[redacted]

66p

cite as (NASA CR-51845; JPL Space Programs Summary 37-21, Vol. 2)

see attached X63 16524

Code 2B

see copy

Space Programs Summary No. 37-21, Volume II [redacted]

for the period March 1, 1963 to April 30, 1963

Initial copy

The Planetary — Interplanetary Program

(Title [redacted])

[redacted]

Security 3

474-2003

jpl
JET PROPULSION LABORATORY
CALIFORNIA INSTITUTE OF TECHNOLOGY
PASADENA, CALIFORNIA

May 31, 1963 66 p

(NASA Contract NAS7-100)

(NASA-CR-51845) SPACE PROGRAMS SUMMARY NO. 37-21, VOLUME 2 FOR THE PERIOD 1 MARCH - 30 APRIL 1963. THE PLANETARY - INTERPLANETARY PROGRAM (Jet Propulsion Lab.) 66 p

N73-73968

Unclas
00/99 18923

[redacted]

[redacted]

Space Programs Summary No. 37-21, Volume II

for the period March 1, 1963 to April 30, 1963

The Planetary – Interplanetary Program

(Title U[redacted]

Copy No. 00358

JET PROPULSION LABORATORY
CALIFORNIA INSTITUTE OF TECHNOLOGY
PASADENA, CALIFORNIA

May 31, 1963

[redacted]

GROUP 4 [redacted] years.

Preface

The *Space Programs Summary* is a six volume, bimonthly publication designed to report on JPL space exploration programs, and related supporting research and advanced development projects. The subtitles of all volumes of the *Space Programs Summary* are:

Vol. I. The Lunar Program (Confidential)

Vol. II. The Planetary–Interplanetary Program (Confidential)

Vol. III. The Deep Space Instrumentation Facility (Unclassified)

Vol. IV. Supporting Research and Advanced Development (Unclassified)

Vol. V. Supporting Research and Advanced Development (Confidential)

Vol. VI. Space Exploration Programs and Space Sciences (Unclassified)

The *Space Programs Summary*, Volume VI is an unclassified digest of appropriate material from Volumes I through V, plus the space science instrumentation studies of the JPL Space Sciences Division.

W. H. Pickering

W. H. Pickering, *Director*
Jet Propulsion Laboratory

Space Programs Summary No. 37-21, Volume II

Prepared under Contract No. NAS 7-100, National Aeronautics & Space Administration

This document contains information affecting the national defense of the United States, within the meaning of the Espionage Laws, Title 18, U.S.C., Sections 793 and 794, the transmission or revelation of which in any manner to an unauthorized person is prohibited by law.

Contents

I. Program Objectives

The primary long-range objective of the NASA Planetary-Interplanetary Program is the development of automatic, unmanned, interplanetary spacecraft technology and the use of this technology in the form of space probes to gather fundamental scientific knowledge concerning the planetary and interplanetary environments, the planets themselves, and solar phenomena, both out of and within the plane of the ecliptic.

The secondary long-range objective of the program is the development of technology and the collection of scientific data which will contribute to the successful manned exploration of the planets and interplanetary space.

The primary objective of the program by 1970 is to have rather completely demonstrated and, to some reasonable extent, exploited (in terms of acquired scientific data) spacecraft capable of: (1) being put into orbit around, and (2) landing on the surface of, Mars and Venus.

A secondary objective during this period will be the initial effort toward extending the above capability toward the planets Mercury and Jupiter and space shots out of the plane of the ecliptic and in toward the Sun. The immediate objective of the program is the initial probing of Mars and Venus.

The Planetary–Interplanetary Program at present consists of three projects: *Mariner C* using the *Atlas-Agena B* vehicle, *Mariner B* using the *Atlas-Centaur* vehicle, and the *Voyager*, using the *Saturn* vehicle. The missions planned for these projects are obviously subject to change because of such influences as new scientific discoveries or unexpected development in vehicle availabilities.

The decision to terminate the *Mariner R* Project was made in January 1963. This decision was based upon the high degree of success obtained by *Mariner 2*. Much of the work being performed at that time was directly or partially applicable to the *Mariner C* or *Ranger* Projects, and transfer of efforts to these projects has been made. Presently, the only active effort directly applicable to *Mariner R* is analysis of data resulting from the *Mariner 2* flight; this work will continue into 1964. Work which had no application to other projects was cancelled.

II. *Mariner R* Project

Subsequent to the decision in early January 1963 to terminate the *Mariner R* Project, much of the *Mariner R* work has been transferred to the *Mariner C* and *Ranger* Projects. *Mariner R-3* design-evaluation-vehicle tests is one of the efforts being continued in support of existing projects (*Mariner C* and *Ranger*).

A. Systems

On November 5, 1962, a formal series of design evaluation tests was begun using the *Mariner R-3* spacecraft. These tests, designated design evaluation vehicle (DEV) tests, were designed to provide additional information on anomalous operating conditions encountered on the *Mariner 2* flight and to investigate selected *Mariner R* design characteristics. (In addition, the tests are providing invaluable data needed for the *Mariner C* project.)

The *Mariner R-3* spacecraft was assembled from *Mariner 1* and *2* spare parts. Following its first system test on June 25, 1962, the *Mariner R-3* was used for special tests in support of the *Mariner 1* and *2* missions. Among these special tests was the verification of the *Mariner 2* midcourse maneuver commands on *Mariner R-3* prior to their transmission to *Mariner 2*, then on its way to Venus.

The following is a brief description of the DEV tests performed to date.

Test 1: primary power voltage variation. A spacecraft operational sequence was synthesized which allowed all spacecraft elements to be exercised. The power subsystem control circuit was adjusted to supply the required voltage levels. Each subsystem engineering group evaluated the performance degradation of their subsystem as the 2.4-kc primary power voltage was decreased to 42.5-v rms, then increased to 57.5-v rms.

The test data indicated that all subsystems could tolerate a wide variation in primary power voltage level if regulation was maintained at the changed level. The transponder was the only subsystem which showed change

at different voltage levels. The transponder B+ supply depended on the voltage level set; therefore, as the voltage input level was changed, the B+ voltage changed, resulting in a change in threshold level.

A battery voltage range of 42 to 57 v, instead of the nominal 28 v, could mitigate the seriousness of a booster regulator failure.

Test 2: data conditioning system cyclic calibration noise. The test objective was to determine the content and level of noise needed to cause the science subsystem to go into the calibration mode, thus explaining the unscheduled science calibrations of the *Mariner 2*. A transient monitor was used to determine the presence and magnitude of transients.

The test did not reveal any areas significantly susceptible to noise, but it did eliminate a number of suspect areas. The *Mariner R-3* spacecraft was very insensitive to noise.

Test 3: 2.4-kc frequency variation. Each subsystem group evaluated the performance degradation of their subsystem as the 2.4-kc primary power frequency was decreased to 1920 cps, then increased to 2880 cps. Also, the free-running frequency of the power subsystem was determined with the 38.4-kc power sync disconnected.

All subsystems operated normally when the 2.4-kc power frequency was varied 1%. This demonstrated that all subsystems will function properly with the 38.4-kc backup oscillator (frequency ±1%) planned for future spacecraft. With a 20% variation of the 2.4-kc signal, communications, central computer and sequencer, and command subsystems operated normally. At these wide frequency variations, the data encoder did not function. This response was in accordance with its performance specification.

With the 38.4-kc sync disconnected and the spacecraft operating in the cruise mode, the free-running frequency of the 2.4-kc primary power was 2077 cps (gyros *on*), and 1977 cps (gyros *off*).

Test 4: noise susceptibility. The noise existing between the various spacecraft grounds and the various operational support equipment grounds was mapped as the spacecraft was stepped through the modes of a simulated mission.

The noise mapped indicated that the spacecraft was relatively quiet. The most significant fact noted was that when AC5A, AC6B, and gyro *on-off* loads were applied, there was a loss of data sync caused by a momentary change in frequency of the 2.4-kc primary power.

Test 5: operation of 400-cps and 2.4-kc power amplifiers with booster regulator failure. The effect of a 10% variation of the DC input to the 400-cps and 2.4-kc power amplifiers was determined using various system loads.

The data indicated that the 400-cps and 2.4-cps power amplifiers operated satisfactorily (as was expected) on input voltages of 52 v ±10%. Since the specified input voltage tolerance is 1%, the power amplifiers would perform satisfactorily if a booster regulator failed.

Test 6: spacecraft power factor determination. The individual and the combined power factors of various loads on the 400-cps and 2.4-kc power supplies were measured by several methods and the effect on waveforms recorded.

As required by system specifications, the power factors were consistently greater than 0.95.

Test 7: data encoder and RF ground investigation. The noise on the electrical grounds between the data encoder and RF equipment was measured. An attempt was made to isolate these grounds and substitute other grounding techniques.

One ground loop was discovered and corrected. As a result of this test, a complete theoretical study of grounds and grounding techniques was initiated.

Test 8: Mariner R-3 *reflectance.* This test was made to determine the amount of heating which could be attributed to reflections between portions of the spacecraft.

Preliminary data reduction indicated that about 1% of a solar constant of reflected light was incident on the vertical hex faces and the surfaces of the Earth sensor. These results represent the first separation of the reflection effect from other modes of heat input. The test indicated the maximum effect of reflectance on spacecraft temperature will not exceed 10%. The spectrally selective nature of the sensor used and the relatively poor spectral solar simulation of the mercury-xenon lamps limited the accuracy of the results; however, the accuracy was well within the broad limits of the investigation.

Tests 9 and 12: science case harness (Case I) evaluation, and data conditioning system ground investigation. These tests were designed to determine whether the additional weight and bulk of shielded wires used in the *Mariner 2* science case harness was justified by a significant reduction in ambient noise levels or crosstalk.

Representative ambient noise levels were measured using the present fully shielded case harness, then using a harness in which only the AC power leads were shielded. With the unshielded case harness installed, the performance of the system and subsystem was observed in the normal operating modes. These results were compared with the results of previous tests using the shielded harness.

When the unshielded harness was used the subsystem functioned without observable performance degradation. In addition, the noise amplitudes noted were generally equal to or lower than those observed when the shielded case harness was used.

It was concluded that the *Mariner 2* science subsystem would have performed equally well without the extra weight and complexity of shields on most of the case harness signal wires. The same conclusion could not be drawn regarding other subsystems without further testing. These tests did indicate, however, that from a weight and reliability standpoint it may be worthwhile to fabricate two sets of harnesses for testing on the proof test models of future programs: one shielded in the *Mariner* 2 fashion and the other unshielded except for AC power lines.

Tests 10 and 11: event-channel noise characteristics, and limiting of the 2.4-kc clock. The 2.4-kc primary power input to the data encoder transformer-rectifier unit was monitored using the unassigned channels of the 10-channel transient monitor. As the spacecraft was operated through a simulated operational sequence, the amplitude of the transients as they appeared on the 2.4-kc input to the data encoder transformer-rectifier was measured.

The following conditions caused a momentary interruption of the 2.4-kc signal, resulting in a brief loss of data sync: (1) Attitude control power *on*. (2) Gyros *on* and *off*. (3) Science *on* and *off*. (4) Science calibrate *on* and *off*, and (5) Earth sensor *on*.

The 2.4-kc power to the data encoder was unaffected for all other conditions.

Test 13: calibration of temperature transducers. A decade box was substituted for each temperature transducer at the connector and the telemetry indication compared with the decade box resistance. A 10-ft unshielded wire was connected to the lower thermal shield transducer connector, then routed close to the spacecraft ring harness to determine the effect of spacecraft noise induced through this long unshielded wire.

When compared with the "black box" calibration method used previously, the decade substitution method proved superior in that long leads from the spacecraft to the operational support equipment were eliminated and the data encoder did not have to be removed from the spacecraft. Tests with the 10-ft unshielded wire indicated that a weight saving may be possible through the use of unshielded temperature transducer leads. Fig. 1 shows typical calibration curves (Telemetry Channel 51), using the old and new calibration methods.

Test 14: long-range Earth sensor reflection. The objective of this test was to determine if the reflection of the sunlight from various spacecraft components would cause a degradation in the Earth intensity output. The possibility of a false reflected acquisition source was also investigated.

The test results showed that the reflected sunlight did not affect the light intensity output, nor did the com-

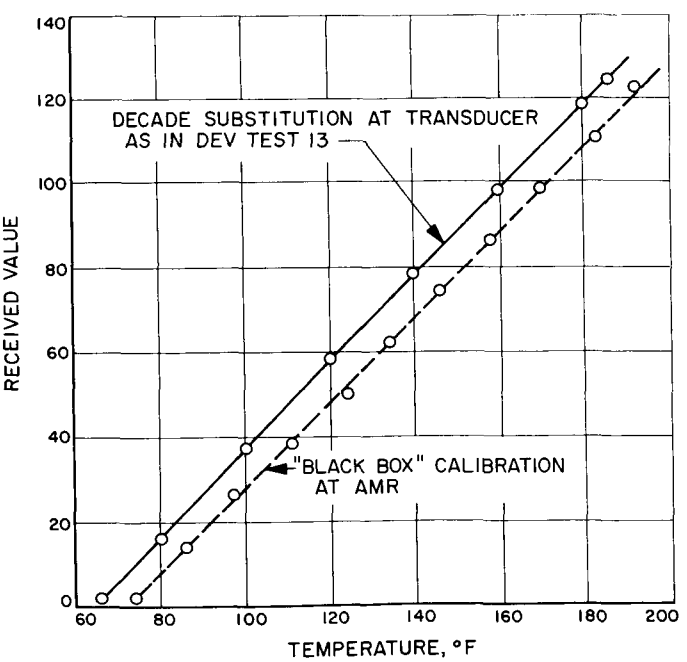

Fig. 1. Typical temperature calibration curves

ponents located on the antenna create any Earth sensor difficulties.

Test 15: temperature control. This test compared and correlated *Mariner 2* flight data, *Mariner R-3* test data, and temperature control model test data. The 25-ft space simulator was used to simulate *Mariner 2* Flight Days 240, 252, 303, and 305 (1, 13, 64, and 66 days after launch). Fig. 2 shows the spacecraft in the simulator.

The simulated space conditions resulted in spacecraft temperatures about 10 to 22°F lower than the flight temperature information telemetered from *Mariner 2*. The temperature discrepancy was greater for higher simulated solar intensity values.

Test 16: simulated midcourse interactions. This test, which was performed at the Lockheed Research Center Space Simulation Facility, near Newhall, California, was designed to compare the actual autopilot performance and spacecraft dynamics in a simulated space environment with the results of analysis and analog computer simulation. Further, an attempt was made to determine the validity of the analytic approximations and identify those areas in which a more detailed simulation or complete change in concept was needed. Some of the approximations made in the theoretical analysis of autopilot performance were:

(1) Backlash and friction were ignored; linearity was assumed.

(2) Ideal jet vane characteristics were assumed.

(3) Dynamic properties were based on a simple model comprised of rigid bodies coupled through springs and hinges.

(4) Cross-coupling through resonant members was largely ignored.

The spacecraft was spring suspended on a 45-ft pendulum with three axes of freedom (Fig. 3). The spacecraft was balanced in each configuration so that the line of suspension went through the CG of the spacecraft and a

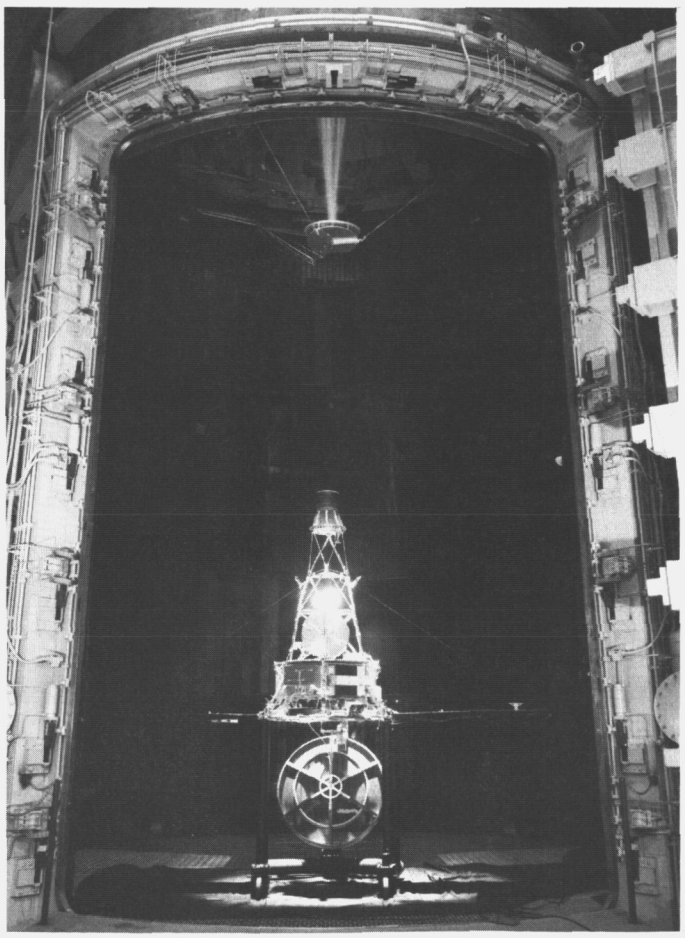

Fig. 2. *Mariner R-3* in JPL 25-ft solar simulator

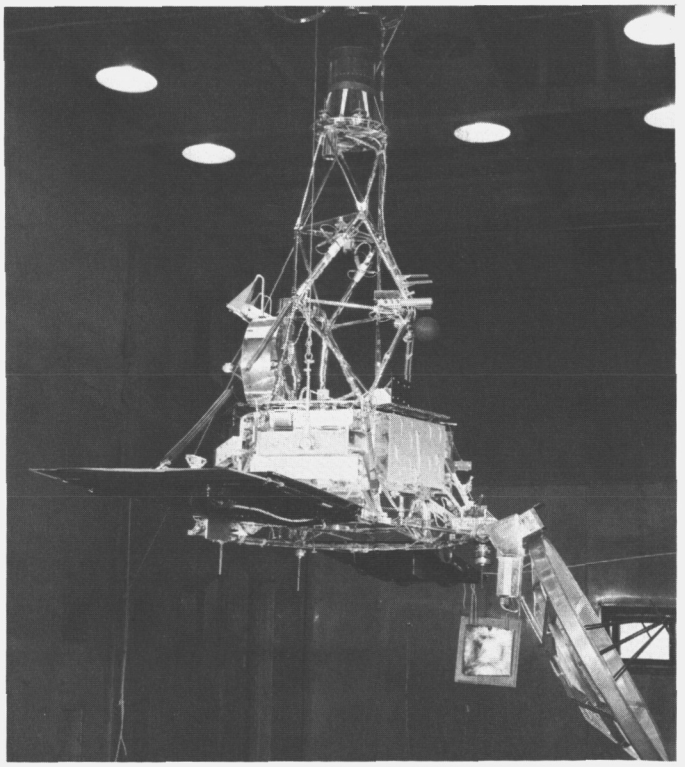

Fig. 3. *Mariner R-3* in high altitude simulator during SMIT

near perfect balance was maintained. The spring suspension allowed 5-in. travel for the 50-lb thrust of the midcourse motor. This allowed enough free-flight time to examine the autopilot response through the first 100 to 500 msec of motor burn.

In each case, the effect of the analytic approximations was examined and individually evaluated. Modal analysis on the type of suspension system used in this test provided valuable information, and analysis and analog computer simulation results were substantially confirmed.

Test 17: RF interference. The objectives of this test were to make an RF signature of the *Mariner R-3* spacecraft, to irradiate the spacecraft with RF and locate possible RF interference, and then to compare the test results with the limits defined by JPL specification.

The RF generated by the spacecraft system and that of selected subsystems was mapped and logged. The spacecraft system and certain subsystems were irradiated by RF and the spacecraft monitored to determine the effect of RF radiation on system and subsystem operation.

The test data indicated there was no RF radiated by the spacecraft system or any of its subsystems in excess of the limits required by specification. Also, the spacecraft system was found to be very insensitive to RF interference. Data from this test will enable future RF interference specifications to more closely represent spacecraft function and design.

Test 18: radiometer scan. The *Mariner R-3* radiometer was operated in slow scan for 4.2 hr in a test designed to find the cause for some apparently anomalous data received from *Mariner 2* during its Venus flyby. The test attempted to locate any sticking or fluctuation in the scan mechanism and determine the linearity of its scan.

The test results indicated that there is no strong evidence of binding or sticking of the scan mechanism; the fluctuations about the average shown in Fig. 4 could be statistical. The period of fluctuation (about 40 sec) did not correspond to any known periodic phenomenon on the spacecraft. On the basis of this test, no conclusions could be made concerning the *Mariner 2* data.

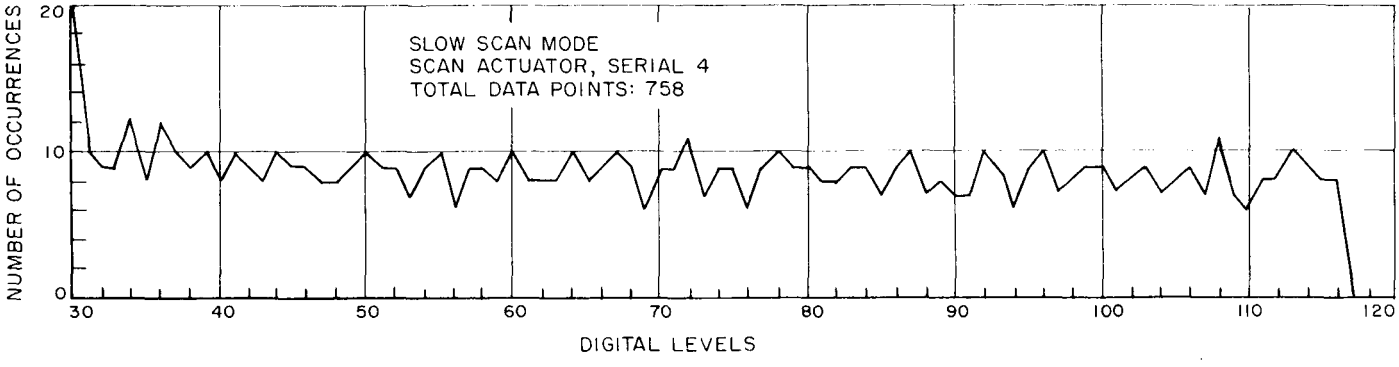

Fig. 4. Radiometer scan data, *Mariner R-3*

III. *Mariner C* Project

The primary purpose of the *Mariner C* Project is to permit a biology-oriented scientific investigation of the planet Mars during the 1964 opportunity. Secondary purposes in order of priority are: (1) to make interplanetary scientific investigations in the region between the Earth and Mars orbits, (2) to develop additional experience in the design of spacecraft capable of conducting specific interplanetary missions, (3) to provide experience and knowledge which will permit continued development of attitude stabilized spacecraft of the later *Mariner B* and *Voyager* types. The *Mariner C* spacecraft will be injected into Mars planetary transfer orbit by the *Atlas*-space-booster/*Agena D* launch vehicle. Three identical spacecraft will be launched during this planetary opportunity.

The *Mariner C* spacecraft detail design is being firmed with most decisions having been made regarding subassembly configuration, location, and electrical interfaces. Design specifications and control drawings are being released to detail these interfaces. The spacecraft estimated weight increased to an unacceptable limit of 612 lb, requiring action to establish a maximum allowable weight of 570 lb. It was necessary to make some changes in the spacecraft configuration, including the interchange of some science experiment packages.

A design review of each subsystem on the spacecraft has been in process during March and April. This has resulted in a clarification and more thorough understanding of the spacecraft design by all cognizant subsystem groups. Interface problems and design deficiencies have been uncovered and corrected during this review period.

A project requirements and policy document was coordinated and put into effect throughout all spacecraft areas in March. This document defines the documentation, quality assurance, and schedule requirements as well as the discipline division responsibilities toward the project.

During March a meeting of the potential experimenters for the 1964 Mars mission was held in Washington DC at NASA Headquarters. This resulted in recommendations for changes in the *Mariner C* science payload. These

recommendations have been carefully studied at JPL with regard to the influence on the spacecraft design. Decisions were made on the basis of these studies so that the spacecraft design could proceed with a minimum of delay. To assist the experimenters in preparing their equipment for the spacecraft, a series of documents defining the documentation, quality assurance, and schedule requirements were prepared. In addition, all electrical and mechanical interfaces which were already firm were defined in detail and sent to each experimenter.

The first *Mariner C* Project meeting was held at Lockheed Missiles and Space Company (LMSC) on April 10, 1963. This meeting was attended by representatives of the Lewis Research Center (LeRC), LMSC, General Dynamics/Astronautics, Space Systems Division, NASA Headquarters, and JPL. The project manager outlined the over-all mission objectives and major features of the schedule to support these objectives. The spacecraft systems manager described the spacecraft as well as the important interface features. LeRC and LMSC gave a comprehensive presentation covering the current launch vehicle capability and the capability which will result from the programmed improvements to support the *Mariner C* mission.

A meeting was held at LeRC on April 24, 1963 to explore the factors associated with a combined system test for *Mariner C*. As a result of this next meeting, it was decided to investigate the possibility of using the *Mariner C* spacecraft proof test model, the *Ranger 10* launch vehicle, and Launch Pad 13 at the Atlantic Missile Range for the systems test. This combined system test would be scheduled so that no interference would result in the *Ranger 10* launch preparations.

JPL conducted a study and subsequently recommended to NASA Headquarters that the Mars 1964 opportunity incorporate three launches instead of two. This study included the probability of launching three vehicles from two launch pads during the launch period as well as the probability of achieving at least one mission success. A cost analysis for achieving the one mission success was also made.

The preliminary draft of the *Project Development Plan* has been reviewed by the technical division at JPL and LeRC. Comments and revisions resulting from this review are currently being incorporated. The final coordinated copy will be sent to NASA Headquarters for approval during May 1963.

A. Systems

1. Trajectories

a. Introduction. In late 1964 at least two attempts will be made to launch a *Mariner C* spacecraft on a fly-by path to the planet Mars. The spacecraft will be launched by an *Atlas-Agena D* booster. The purpose of the mission is to gather scientific data on the interplanetary environment between Earth and Mars as well as to take scientific measurements, including TV pictures, of the planet itself.

The purpose of this article is to present preliminary trajectory information covering this mission.

b. Launch and arrival date philosophy. To increase the probability of a successful launch, a total launch period of 28 days, using Type I trajectories only, is being used for planning purposes.[1] The actual launch period utilized for the mission will probably be somewhat less than this, being ultimately determined by the final spacecraft weight and launch vehicle performance capability. During the launch period, two shots will be attempted from two separate launch pads. On the first available launch day, a countdown will be conducted simultaneously on both vehicles.

At a predetermined time in the simultaneous countdowns, probably a few hours before lift-off, and if both vehicles are still in a ready condition, one of the countdowns will be suspended. Two days after launch of the first vehicle, the countdown on the second vehicle will begin again.

Since either launch may occur on any day of the launch period, two trajectories will be provided for each launch date with fixed arrival dates separated by 5 days. The 5-day separation at encounter is necessary to simplify the operations during the critical encounter portion of the flight. On the first attempted launch date, when simultaneous countdowns are being conducted, each vehicle will utilize the same arrival date trajectory so that the same injection loci will be used no matter which vehicle is launched. If the first launch is successful, the second

[1]At the present, Type II trajectories are being considered for inclusion in the mission. If they prove to be feasible, the launch period will be extended to 35 days or more, and a third launch will probably be utilized. Type I trajectories are those along which the spacecraft traverses less than 180 deg in heliocentric space from launch to encounter. For Type II trajectories the spacecraft traverses more than 180 deg but less than 360 deg from launch to encounter.

launch will use the remaining arrival date for the duration of the launch period. If the first shot is unsuccessful, the second launch will use whichever arrival date is most suitable.

c. The near-Earth trajectory. Interplanetary trajectories near the Earth can be accurately represented by a hyperbola whose perigee is nearly equal to the parking orbit radius. The orientation of the outgoing asymptote and the required injection energy are relatively fixed for the few-hour launch window[2] on any launch day but will vary from day to day through the launch period. The injection loci and launch window for a given launch azimuth are determined by these two parameters. The injection loci move downrange as the injection energy increases and as declination of the outgoing asymptote increases in algebraic value. As the value of the declination of the outgoing asymptote increases, the launch window will increase.

In order to launch the spacecraft, a launch azimuth from AMR must be used which will allow the spacecraft to travel in a plane which contains both the launch site at launch and the geocentric asymptote. Since the asymptote is fixed inertially in space and the launch site is rotating, the launch azimuth must be varied continuously through the window. Also, since it is optimum (for maximizing payload) to inject at or near perigee, the parking orbit coast time must also be varied continuously to meet this condition.

Due to AMR range safety considerations the maximum allowable launch azimuth sector which can be utilized is 90 to 114 deg E of N from AMR. With this azimuth sector, the *Mariner C* trajectories will have daily launch windows of between 3 and 4 hr due to the high positive value of the asymptote declination. This high value of declination also causes the injection locations to be well downrange through most of the period.

Due to the extreme downrange injection locations characteristic of this mission and the possible difficulties in furnishing adequate tracking and telemetry coverage over these injection loci, two sets of possible trajectories are being considered.

Fig. 1 through 3 show the Earth tracks and the composite injection loci for the most uprange and most down-

[2]The launch window is defined as the amount of time during any given day of the launch period when it is possible to launch the vehicle.

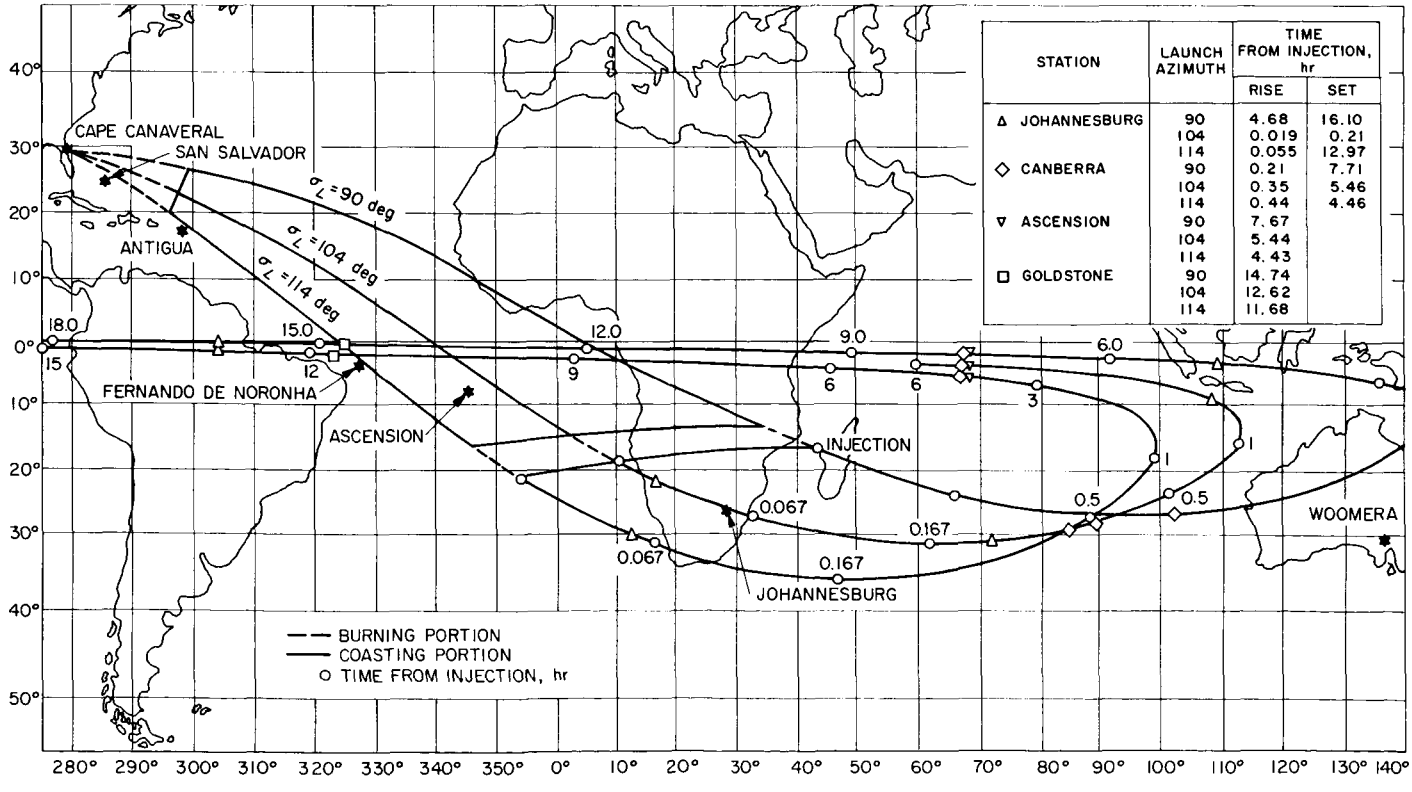

Fig. 1. Earth track and view periods for the most uprange injection loci, July 15 and 20, 1965 arrival dates

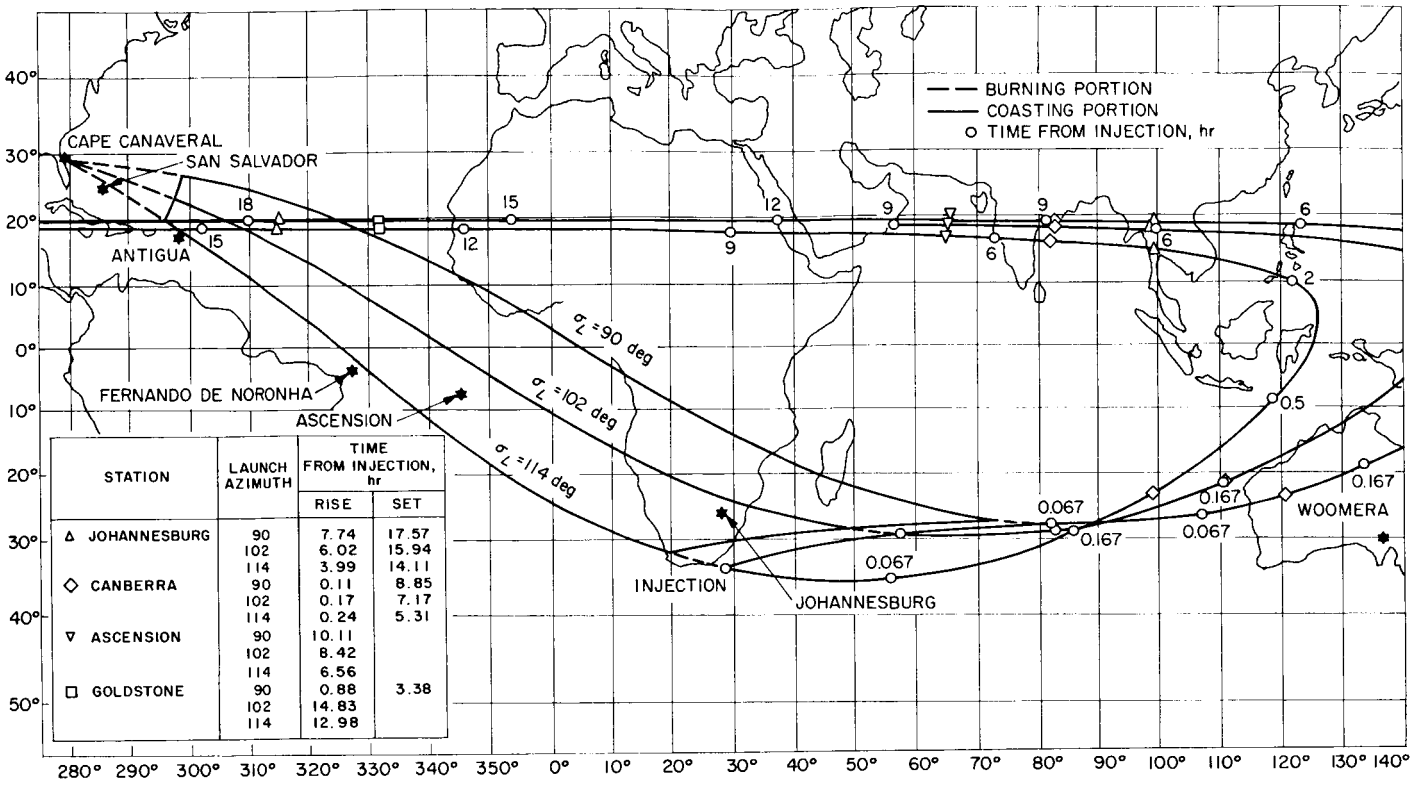

Fig. 2. Earth track and view periods for the most downrange injection loci, July 12 and 17, 1965 arrival dates

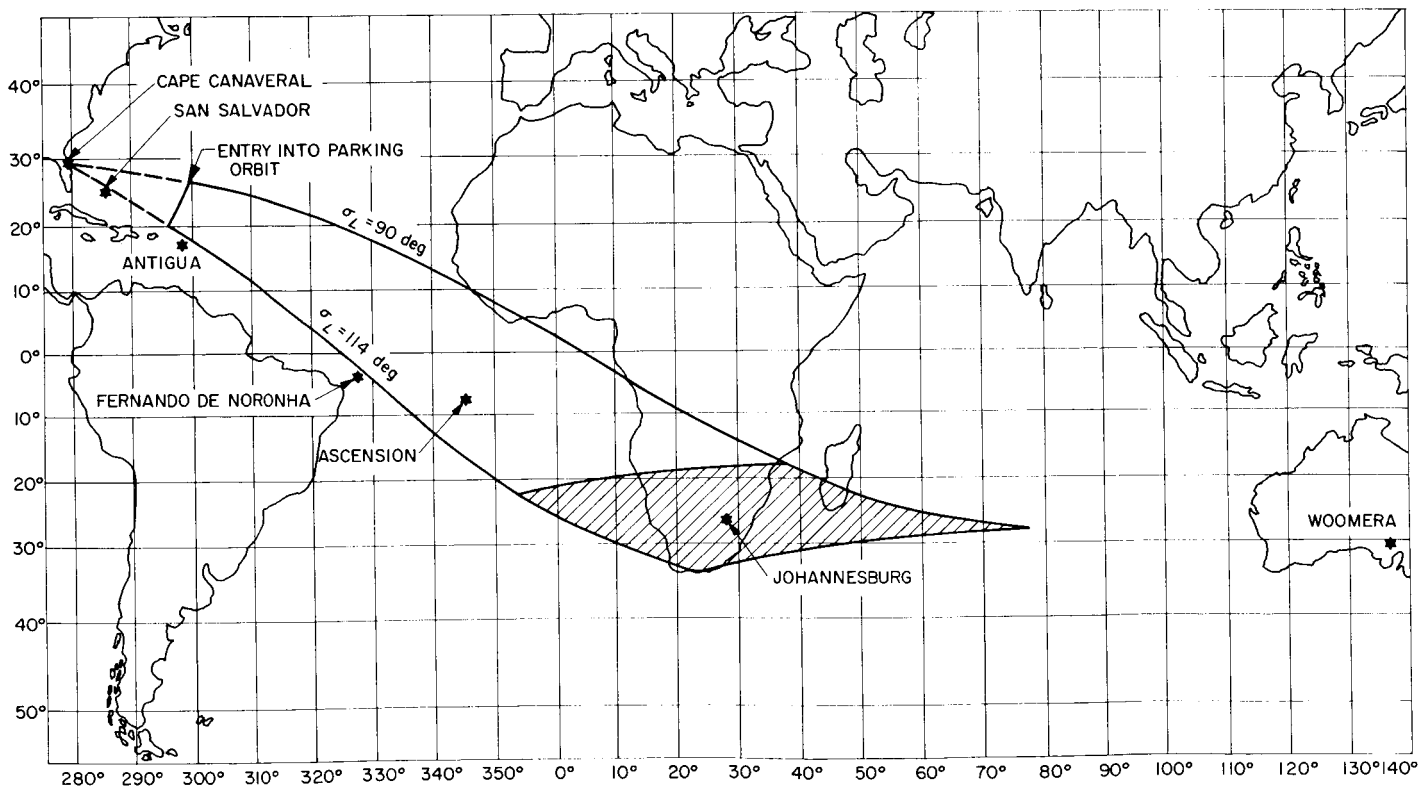

Fig. 3. Composite injection loci for July 15 and 20, 1965 arrival dates

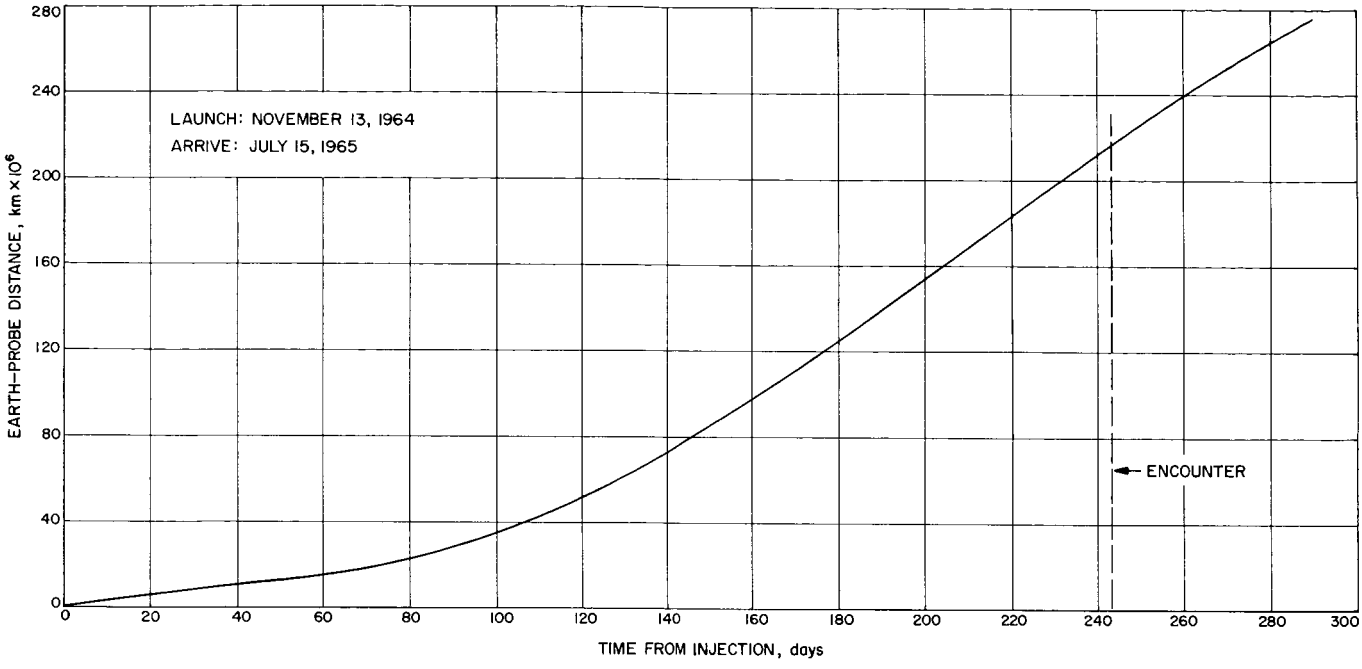

Fig. 4. Typical plot of Earth-probe distance versus time from injection

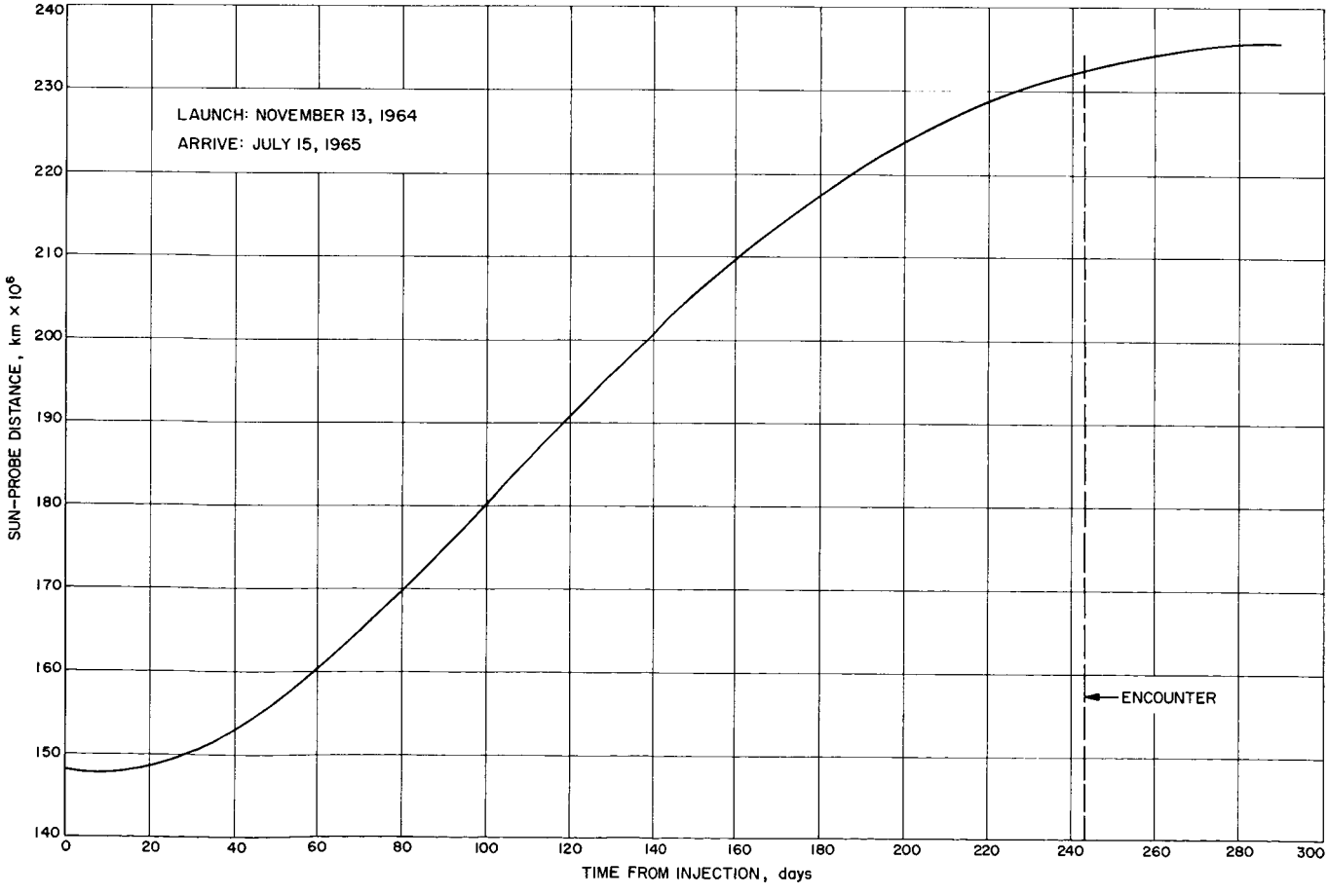

Fig. 5. Typical plot of Sun-probe distance versus time from injection

range injections for the two sets of trajectories. Set 1 utilizes July 15 and 20, 1965 for arrival dates, while Set 2 uses July 12 and 17, 1965. It can be seen from these curves that in order to give continuous tracking and telemetry coverage a rather large number of tracking and telemetry ships would be required. If the problem of providing suitable coverage for the entire 90- to 114-deg launch azimuth sector becomes excessive, consideration can be given, possibly on a day-to-day basis, to decreasing the usable sector to improve coverage.

d. Heliocentric and near planet characteristics. The heliocentric, or Sun-centered, portion of the trajectory will be an ellipse with the Sun at one focus. With launch dates beginning on November 12, 1964, and extending through the early part of December, the flight times for the two sets of arrival dates chosen will be from 214 to 247 days. The maximum communication distance at arrival will be approximately 221 million km for Set 1 and 218 million km for Set 2.

Fig. 4 and 5 show typical plots of the Earth-probe and Sun-probe distance with time. Fig. 6 is an ecliptic projection of a typical *Mariner C* trajectory between Earth and Mars.

Two other important parameters during the heliocentric phase of the trajectories are the cone and clock angles of the Earth as seen from the spacecraft. The cone angle is defined as the Sun-probe-Earth angle. The clock angle is defined as the angle between the projection of the spacecraft-Canopus direction on a plane perpendicular to the Sun-probe direction and the projection of the spacecraft-Earth direction on the same plane (Fig. 7).

For the *Mariner C* trajectories the cone and clock angles are almost fixed during approximately the last half of the flight, allowing the use of a fixed high-gain antenna. Fig. 8 and 9 show typical plots of the cone and clock angles of Earth from launch to encounter.

When the spacecraft nears the planet Mars, it will enter a hyperbolic orbit with respect to the planet.

The trajectory about Mars is completely defined by the impact parameter vector **B** and the incoming hyperbolic velocity vector $\mathbf{V}_\infty$. The impact parameter is defined as a vector from the center of Mars perpendicular to the incoming asymptote direction. The aiming point at the planet is specified by magnitude and direction of the desired impact parameter.

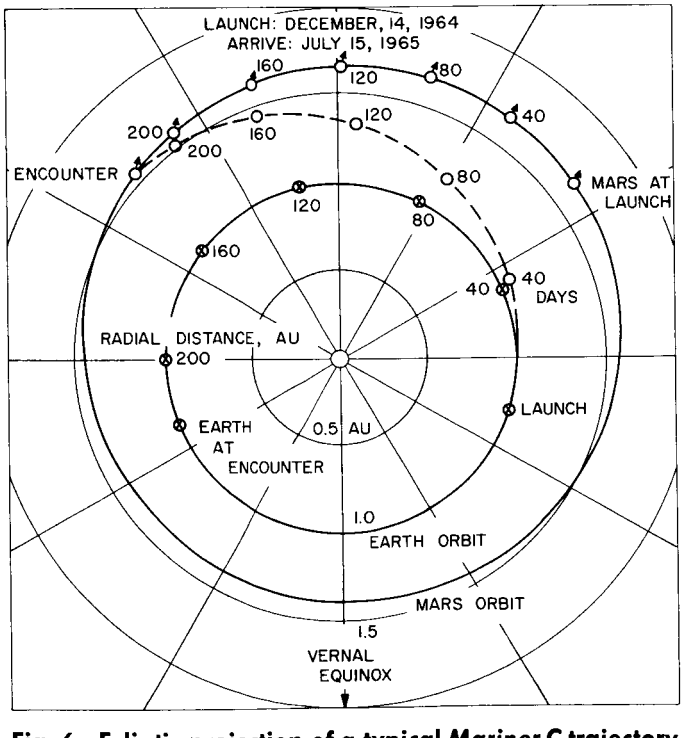

Fig. 6. Ecliptic projection of a typical *Mariner C* trajectory

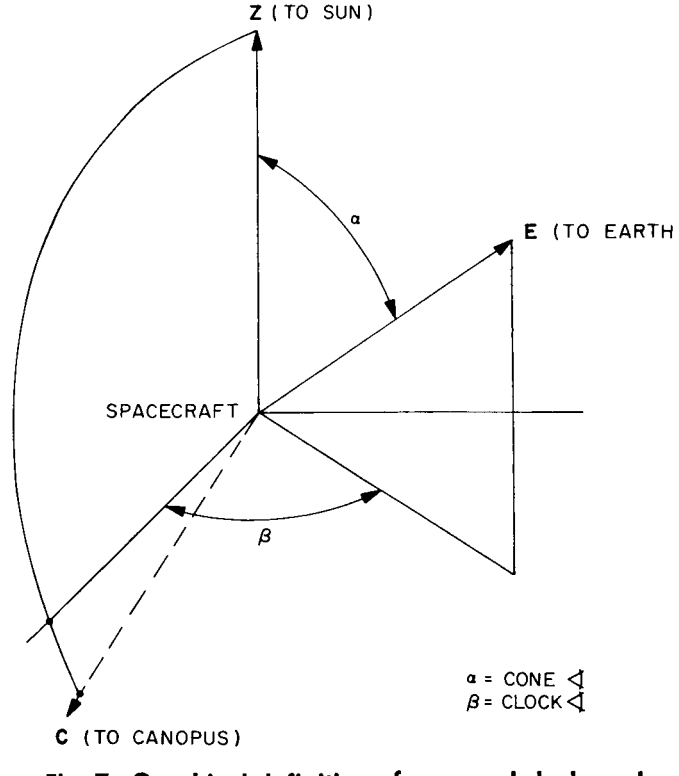

Fig. 7. Graphical definition of cone and clock angles

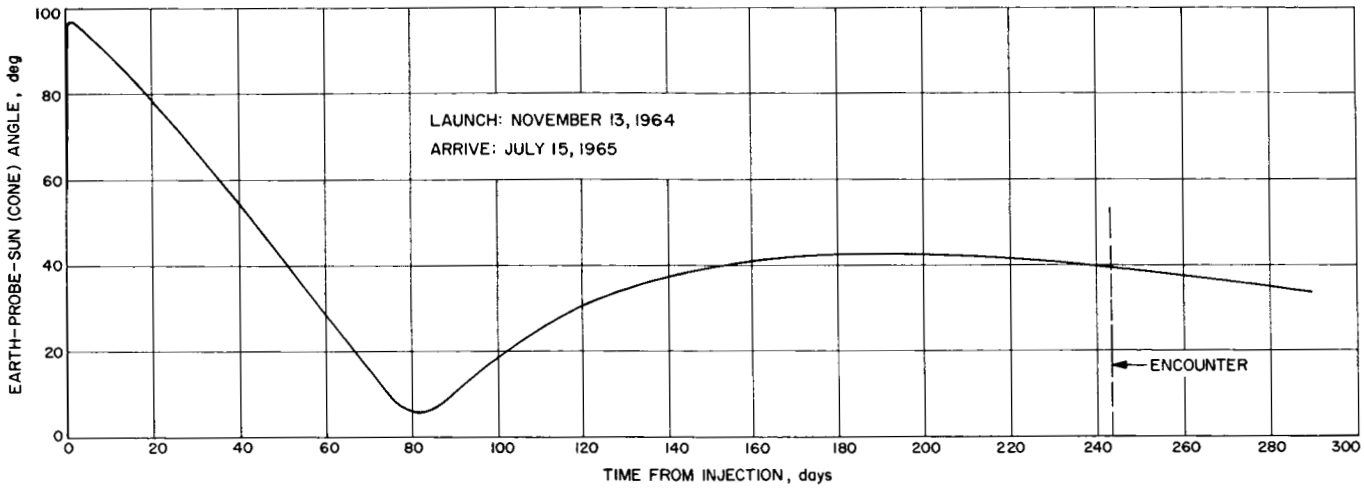

Fig. 8. Typical plot of Earth-probe—Sun (cone) angle versus time from injection

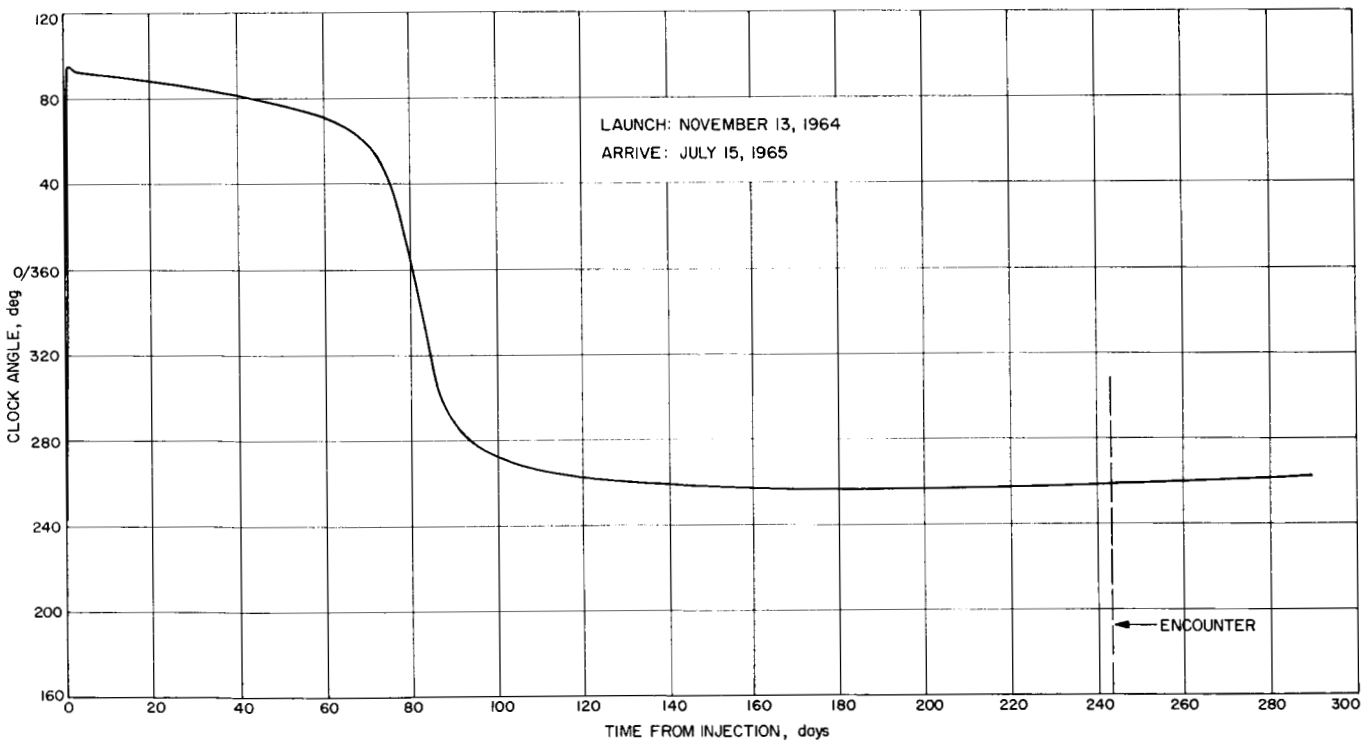

Fig. 9. Typical plot of clock angle versus time from injection

The aiming point must be selected considering the following constraints: (1) The Sun-probe-near-limb-of Mars angle must always be greater than 5 deg. (2) It is desirable that the Earth-probe-near-limb-of-Mars angle always be greater than 0 deg. (3) The Canopus-probe-near-limb-of-Mars-angle should always be greater than 36 deg.

Fig. 10 shows the aiming point for a typical trajectory during the launch period. The figure is plotted in the **T**, **R** plane which is perpendicular to the incoming asymptote and hence contains the impact parameter **B**. **T** is parallel to the ecliptic plane and $\mathbf{R} = \mathbf{S} \times \mathbf{T}$. The contours drawn in Fig. 10 represent aiming points which would result in one of the three constraints men-

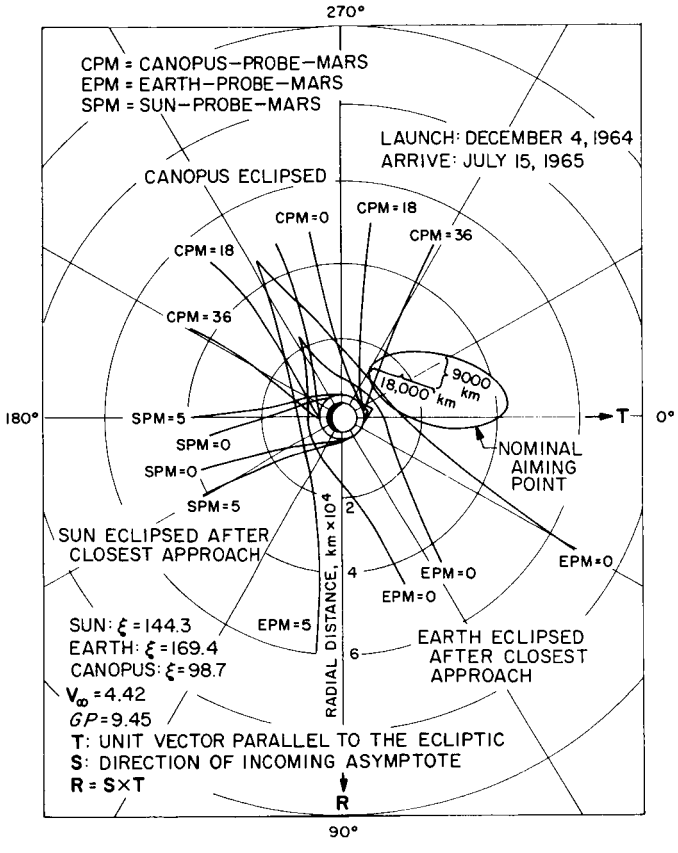

Fig. 10. Aiming point for a typical trajectory

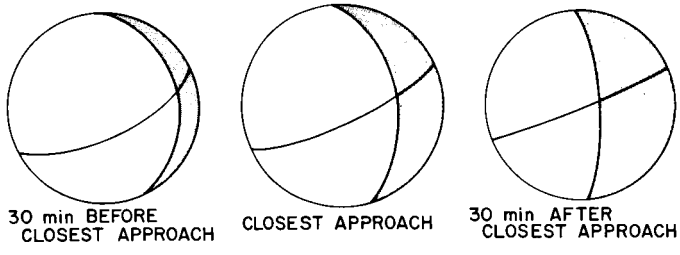

Fig. 11. Nominal fly-by trajectory views

tioned above being violated. For example, all impact parameters lying inside the contour labeled $EPM = 0$ would result in Earth-probe-near-limb-of-Mars angles less than 0 deg or occultation of the Earth, and violation of Constraint (2). The ellipse drawn about the nominal aiming point represents the expected 3σ dispersion in the aiming point due to midcourse maneuver execution errors.

As can be seen from Fig. 10, the nominal impact parameter has a magnitude of about 25,000 km which corresponds to a closest approach distance of about 23,000 km, using a V_∞ of 4.2 km/sec. The probable range in V_∞ will be from 4 to 4.4 km/sec.

Fig. 11 shows the spacecraft view of Mars during the encounter phase for a typical trajectory. The darkened area represents the portion of Mars in the Sun's shadow while the curved line represents the equatorial plane of Mars.

B. Spacecraft Design

1. Introduction and Abstract

A major change in the complement of scientific experiments aboard the *Mariner C* spacecraft has occurred since the reporting in *SPS 37-20*. This has resulted in some rather significant changes to the over-all spacecraft configuration. In addition, the continued evolution of the detail design of the spacecraft has permitted better definition of the location of some of the smaller spacecraft components. The current results of the change in scientific experiments, as well as those engendered by the evolution of the spacecraft design, are reported upon.

The operational and handling implications of using ultra-light weight and integrated structures on the *Mariner C* are discussed. Several specific examples of the problems in using such structures are cited.

The temperature control section will report on the absorptance standard which occupies four telemetry channels on the *Mariner C* spacecraft. The purpose of the standard is to make solar absorptance measurements of several selected surfaces that will contribute to the interpretation of flight data as well as solar simulator test data.

The cabling section contains a brief description of the case harness support structure.

2. Configuration

The *Mariner C* spacecraft configuration is currently shaped to accommodate the following scientific experiments:

(1) Helium vapor magnetometer.

(2) Cosmic dust detector.

(3) Ion chamber.

(4) Trapped radiation detector.

(5) Low energy plasma detector.

(6) Cosmic ray telescope.

(7) Television camera.

(8) Ultra-violet photometer.

Of this list, the trapped radiation detector and the cosmic ray telescope are additions to the previously considered complement of experiments. Of the remainder, the ultra-violet photometer is being accommodated in place of the infra-red grating spectrometer and a low energy plasma experiment, developed by MIT, will be flown in place of the JPL plasma probe.

The trapped radiation detector will consist of four detector tubes approximately 3 in. long and 1 in. in diameter mounted to an electronic package approximately 6″ × 5″ × 4″. Three of these tubes will be pointed at a cone angle of 70 deg. The fourth tube will be pointed at a cone angle of 135 deg. (Cone angle is defined as the angle between the Sun line and the pointing direction). Each of these tubes has an acceptance cone of 70 deg total angle. In order to accommodate these view requirements and package size, this instrument will be mounted on the upper octagonal ring of the basic spacecraft structure in Bay IV as close as possible to Bay III which contains the scientific data system.

The cosmic ray telescope will consist of a counter telescope approximately 1½ in. in diameter and 2 in. long attached to a standard size electronic subassembly. The subassembly will be located in the science bay (Bay III) immediately adjacent to the lower octagonal structural ring. An opening will be machined in the octagon support ring to provide an unobstructed view for the counter telescope. The instrument is pointed at a cone angle of 180 deg and will have an unobstructed field of view of 30-deg half cone angle about this nominal pointing direction.

The MIT low energy plasma detector will consist of a cup approximately 7 in. in diameter and 4 in. high. The detector cup will be mounted on the upper octagonal ring directly above Bay III. A pigtail from the cup will be routed directly to the associated electronic package immediately below the instrument. The cup will be pointed in a nominal viewing direction of 10-deg cone angle.

The ultra-violet photometer will be mounted on the planet science scan platform in the position previously provided for the infra-red instrument. The ultra-violet instrument is generally less restrictive, mechanically, than the IR instrument and presents no special spacecraft configuration problems.

As reported previously, the magnetometer sensor and ion chamber are located on the low-gain antenna waveguide. Pattern tests on both the low- and high-gain antennas have progressed sufficiently to allow the determination of the tube elevations at which these instruments may be mounted. The highest point on the magnetometer sensor will be 2 ft from the top of the low-gain antenna. The center of the ion chamber will be 37 in. above the top of the spacecraft.

Detailed design of the pedestals required to support the square root Sun sensors on the top of the spacecraft has permitted detailed definition of mounting locations for the Earth detector and Sun gate. The Earth detector will be mounted to the side of the pedestal located above Bay VI. The Sun gate will be mounted to the back of the pedestal above Bay II.

In the interest of minimizing weight a new approach will be used to actuate the four solar panels. This scheme utilizes a separate spring on each panel to provide the opening torque and a central speed retarder to control the opening speed of all four panels. The central retarder will be mounted at the top of the superstructure truss on the spacecraft centerline. A cable will connect the retarder to each solar panel for transmitting the retarding force. Detail design is proceeding to accommodate this actuation scheme. The structure and panels will continue to be designed to accommodate the original single actuators as a backup approach.

Although the changes mentioned above represent rather significant changes to the *Mariner C* spacecraft configuration, no unsolvable problems have been uncovered to date. The remainder of the spacecraft remains as previously reported.

3. Booster Interface

During the reporting period, final design has been started for those items in the spacecraft/*Agena D* interface area. The interface configuration has remained essentially as described in prior issues of the *SPS* (Fig 12). While both the clam-shell shroud and the over-the-nose shroud are being designed, only the former is shown in the figure.

With the exception of the shroud design, the only significant problem areas as yet unresolved are the low-gain

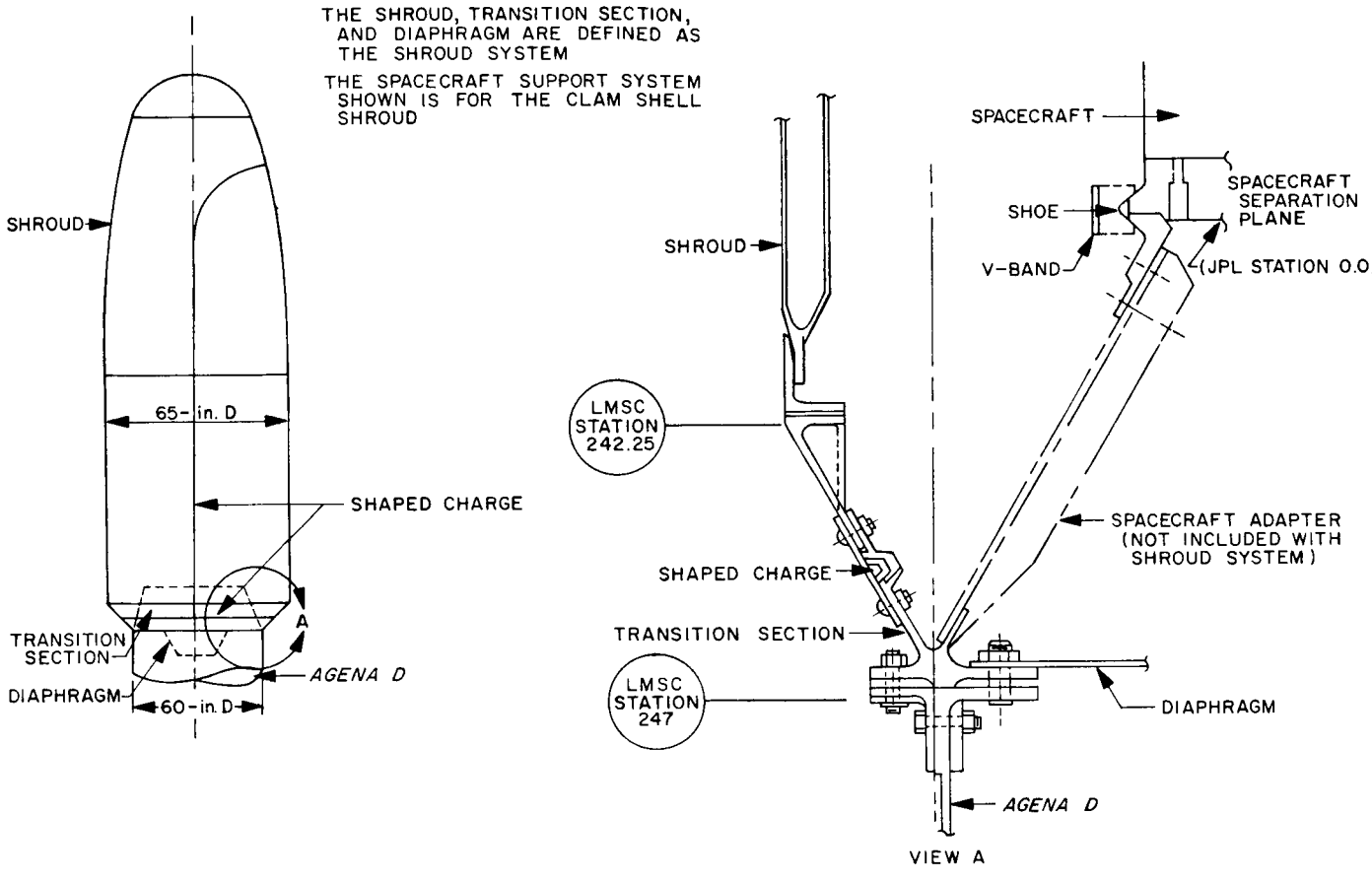

Fig. 12. Spacecraft support system nomenclature

antenna coupler, spacecraft umbilical and inflight disconnect connectors, and the *Agena* diaphragm. As with the rest of the spacecraft support system, each of these items is under the cognizance of Lockheed Missiles and Space Company (LMSC), Sunnyvale, California.

LMSC has developed a beam-supported diaphragm design which appears adequate except for its high weight of approximately 12 lb. Another minimum weight design is being evaluated which would have the diaphragm tied down to both the center and outer edge of the *Agena D* forward equipment rack.

4. Structure

A major *Mariner C* structure design goal was to achieve a significant structural weight reduction. By pursuing a more integrated design and utilizing point damping, the structural weight fraction has been reduced to approximately 15% of the gross spacecraft weight (from approximately 25% on *Mariner R*).

This reduction in weight has been obtained in many cases by utilizing thin-gage material. This has produced two major nonstructural problems: (1) the heat conducting capability of these structures has been reduced, and (2) improper handling of these structures can cause severe damage. The first problem has necessitated adding more material in certain areas to restore adequate heat conducting capacity. The second problem has required that special handling techniques be developed and special storage and shipping fixtures be fabricated.

Examples of these types of structures on the spacecraft are the solar panels, the omni antenna, the high-gain antenna and the temperature control louvers. The solar panel structures are fabricated from 0.003- and 0.005-in. aluminum. (This material can easily be dented with the fingers.) The omni antenna structure consists of a 7.5-ft aluminum tube, 3.870 in. in diameter with 0.025-in. walls. This tube should not be dented or have eccentricities because the tube is an RF wave guide. The high-gain antenna dish structure will be fabricated from ultra light weight honeycomb. The aluminum skins will be 0.004 in.

thick and the honeycomb core material 0.0007 in. thick. The temperature control louvers are fabricated from 0.006-in. aluminum sheet. All of these structures are susceptible to damage if handled improperly.

The integration of packaging chassis and gas system into the structure has created another class of operational and handling problems. If one item is removed, additional auxiliary support may be required for the remaining components. There are three specific examples of this:

(1) The basic structure will be built on a large aluminum tooling plate called a universal ring. This universal ring is intended to support the spacecraft in the same manner as the *Agena* adapter. If the spacecraft is not supported at the eight attach points, bus structural failures may result. The spacecraft will be attached to the universal ring during all JPL operations. The only time the spacecraft will be removed from this fixture is when it is transferred to a flight adapter.

(2) When the electronic chassis are mounted on the octagon structure, most of the chassis structural support is derived from the attachments to the bus. Special fixtures which supply the necessary structural integrity must be attached to the chassis when they are removed from the spacecraft. The octagon in turn derives shear strength from the chassis. When the chassis are removed, shear plates must be installed on the octagon structure to supply the required torsional stiffness.

(3) The attitude control system will include a welded plumbing system which must be installed in the spacecraft as a unit. The gas weight requirements have been reduced by locating the jets as far as possible from the CG on the solar panel tips. Because the panels are not on the spacecraft at all times, auxiliary support structures must be provided to support the plumbing and jets during the SAF test operations and when shipped to AMR.

The operational and handling complexities noted above apply to many other areas. To solve these problems, protective fixtures will be provided for as many portions of the spacecraft as possible and *all* people who will have contact with the spacecraft will be educated in the proper handling techniques. This education will be repeated periodically and portions of the fragile structures will be offered to people for destruction.

5. Temperature Control

a. Background information for absorptance standard design. Extensive testing of the *Mariner C* temperature control model (TCM) is planned during the last quarter of 1963. These tests will be similar to those previously conducted on the *Mariner R-3* and the *Ranger* Block II (TCM) spacecrafts using the JPL *Mercury-Xenon* solar simulator facility.

Since these tests will provide the principal data for the determination of the adequacy of the *Mariner C* thermal design, the sources of experimental errors are of concern. The recognized errors in the solar simulation can be divided into three areas: (1) Those errors associated with the less-than-solar collimation or parallelness of the light. (2) Those errors associated with the uniformity of the intensity of the light over the test volume, including reflections from the chamber optics. (3) Those errors associated with a non-solar spectral distribution of the light's energy. It is this third source of error that led to the design of an absorptance standard to be flown on *Mariner C*.

In taking advantage of certain properties of a material such as a low solar absorptance, it has been necessary to compromise other desirable properties such as the specular independence of this absorptance. The designers of solar simulators have found it necessary to compromise spectral considerations in favor of arc sources which are capable of producing an adequate intensity over a large test area.

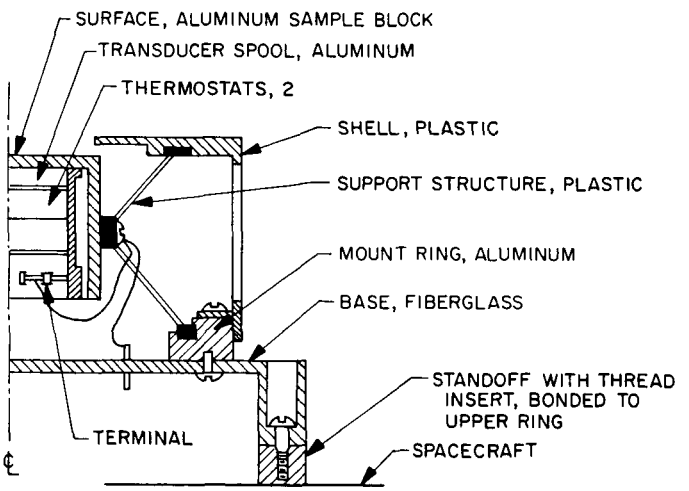

Fig. 13. Temperature control absorptance standard

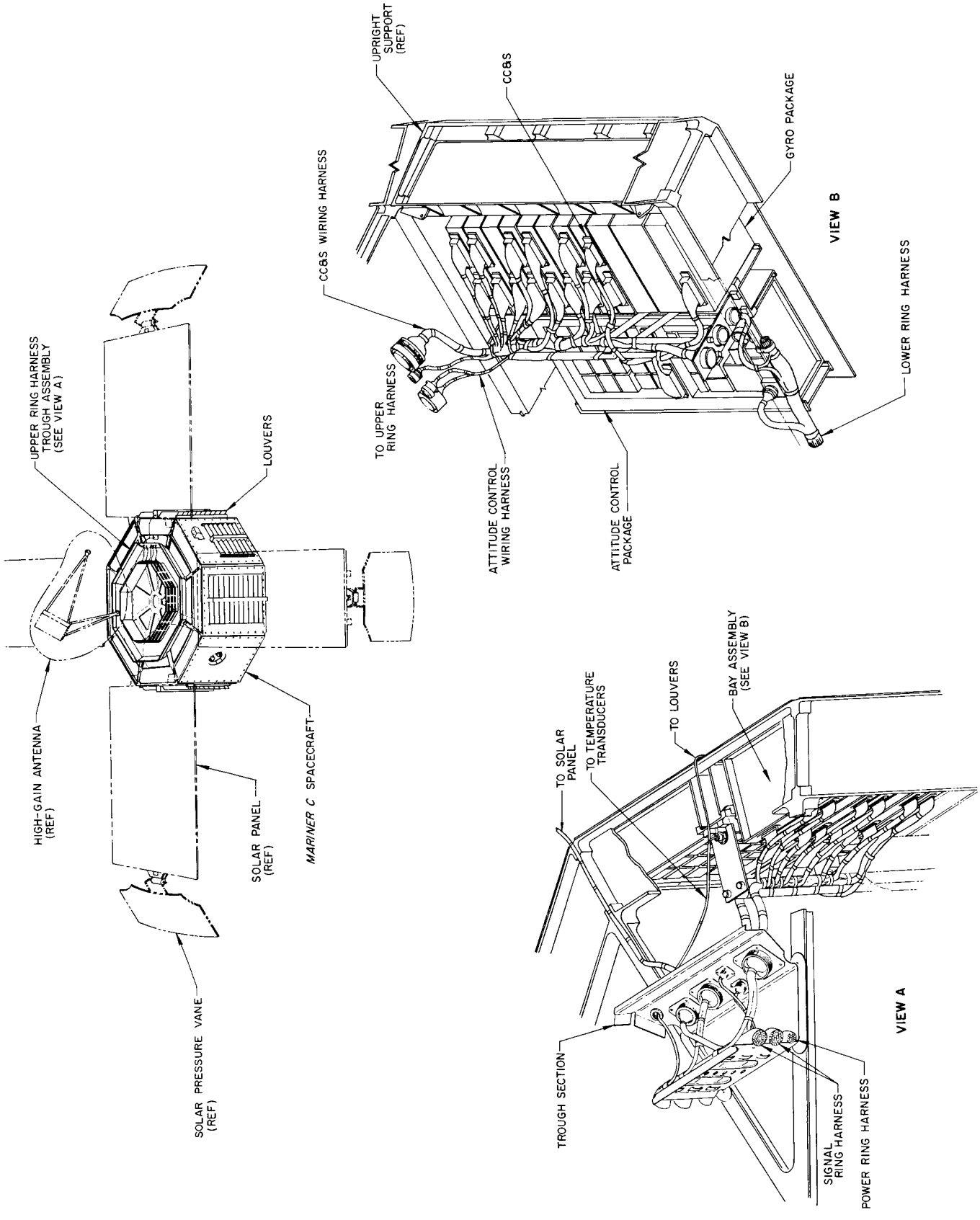

Fig. 14. Basic cabling concept

Measurements have been made of the spectrum of these arc sources as well as the reflectance of temperature control surfaces using established spectrophotometry techniques. By integrating these values with wave length, the total energy absorbed by a given surface in a given arc source can be calculated. As a cross check, an instrument was developed which can accurately measure the absorbed energy directly. By comparing the results from these experiments, it appears that the accumulated errors associated with the spectrometer technique are of the same order of magnitude as the spectral mismatch being investigated. A basic problem arises because spectrometer measurements of the solar energy distribution contain errors consisting of narrow wave bands of energy that have not been identified and are not possible to artificially simulate. Uncertainties of these waveband energies cause many spectrally selective surfaces to be thermally unpredictable. This limits the usefulness of solar simulators, no matter how elaborate, to spacecraft which have spectrally non-selective surfaces or to spacecraft which can tolerate the associated temperature uncertainties. A valid diagnosis of temperature control problems from flight measurements is also comprised by not knowing the actual solar absorptance of the spacecraft.

Four of the *Mariner C* flight temperature measurements have been modified to secure the absorptance of selected surfaces used on the spacecraft. This data will contribute to the interpretation of thermal flight data as well as solar simulator data. The variations in the absorptance resulting from long-term exposure of surface coatings to the solar spectrum and high vacuum conditions also may be deduced from these measurements.

b. Absorptance standard design. The design of the flight standard is similar in principle to the instrument used to measure the absorptance of surface coatings to various arc sources. A cross section of the absorptance standard is shown in Fig. 13. The standard consists of a sample surface which envelops a temperature transducer and two thermostatic switches. The sample is supported and partially encased in a plastic shell which is fastened to a base plate. Internal radiation energy exchange is reduced by reflective shielding.

The thermostatic switches are for the purpose of providing a more accurate in-flight temperature calibration than can be obtained through the telemetry system. The standard requires no electrical power and appears as a

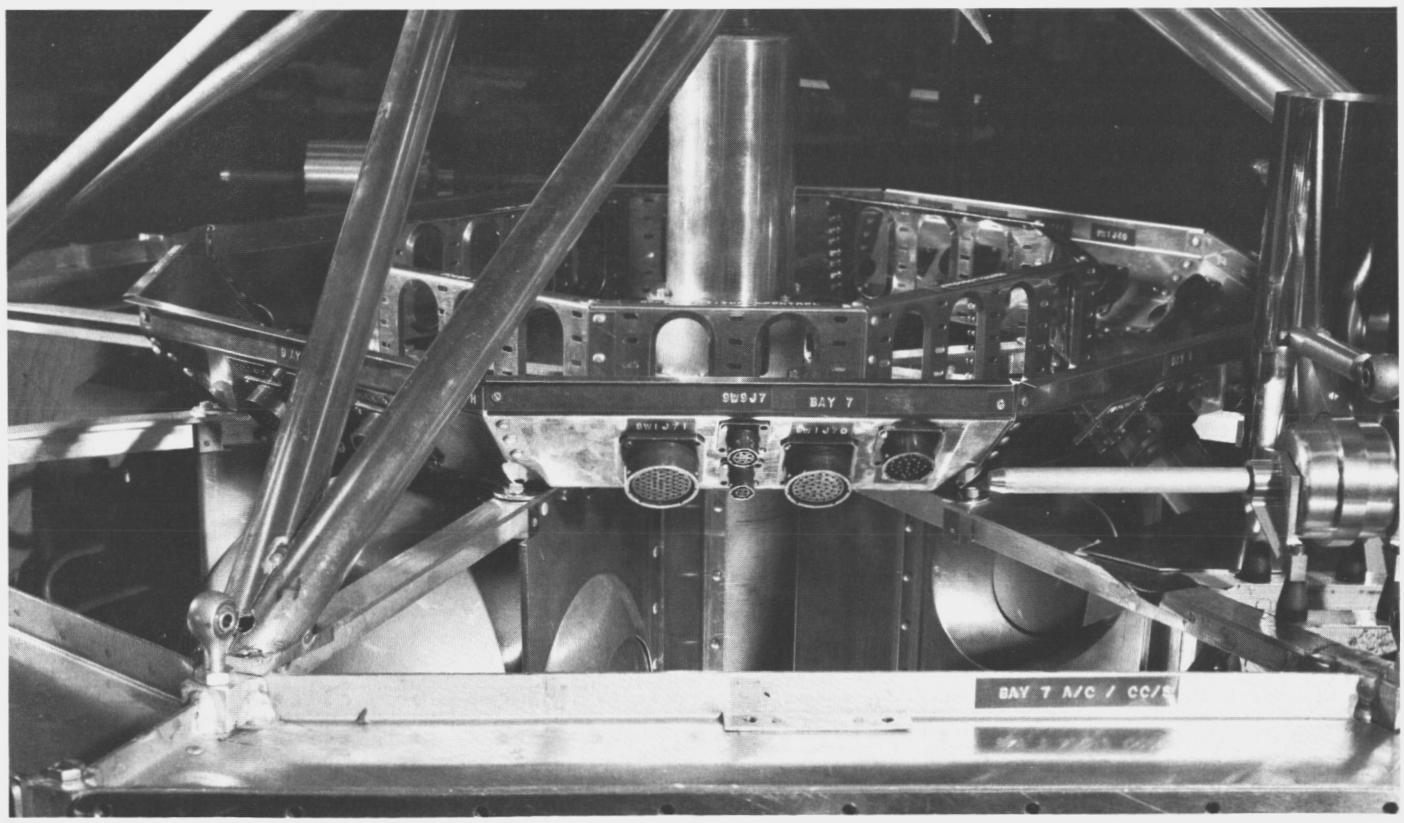

Fig. 15. Upper ring trough in the spacecraft mockup

typical temperature measurement to the telemetry system. The sample temperature will drop during transit to Mars due to a decrease in the solar intensity. At pre-set temperatures the thermostats will switch the signal level of the platinum wire transducer, thus providing the required in-flight calibration. The design of the standard is complete and prototype hardware is being fabricated.

6. Cabling

Numerous changes have been made in the design of the *Mariner* spacecraft cabling to accommodate revisions and relocations of equipment of the various subsystems. However, the basic cabling concept (Fig. 14) has not changed and design and mockup are proceeding. Fig. 15 shows the upper ring trough in the spacecraft mockup with connectors installed.

A tubular case harness support structure has been chosen, in lieu of the box structure shown in a previous *SPS*, in order to facilitate fabrication and inspection of the harness. The tubular structure, which is typical for most cases, is shown with its associated case harness and the adjacent portion of the upper ring harness (Fig. 14). The tubular structure and a rough prototype of the CC&S harness were given flight approval and type approval shake tests on the jig shown in Fig. 16. During the test a simulated attitude control case harness (not shown in the figure) occupied the other side of the jig. No failures in either the structure or wiring were detected and fabrication of a second and more accurate prototype CC&S harness has been completed using a reworked version of the fabrication jig (Fig. 17).

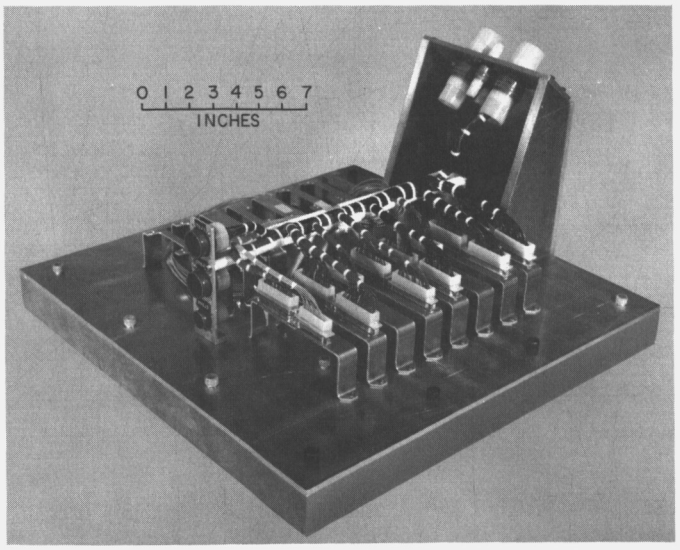

Fig. 16. Case harness shake fixture

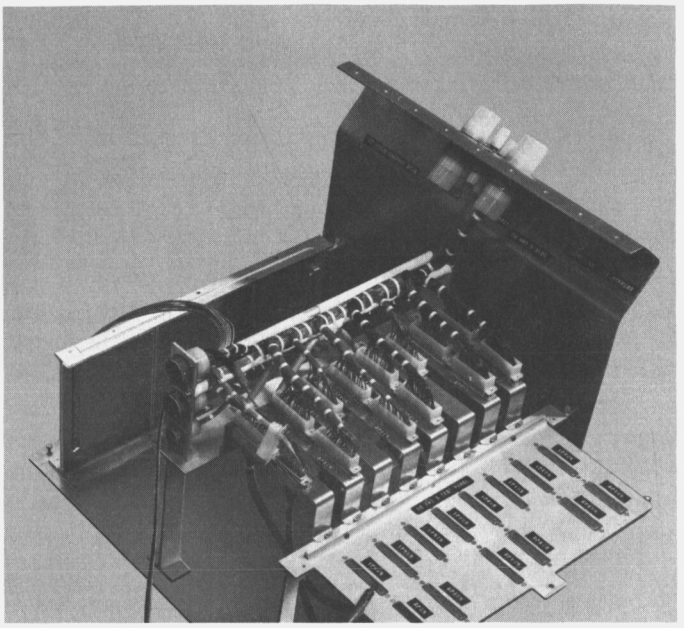

Fig. 17. Case harness fabrication jig

C. Guidance and Control

1. Power Ground Support Equipment

a. Power system test set. The power system test set (STS) for *Mariner C* provides the necessary elements of power monitoring and control to support the spacecraft power subsystem through test operations consisting of: initial power application, power subsystem evaluation, spacecraft system tests, environmental testing, and final integrated system tests conducted just prior to transport to the launch pad. Further, system test sets, along with adaptor racks, are provided for use in the laboratory and flight acceptance testing. The test set is capable of automatic self-test before or *during* any operation in conjunction with the spacecraft or power subsystem. The maximum duration of this automatic sequence is 90 sec, and on successful completion, assures that the monitor, recording, and power control functions of the ground support equipment (GSE) are operating within the required tolerances. Because all self-test simulation is self-

contained, no external equipment is necessary to complete the self-test.

The system test power GSE will incorporate all of the elements of power, monitoring, and control necessary to provide detailed subsystem analysis and records required to support the spacecraft power subsystem in the laboratory and system test areas. In addition, it provides simulation of interfaces that the flight equipment normally (when in the spacecraft) encounters with other spacecraft subsystems.

Fig. 18 shows a functional block diagram of the system test power GSE. The diagram reflects that the design logically divides the equipment into two groups: (1) the monitoring and operator control area, and (2) the various power supplies, simulators, and associated logic and switching networks.

The GSE will be able to test itself rapidly and frequently. A self-test assembly shall be provided to simulate spacecraft voltages and loads monitored and controlled by the GSE. A transfer assembly, on command from the control panel, will select between the spacecraft and self-test assembly. In the self-test mode, a test routine shall be actuated that on completion ensures that the monitor, recording, and control functions of the GSE are operating. No external spacecraft simulation equipment will be required to completely satisfy this test. Also, special physical operations are not required to calibrate the primary tolerance detectors. The monitoring portion of the test set will be capable of self-test during operation of the spacecraft.

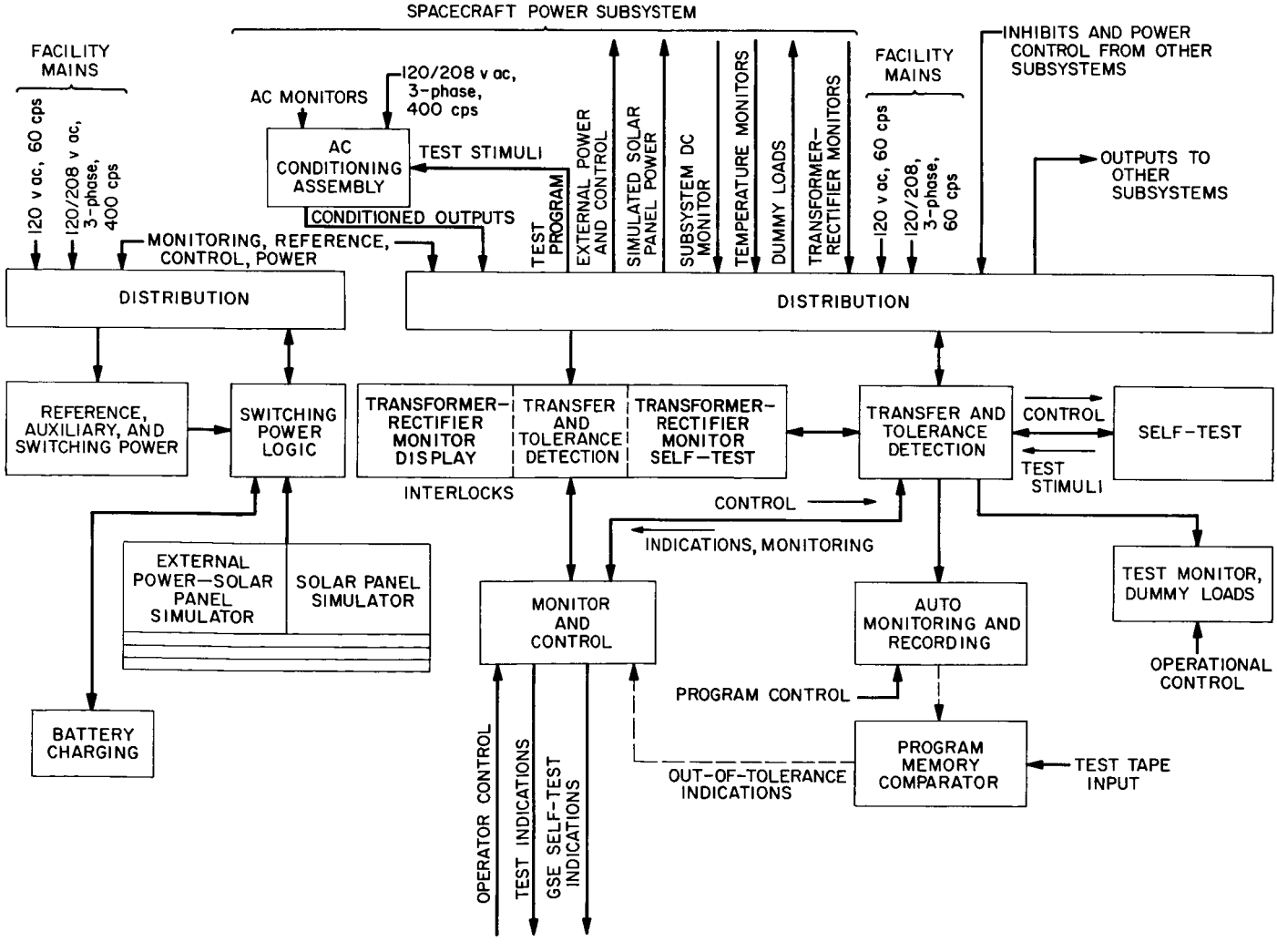

Fig. 18. System test power GSE for *Mariner C*

b. Special remote controls. The power GSE is mechanized to be remotely controlled from other elements of GSE that include: (1) system test—CC&S GSE; (2) environmental test area—CC&S GSE, chamber vacuum sensor; and (3) launch area—CC&S GSE.

The CC&S GSE has the capability in system test and environmental test lab (ETL) to prevent spacecraft power from being applied unless hold-current and relay-position interlocks are satisfied. Once spacecraft power is applied, these two interlocks may be removed to allow the issuance of CC&S commands without losing spacecraft power. If CC&S GSE power is lost, however, spacecraft power will be turned *off* by the power GSE.

The same power GSE interlocks are used to turn spacecraft power *off* in the event of a vacuum chamber failure. Most of the ETL tests are conducted on internal power and because spacecraft power may not be turned off unless the power system is in the external mode, the vacuum fail indication initiates a sequence that transfers the spacecraft from internal to external power and removes external power. Once this action has taken place, the power GSE is *latched* in the *off* position, the remote power control indicator is *on*, and will remain in this condition until the operator manually resets the controls *after* the fail indication is removed.

c. *Functional description of major assemblies.* *Transfer and tolerance detection assembly.* This assembly, on command, selects either the self-test assembly or the spacecraft functions. It is interlocked so that it cannot apply power to the spacecraft during a GSE self-test. Also, should a self-test be performed on the GSE during an operation with the spacecraft, power will not be removed from the spacecraft. All external functions pass through the transfer assembly such that a logical selection between self-test or operate can be made.

The tolerance detectors are located herein. These circuit cards make up a system of primary continuous monitors to detect malfunctions in the spacecraft power subsystem. The output of these detectors is a fail indication on the operator control panel. By separate control the operator may elect to have the fail indication *latch* or not. During automatic self-test the detectors are required to respond to signals that are marginally out-of-tolerance high, out-of-tolerance low, and in tolerance.

If, and only if, all test conditions are satisfied for all detectors, a single self-test *complete* indication is given.

Monitor and control panel assembly. As implied, the control panel assembly presents to the operator controls to place the spacecraft power subsystem and/or GSE into the desired mode. Also, all primary indications affecting the operation and state of the flight and power GSE are displayed. The operator may conduct a GSE self-test, a test in conjunction with the spacecraft power system, or both.

The controls available to the operator include:

(1) Spacecraft switching to external or internal power.

(2) Simulated solar panel power.

(3) GSE self-test (automatic upon initiation).

(4) GSE operate (transfer to spacecraft).

(5) Battery charger enable (allows automatic operation of the GSE charging circuits).

(6) Fail indication latch set.

(7) Manual charge initiate.

Interlocks are provided to prevent the operator from inadvertently damaging the spacecraft or the GSE.

Monitoring displayed at the control panel includes:

(1) Current supplied to the spacecraft from the GSE.

(2) Spacecraft primary system voltage.

(3) Spacecraft battery voltage.

(4) Positive indications for each of the controls listed in the paragraph above.

(5) An out-of-tolerance indication for the primary monitors.

(6) An indication that the *external power* is out-of-tolerance high. (This interlock also prevents switching to external power from either the *off* mode or internal power mode.

(7) An indication that a *remote power control* interlock is in effect which prevents application of spacecraft power.

(8) Positive indications that *GSE self-test* is *complete*, *battery charging* is *required*, and *battery charging* from the GSE is taking place.

Self-test assembly. This assembly provides simulation for all spacecraft power functions monitored or controlled by the GSE. Its test routine is commanded automatically from the control panel assembly upon transfer to GSE

test. During automatic self-test all monitors and tolerance detectors are required to respond to marginal conditions.

Automatic digital monitoring and recording subsystem. Four assemblies make up this portion of the GSE. It is capable of fully automatic, semiautomatic, or manual operation at the discretion of the operator. The monitors are visually presented and permanently recorded on printed tape. Channels are available for 200 inputs which may include AC, DC, and resistance measurements. It is automatically controlled in self-test by the control panel to provide a printed record of the GSE during this mode. A clock assembly is included to provide timed automatic scans at prescribed intervals without an operator, for overnight use or during extended life tests.

Each time an automatic scanning cycle is initiated, the clock assembly records the time on the permanent record. As indicated on the block diagram, it is designed to operate in conjunction with an optional digital comparator assembly for tolerance detection. Modification to existing equipment is not necessary to include these additional assemblies.

Transformer rectifier monitoring and display subassembly. This unit is provided in the power GSE as a central data gathering point for power subsystems used in other than guidance and control flight equipment. With the exception of the data-monitoring subsystem which processes its outputs, the assembly is self-contained. That is to say, it contains monitoring facilities, front panel indications, tolerance detectors, and self-test.

Test monitor assembly. A special test assembly included in the GSE to provide direct access to *all* applicable spacecraft functions (whether simulated or real) for purposes of fault-finding, analog recording, or manual testing.

This assembly also houses dummy loads for the spacecraft power subsystem, and switching controls for simulating spacecraft commands that normally originate in the CC&S or command decoder subsystems.

Switching logic assembly. Provides necessary control, logic, and protection for application of external power, solar panel simulated power, and battery charging.

Auxiliary power supply assembly. Houses auxiliary, switching, and precision reference power supplies required by the spacecraft power subsystem and the GSE. All external functions leaving the GSE are short-circuit protected such that a failure in the spacecraft or associated equipment does not destroy cabling.

Power source/solar panel simulator. Two assemblies are used to provide four separate isolated outputs for simulated solar panel power. These units serve both as the simulator and as a constant voltage power supply for external power/battery simulation. The main regulator is then controlled from a voltage reference source or function generator to provide the mode desired.

d. Secondary power—launch control sets. Fig. 19 shows a functional block diagram of the launch control power GSE. The launch support sets contain all of the basic monitor and control features of the system test equipment but reflect the constraints and design considerations imposed by the launch operation and site. All launch equipment features and mechanizations are found in the system test sets.

2. CC&S Ground Support Equipment

a. Functional description. The ground support equipment (GSE) for the CC&S flight equipment has the following capabilities:

(1) Automatic checkout of the CC&S with a coded printout record of test results.

(2) Manual control of all required CC&S functions for spacecraft system testing.

(3) Preflight monitoring and preparation of the CC&S in the launch complex area.

Capabilities (1) and (2) use identical equipment. Capability (1) is used in the laboratory and capability (2) while the CC&S is installed in the spacecraft. GSE used in the blockhouse is identical and interchangeable with panels found in systems GSE. This accomplishes three important things:

(1) Operators using systems equipment are also familiar with blockhouse equipment.

(2) Spare equipment is provided for the blockhouse by the systems equipment.

(3) Launch complex operating modes and mechanizations are verified during system testing prior to actual launch operations.

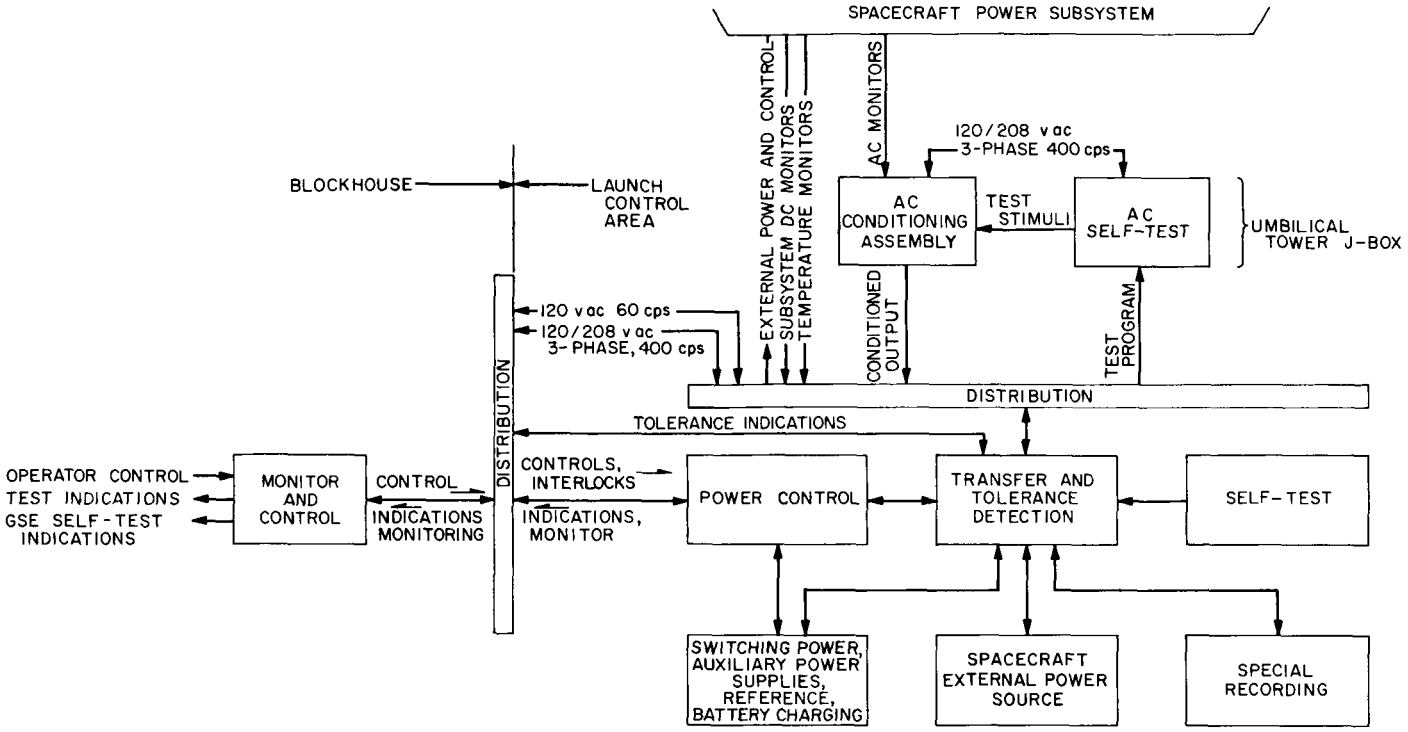

Fig. 19. Launch complex GSE for *Mariner C*

b. Interface characteristics: inputs.

From CC&S direct access through signal conditioner module.

(1) *Relay indicate lines.* These signals are contact closures to ground in the CC&S and provide a visual indication on the GSE of a particular CC&S relay state (set or reset).

(2) *CC&S 1 pps.* A 2-μsec pulse that is stretched in the signal conditioner to 30 μsec and transmitted to the GSE.

(3) *+15 vdc, +28 vdc, and +60 vdc test voltages.* These signals can be monitored through test points on the front panel of the GSE and are also transmitted to the power GSE where they are continuously monitored through a scanner switch.

(4) *Parity check.* A 5-msec transistor opening to the GSE during loading of midcourse maneuver information.

(5) *RF load.* This signal is given to the GSE at the end of the address portion of the command data word and remains on for the balance of the word. The signal is a transistor closure to ground.

CC&S attitude control functions.

(1) *CC&S output command lines.* All attitude control command lines monitored by the GSE consist of opening or breaking a GSE rack ground.

CC&S system functions.

(1) *CC&S output command lines.* All system command lines monitored by the GSE consist of opening or breaking a GSE rack ground.

(2) *38.4 kc.* The CC&S 38.4-kc time base is monitored by the GSE and a printout is generated either upon the application or removal of the signal. Front panel test points are also provided on the GSE for this signal. *Timing accuracy.* The GSE is capable of measuring the basic timing of the CC&S clock to an accuracy of 0.005%.

(3) *+28 vdc monitor.* This signal can be monitored through a test point on the front panel of the GSE.

(4) *CC&S event telemetry.* A 3-msec transistor pulse closure upon the occurrence of all CC&S commands.

CC&S umbilical functions.

(1) *Encounter verify.* A 100-msec contact closure during the update sequence.

(2) *Relay position indicator.* This line monitors the composite reset state of all CC&S output relays.

(3) *CC&S clear indicate.* A contact opening occurring 120 sec after inhibit-release, indicating the CC&S launch counter was clear prior to start of updating sequence.

Power interlock functions.

(1) *Spacecraft power on.* Once relay hold has been applied from the GSE and all relays are reset in the CC&S, this signal can then be given, causing 2.4-kc power to be applied to the CC&S.

c. Interface characteristics: outputs.

To CC&S direct access through signal conditioner module.

(1) *Midcourse clear.* A 50-msec pulse that performs clearing of the maneuver clock.

(2) *10-kc override control.* A contact closure in the GSE commanding a 25 times speedup of the CC&S operation.

(3) *10 kc to CC&S.* A 10-kc signal is injected into the CC&S at the 400 to 1 divider point in the central clock, thus speeding up the CC&S operation by 25 times.

(4) *Master timer speedup input.* A gate signal to the signal conditioner module that causes a 2.5-μsec pulse to be transmitted to the CC&S at a 1-pps rate. This signal is used to speedup the countdown of the CC&S magnetic divide by 2000, which is normally counted down at a rate of one pulse every 3.3 hr. This speedup capability allows a complete system test to be performed in less than an hour.

Signal outputs through the CC&S system cables.

(1) *2.4-kc power.* Input power to the CC&S is 2.4 kc, 100 v squarewave peak-to-peak. This is supplied by the GSE in the absence of spacecraft power.

(2) *CC&S alert.* A 5-msec pulse transmitted to the CC&S before the beginning of each command data word.

(3) *CC&S maneuver command bits.* A 25-msec pulse transmitted to the CC&S for each *one* in the command data word.

(4) *CC&S sync.* A 5-msec pulse transmitted to the CC&S during each bit of the command data word.

(5) *Initiate midcourse maneuver.* A switch closure in the GSE.

Signal outputs through the CC&S umbilical.

(1) *Inhibit counters.* A constant current generator in the GSE supplies 500-ma inhibit current to the CC&S.

(2) *Clear counters.* A constant current generator in the GSE supplies a 1-amp clear pulse to the CC&S.

(3) *Relay hold.* A constant current generator in the GSE supplies 300-ma hold current to the CC&S.

(4) *CC&S actuator inhibit.* A switch closure on the front panel of the GSE.

(5) *Encounter update.* A 100-μsec pulse transmittted to the CC&S at the rate of 10 pps.

Power interlock functions.

(1) *Power off command and CC&S fail indicator.* Contact closures in the GSE, preventing application of spacecraft power unless the CC&S GSE has relay hold applied.

Central clock functions.

(1) *CC&S 1 pps.* Contact closures are supplied to the central clock for 20 msec upon occurrence of the CC&S 1 pps. This signal is transmitted only if inhibit counters are not applied.

3. Attitude Control Ground Support Equipment

The attitude control ground support equipment (GSE) consists of the system test set (STS) (Fig. 20) and launch complex set (LCS) (Fig. 21).

a. System test set. The attitude control system test set (A/C STS) is required to completely test and evaluate the A/C system. It will perform this task by using the STS in integrated spacecraft system tests, and subsystem tests in conjunction with the A/C spacecraft system interfaces. All tests will be performed by using low-risk high-reliability techniques developed on previous programs and in the laboratory. These tests will be supplemented with the Laboratory Test Set (LTS) whenever necessary.

All components of the STS shall be self-tested from the test console. These self-test features shall not distract from the normal operation of the STS. No self-test feature will be allowed to react with flight equipment.

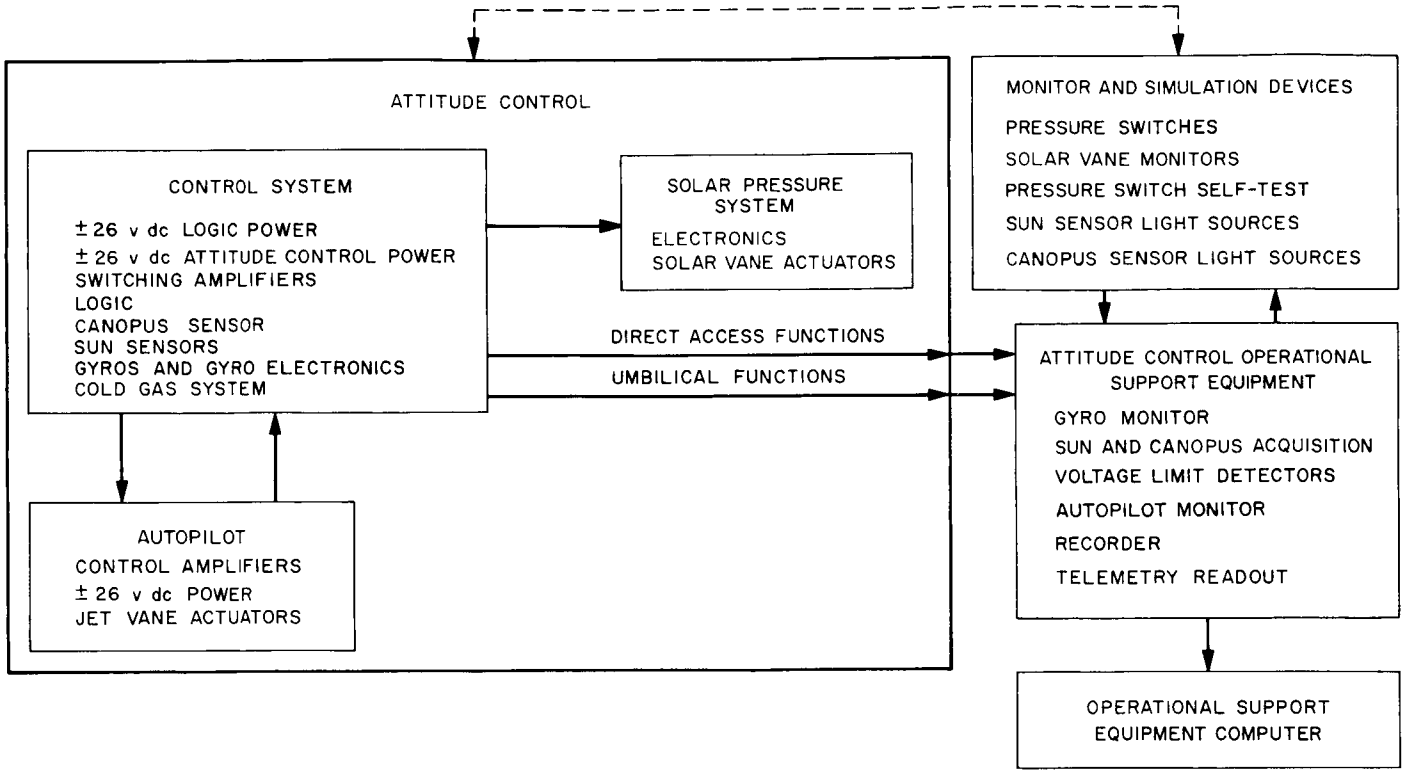

Fig. 20. Attitude control system test set

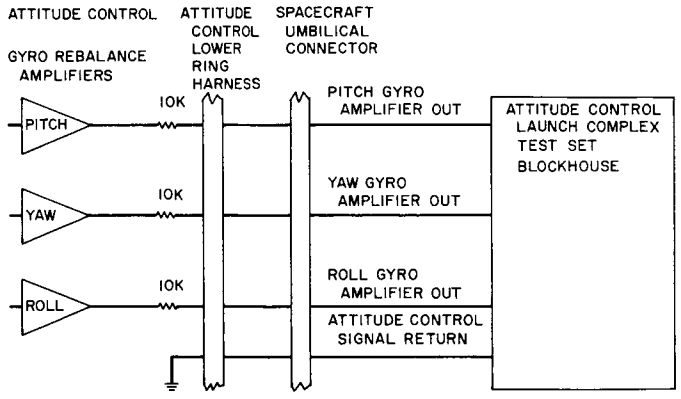

Fig. 21. Attitude control launch complex test set

Inputs.

(1) *From the gyro loops.* Voltage monitoring of the pitch, yaw and roll rebalance amplifier outputs to check and test A/C system phasing, switching levels, and gyro loop gains. Switching state monitoring of gyro loop power on command function will detect many logic switching modes and allow step-by-step logic checkout in conjunction with other logic functions.

(2) *From transformer-rectifier power supplies.* Voltage detection and marginal testing of logic, gyro, A/C, Canopus tracker, Sun sensor, and autopilot power will allow long-term parameter shift analysis and failure mode detection of all pertinent transformer-rectifier supplies.

(3) *From the cold gas jet valves.* Indication of flow of cold gas from the twelve jet valves are used to check and test the A/C system phasing, switching levels, and switching amplifier gains.

(4) *From integrating capacity cycling.* Detection and marginal testing of voltage integration during capacitor forming for midcourse maneuver to test for voltage application and circuit operation.

(5) *From the Canopus sensor brightness (intensity) analog voltage measurement.* This function allows parameter shift long term analysis and logic check and test of the A/C and Canopus sensor interface. *Canopus acquisition inhibit.* Gives capability to test A/C logic during Sun acquisition, and midcourse maneuver. *Canopus cone angle.* Analog voltage measurement corresponding to electrical cone angle setting of the Canopus tracker field of view will be

compared to the STS stimulus readout for comparison tests.

(6) *From the switching amplifiers.* Pitch and yaw position error signals will be visually displayed as analog voltage measurements representing the pitch and yaw Sun sensor outputs. Marginal testing of the pitch and yaw switching amplifier dead bands will be made using these functions in conjunction with the activation of the cold gas jets. The roll position error signal will be visually displayed as an analog voltage and will represent the roll search command voltage and the Canopus sensor roll-error signal. Marginal testing of the roll switching amplifier will make use of this function in conjunction with the roll cold gas jets.

(7) *From the autopilot jet vane actuators.* Analog voltage measurements using visual displays of jet vane angle deviations from the four jet vane actuators during all phases of the flight sequence to test the autopilot phasing and operation with respect to A/C system.

(8) *From the solar pressure guidance system.* Analog voltage measurements using visual displays of the four solar sail angles during all phases of the flight sequence to test the A/C to solar pressure system relative phasing and operation.

Outputs.

(1) *To the acquisition and cruise Sun-line orientation photocells (Sun sensors).* Individual Sun simulation sources (lamps) for each of the sixteen photocells to test phasing and operation of the A/C Sun-line reference system. Each stimulus will be housed in a light tight hood containing the proper number of stimuli to test a given unit, and shielded from one another to eliminate crosscoupling and extraneous lighting. Capability will exist at the STS console to dependently vary the cruise stimuli in an analog fashion during subsystem testing and/or calibrations. On and off operation will also exist and be used during system testing. Intensity controls and stimuli monitors will completely control these functions.

(2) *To the autopilot power control relay.* Capability will exist to turn on the autopilot electronics by energizing the power on relay from the STS through the direct access connector. Checkout of the autopilot can be accomplished during flight readiness preparations using this capability.

(3) *The Sun gate photocells (sensor).* A simulated Sun source (collimated light) housed in a holding and cooling fixture to test the Sun-line logic portion of the A/C system. *On-off* operation at all times is controlled from the test console.

(4) *To the Earth detector photocell (sensor).* A simulated Earth source (lamp) variable for calibration purposes to test the Canopus–Earth logic portion of the A/C system. Intensity controls and stimulus monitor will completely control this function.

(5) *To the Canopus sensor.* Simulated Canopus images consisting of fifteen collimated light sources in a light-tight holding and alignment fixture to test the Canopus acquisition system. Capability will exist to vary the intensity of these images from the test console.

(6) *To the pitch, yaw and roll gyro torquer.* Capability will exist to command the integrating gyros to oppose or compensate all commanded turns by position feedback loops.

(7) *To the computer.* Capability will exist to monitor operation of the A/C system through isolated outputs to the computer data system. These outputs shall in no way distract from the A/C operation or interfere with A/C system operation and shall be available at the STS console only.

Mechanical boundaries.

The STS is comprised of one 6-ft console which will conform to JPL specifications. Twelve pressure-sensitive switches are used to monitor the A/C cold gas valves. In conjunction with these are twenty-four gas check valves and a small compressed gas supply to facilitate self-testing. Four Sun sensor test assemblies, each containing four stimulus lamps, are used to test the acquisition and cruise Sun sensors. Two derived rate reset sensor test assemblies, each containing two stimulus lamps, are used to test the derived rate networks. There are one Sun-gate test assembly containing a collimated light source and one Earth-detector test assembly containing one stimulus lamp. Four analog position monitoring devices are used to monitor the solar vane movements. There are one Canopus and Sun shutter test assembly containing fifteen collimated and one noncollimated stimulus lamps which are used to test the Canopus sensor at all five cone angles, and at three set position offsets.

b. Launch complex test set. The attitude control launch complex test set (A/C LCS) is required to observe critical subsystem functions, and allow measurement of these

functions. It will perform this task by using a portion of the STS for maximum reliability and accuracy.

Inputs.

From the pitch, yaw and roll gyro rebalance amplifier outputs. Constant analog voltage monitoring and precision measuring capabilities to observe gyro loop gain and gyro loop closure. These functions are monitored from power turn-on to liftoff.

Outputs.

All outputs are self-contained self-test voltages which can be operated at any time without affecting the flight equipment.

4. Spacecraft Power

a. Power system. The *Mariner C* power system represents an extension of the technology developed on the *Mariner 2* program. Considerable effort is being expended in the improvement of the design features and fabrication techniques for the solar panels. Extensive prototype panel testing is now planned. For the same weight as the *Mariner 2* battery, the *Mariner C* battery should have 33% greater capacity. The major difference between *Mariner 2* and *Mariner C* will be in the mechanization of the power system. As was discussed previously in *SPS 37-20*, the *Mariner C* will use a redundant booster-regulator and two 2.4-kc inverters. The power subsystem will also incorporate switching and logic functions both for the effective management of spacecraft loads and the proper utilization of the redundant booster-regulator. The power system telemetry measurements have been selected to provide the necessary intelligence for the management of system loads by ground command, if required.

b.* Mariner C *solar panels. Space Technology Laboratories (STL) has been selected to manufacture the *Mariner C* flight solar panels. It is planned that two prototype and four type approval panels will be constructed and tested prior to the fabrication of flight solar panels. Two of the type approval panels, T/A-3 and T/A-4, will be constructed by STL.

Planning for the construction of the first *Mariner C* prototype panel, MC P-1, has been initiated and drawings, schematics, and process specifications are in preparation. It is anticipated that many of the process specifications employed in the development of the *Ranger* Mark IV solar panels can be modified and incorporated into the *Mariner C* program.

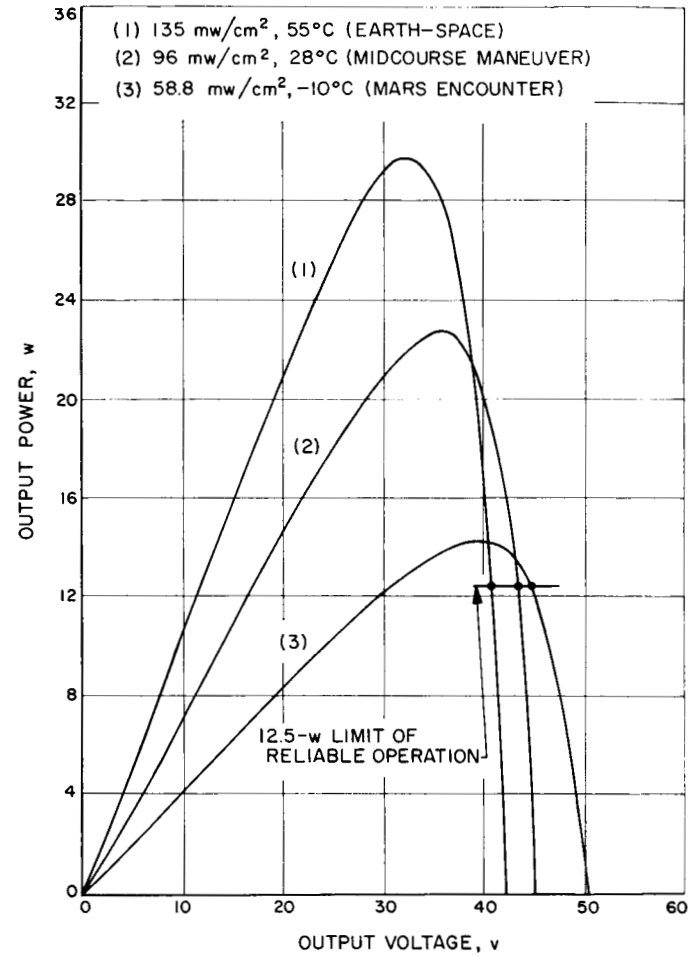

Fig. 22. Nominal power versus voltage, Cell Section 1764, *Mariner C* solar panel

The *Mariner C* prototype solar panel, MC P-1, will consist of 7,056 p/n, 1 × 2 cm, silicon solar cells. The panel will be separated electrically into four isolated units of 1,764 cells each. The cells will be series-parallel connected to produce the expected power-voltage characteristics shown graphically in Fig. 22. The output power of the four sections of the panel is designed to be supplied to the power switch and logic assembly through redundant wiring. Each section is shunt regulated by 6 series-connected zener diodes to limit the output voltage of the panel to a maximum of 50 v.

Presently, three types of cell interconnection techniques are under evaluation for MC P-1. These are shown in Fig. 23. The lower group of cells are of the Mark IV configuration in which connection to the P-contact of the

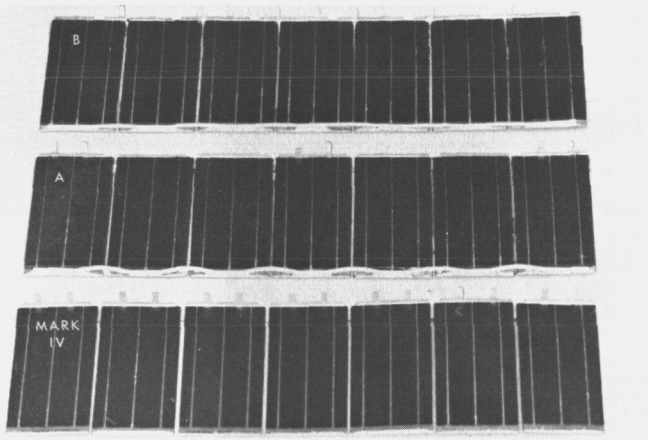

Fig. 23. *Mariner* C solar panel cell interconnection evaluation submodules

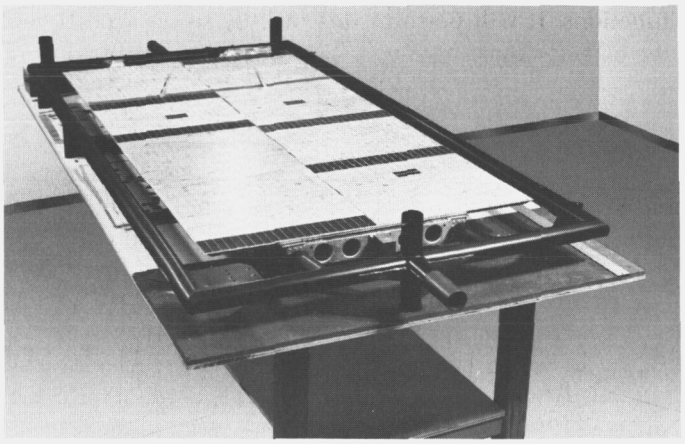

Fig. 24. *Mariner* C prototype solar panel

cells is made after the cells have been mounted on the panel. In the two groups of cells above the Mark IV submodule, the P contacts are paralleled prior to mounting the module on the panel. While the latter two groups of cells appear similar to the Mark IV cells, they have exhibited decided advantages in that it is possible to reduce the number of operations necessary after the submodules are mounted on the panel when cleaning and cell repairs are relatively difficult. It is estimated that after the cells are mounted on the structure a Mark IV MC P-1 submodule would require approximately 14,500 solder connections, two extensive cleaning operations, and the bonding and curing of the filter glass to the cell. It is expected with the other type submodules, soldering operations on the structure could be substantially reduced. Cleaning will be limited to one relatively simple operation and the filter glass will be bonded to the cells prior to mounting the cells on the structure. All of these advantages should provide increased reliability and a substantial increase in the efficiency of the fabrication of *Mariner C* solar panels.

Samples of various submodule configurations have been assembled to 10¼ × 12 in. aluminum sections which resemble the structure of the *Mariner C* panels and have been tested for compatibility of materials and the effects of an acoustic environment on the mechanical properties of the cell-structure composite. The electrical output of the cell assemblies was measured at Table Mountain before and after acoustic testing. It was noted that 10% of the cells subjected to the acoustic environment, regardless of the submodule configuration, developed apparent "hair-line" crazing; however, no degradation of the electrical output of these sections was measured as a result of these tests.

A prototype structure of the *Mariner C* panel has been delivered to JPL by the manufacturer, Ryan Aerospace Corporation. Two 7 × 21 cell assemblies of each of the three types of submodules (Fig. 23) have been mounted on this panel including a mock-up of the required panel harnessing. Pieces of aluminum, simulating the weight and size of solar cell assemblies, were bonded to the remainder of the panel surface. The completed panel is shown in Fig. 24. This prototype structure will be subjected to special structural evaluation testing during the latter part of April and will aid in the selection of the MC P-1 submodule assembly configuration.

The power input to the power regulator assembly from the solar panels of *Mariner C* will be maintained below 50 v dc by a zener diode shunt regulator. Each of the 16 isolated sections of the *Mariner C* solar panels will be individually shunt regulated by 6 zener diodes connected in series. This will require 24 diodes to regulate one panel and a total of 96 to regulate the total solar panel power source. The zeners will be mounted on the underside of the spar assemblies of the panels and will depend upon heat sinking to the panel and radiation to space of the power dissipated in the diodes for temperature control.

There are three operating conditions that must be considered in determining the power dissipation requirements for the shunt regulator. These are:

(1) The transient period when the spacecraft leaves the Earth's shadow. The solar panels could be Sun-oriented at an initial temperature of −100°C, or lower.

(2) Midcourse maneuver period when the spacecraft could be oriented such that the solar panels would cool to temperatures below −100°C. Rapid Sun acquisition could result in a large current flow through the zeners.

(3) Cruise mode near Mars when the low operating temperature (−10°C) of the solar cells will increase the cell voltage. A continuous dissipation of approximately 25 w could occur in certain sections.

The Dickson Electronics Corporation zener 50SZ7.5D has been tentatively selected for use in the *Mariner C* shunt regulator. The 50SZ7.5D has a nominal voltage of 7.5 v at 1.7 amp current (12.5-w dissipation) and a 42°C junction temperature (30°C stud). Six of these units would be connected in series across each section of the power source. The total voltage would be 45 v at 1.7 amp and 42°C junction temperature. Assuming a maximum temperature coefficient of +50 mv/°C, the zener voltage would increase to 50.5 v for a junction temperature of 150°C.

c. **Mariner C *battery.*** A battery is required for this mission to supply the spacecraft secondary power during prelaunch, launch, Sun acquisition, midcourse maneuver periods, and possibly during planet encounter. The battery chosen for this mission is an 18-cell, sealed, rechargeable silver-zinc system, and is presently undergoing design and development.

Battery design. Table 1 lists the battery characteristics in comparison to the battery flown in *Mariner 2*. The increase in capacity is possible because of the reduced maximum load current from 18 to 10 amp. In turn, this current reduction was made possible by eliminating all direct loads on the battery, particularly the squib firing currents, which were pulse loads of about 10 amp.

Reorientation of one-half of the battery cells was undertaken because limited test data showed that cells which were charged and discharged in the inverted position had a shorter life than those kept upright. While a flight battery is usually under load or charge for less than 2 hr before leaving the Earth's gravitational field, elimination of inverted cells eliminates this type of battery degradation.

Changes in materials used for battery and cell cases were made to decrease weight and increase structural strength.

Table 1. Battery characteristics

Detail	*Mariner 2*	*Mariner C*
Weight, lb	33	33
Number of silver-zinc cells	18	18
Voltage regulation, v	25.8 to 33.3	25.8 to 33.3
Maximum voltage on charging, v	36.0	36.0
Float charge capability	Yes	Yes
Minimum capacity, w-hr	900	1200
Maximum load current, amp	18	10
Maximum charging current (flight), amp	1.0	1.0
Maximum charging current (GSE), amp	2.0	2.0
Expected operating temperature, °F	50-140	40-120
Storage life at 30-50°F, yr	1	1
Charge/discharge cycles	5 or more	5 or more
Battery isolation	Diodes & fuse	Diodes & fuse
Orientation of cells on Earth	9 cells inverted	None inverted
Battery case material	Aluminum 6061	Magnesium ZK60
Cell case material	Bakelite RMD-4511	Cycolac T-2502
Cells per molded unit	5	3
Capacity loss per month at 90°F, %	4	1
Temperature transducers	1 GSE 1 telemetry	1 GSE 1 telemetry

Temperature. The temperature profile of the battery during the *Mariner C* mission is shown in Fig. 25. Fig. 26 shows how retention of battery capacity varies with temperature under storage conditions. Thus, during the last months of the flight, the battery charger may be turned off, if this power is needed for other purposes, without losing more than one or two percent of the battery capacity.

Simulated life test. Since the *Mariner C* battery is quite similar to the one flown on the *Mariner 2* with regards to its temperature characteristics, a 9-cell *Mariner 2* type monoblock is being tested under a *Mariner C* temperature profile. The purpose of this experiment is not only to observe the temperature responses during the 240 days simulated flight but also to determine the power sharing capabilities at planet encounter. The monoblock has performed normally through the launch, acquisition, and midcourse phases, and is now in cruise mode. As of April 24, 117 days of flight have been completed. The upper limits of the temperature band of Fig. 25 is being followed for this flight. At the end of an eight month simulated mission, the monoblock temperature will be dropped from 60°F to a worst case condition of 40°F, and the battery will be discharged to depletion in the share mode.

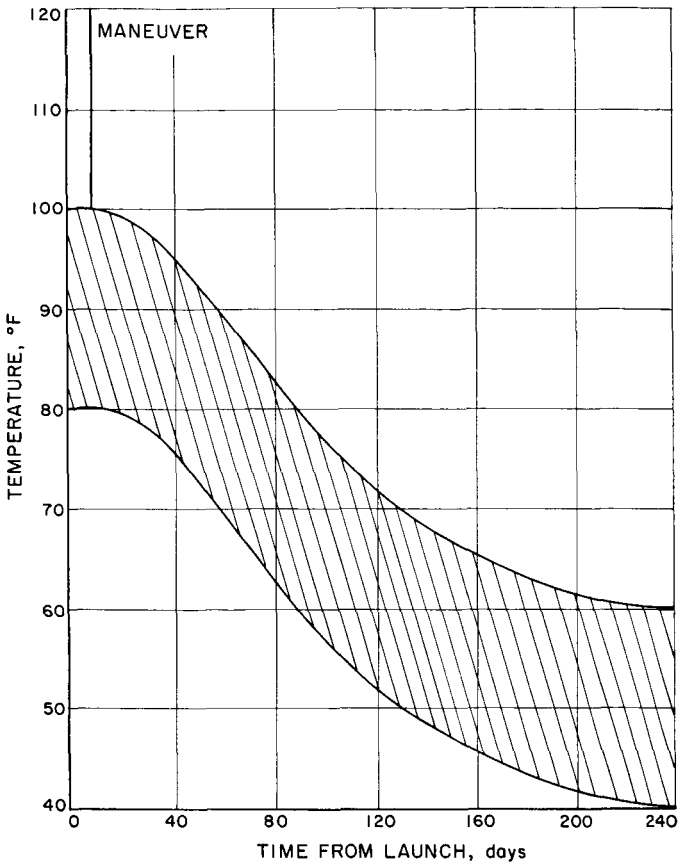

Fig. 25. *Mariner* C battery temperature estimate

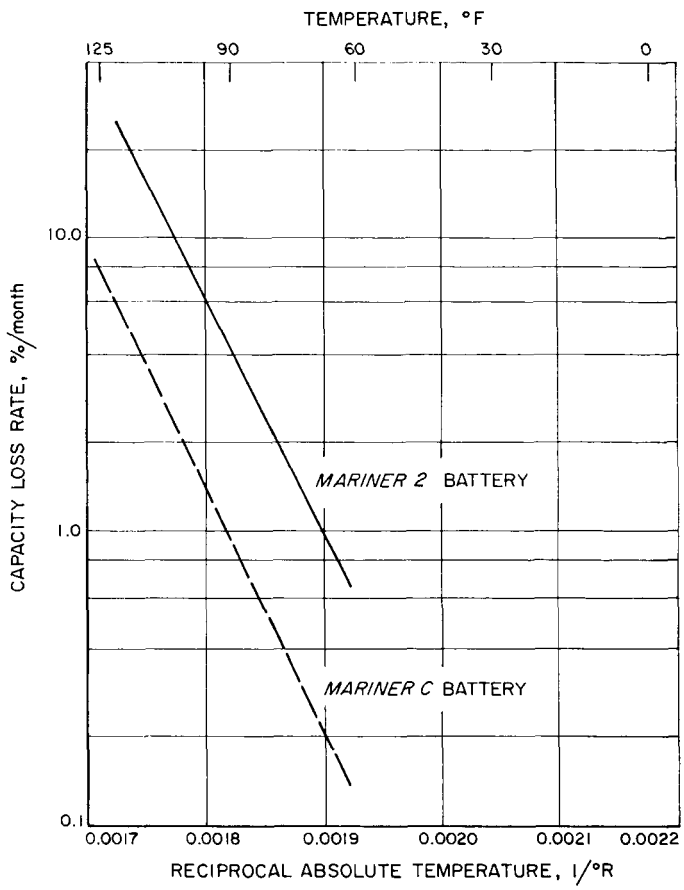

Fig. 26. Preliminary estimate of storage loss for *Mariner* batteries

d. Electrical conversion equipment. The electrical conversion equipment for the *Mariner C* spacecraft is contained in two assemblies. The primary input power from the solar panels and battery is first routed to the power regulator assembly, Case VIII. Regulated DC power from Case VIII is then routed to Case I for the several inverters to provide the various types of power used on the spacecraft.

Case I—power assembly. The power equipment contained in the Case I assembly includes the following seven subassemblies plus the two pyrotechnic control packages:

(1) Power distribution subassembly.

(2) Power synchronizer subassembly.

(3) Battery charger subassembly.

(4) 2.4-kc inverter subassembly for main loads.

(5) 2.4-kc inverter subassembly for maneuver loads.

(6) 400-cps, single phase inverter subassembly.

(7) 400-cps, three phase inverter subassembly.

Case VIII—power regulator assembly. The power regulator assembly is a composite assembly including the functions of input power selection, DC power regulation, and power telemetry conditioner. The composite assembly design was selected to obtain better heat sinking of power components and better integration of this portion of the power system. The one-piece chassis is the Case VIII member of the spacecraft structure. All components and circuit boards are mounted directly to the chassis instead of being packaged in separate subassemblies.

The power regulator receives power inputs from the solar panels, the spacecraft battery, and the GSE external power supply. A power transfer switch controls the choice between the GSE external power and the internal battery. The control lines for these switch and monitor lines from all power conditioners are routed through direct access or umbilical connectors to the GSE equipment.

Each of the solar panel sections and the battery are connected through separate series diodes to provide pro-

tection against a system failure in case one element fails. These diodes also function as an *or* circuit selector to supply power from the higher voltage source. The diodes permit power to flow from both sources during heavy loading periods in a sharing mode.

The summing point of the several input diodes is the unregulated DC power bus. From here the power is routed to the booster regulators, to the communications converter, and to the battery charger.

Booster characteristics. The booster regulator is a switched-mode feedback regulator. A block diagram is given in Fig. 27. A magamp operating from an amplified error signal is used to control base drive pulse width to a pair of power transistors. These transistors, which operate in a push-pull amplifier circuit, boost the input voltage when switched on. The resulting quasi-square wave is added to the input voltage. This wave shape is filtered to yield a constant 52-v dc. The efficiency of such a circuit is much higher than an equivalent series regulator. Efficiency as a function of input voltage is indicated in Fig. 28.

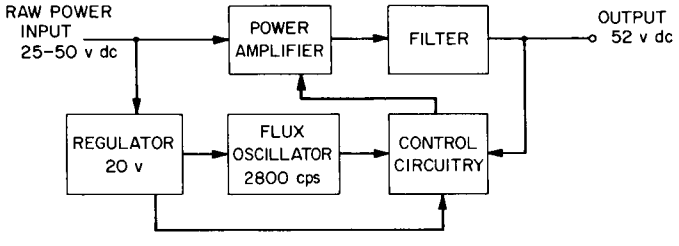

Fig. 27. Booster regulator block diagram

Regulation of the booster for variations of input voltage, load, and temperature is better than 1%. Typical values are shown below in Table. 2.

Table 2. Booster regulation

Input voltage, v	Load, w	Temperature, °F	Output voltage, v
25	27	−4	52.4
25	110	↓	52.2
52	27	↓	52.3
52	110	↓	52.2
25	27	78	52.2
25	110	↓	52.1
52	27	↓	52.3
52	110	↓	52.0
25	27	158	52.0
25	110	↓	51.7
52	27	↓	52.0
52	110	↓	51.8

The booster regulator is capable of handling loads between 25 and 150 w with an input voltage range from 25 to 52 v.

Booster switching. Under normal flight conditions the main booster will handle all cruise and encounter loads

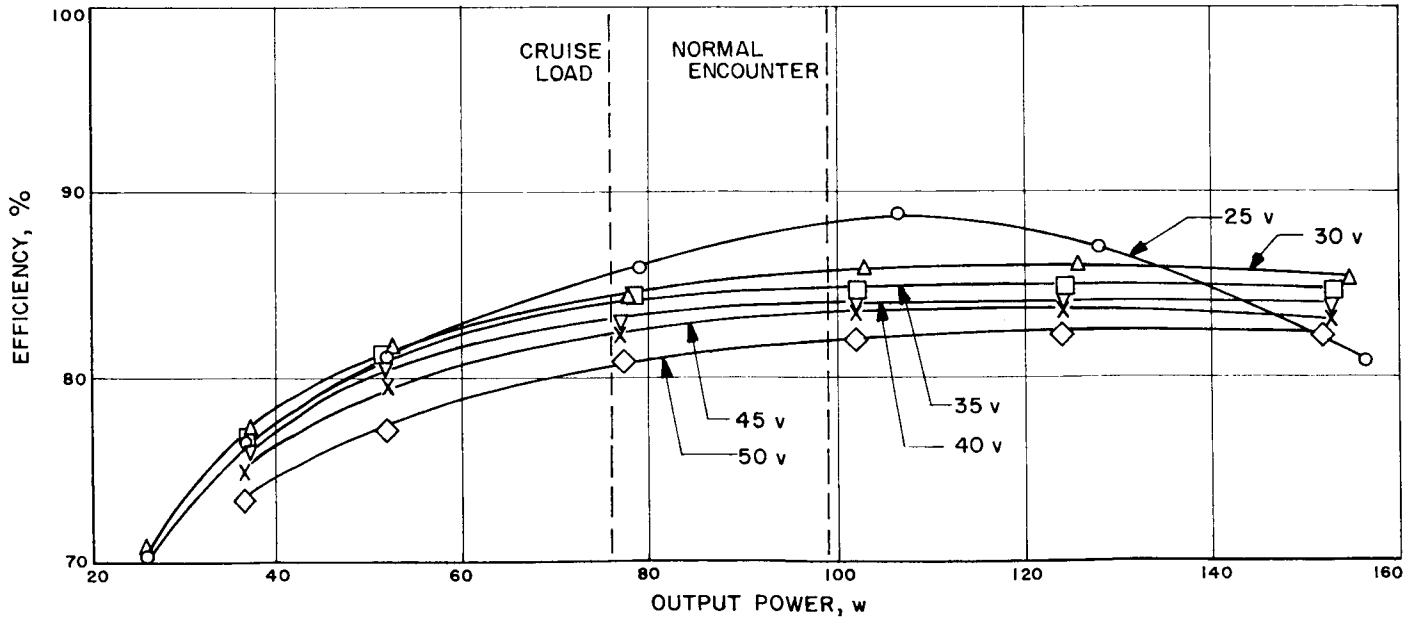

Fig. 28. Booster regulator efficiency versus load as a function of input voltage

Table 3. Booster switching data

Temperature, °F	High voltage, v	High voltage time delay, sec	Output booster 1	
			Low voltage, v	Low voltage time delay, sec
0	57.8	10	43.2	11
72	58	10	43	9
150	57.7	10	43.3	9

while the maneuver booster supports maneuver loads. If the main booster fails, the maneuver booster will be switched to handle all spacecraft loads as indicated in Fig. 29. The switching action is initiated by a tolerance detector. If, for a period of 10 sec, the output of the main booster is greater than 58 v or less than 43 v, the tolerance detector will energize relays which remove the main booster from the circuitry and replace it with the maneuver booster. Because a booster can fail and draw normal amounts of power from the power switch and logic, fusing of the inputs of the boosters is inadequate, hence the switched inputs.

The operation of the switch-over circuitry is quite temperature stable, as can be seen in Table 3.

Mariner C *telemetry*. Three criteria were used in selecting the telemetry measurements to be made and the channel assignments in the power subsystem. Listed in order of importance, these are:

(1) Measure those quantities that will best evaluate the state of the power subsystem.

(2) Arrange the channels in such a way that related parameters (battery voltage and battery charger current, PS&L output voltage, and booster regulator input current, etc.) are closely time related in the telemetry sequence.

(3) Arrange the channels in such a way that if a deck switching failure should occur meaningful data will still be received.

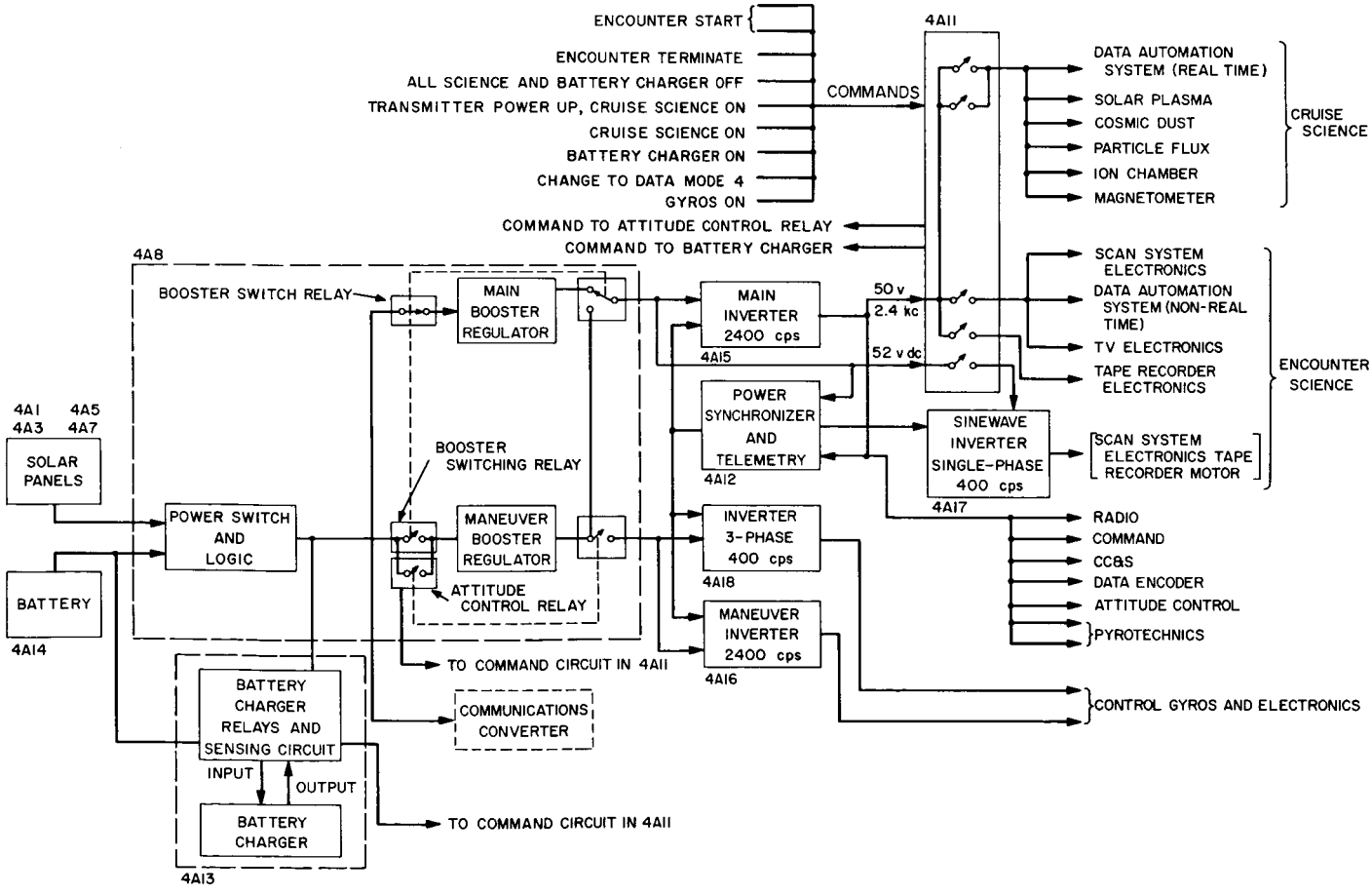

Fig. 29. *Mariner* C power subsystem functional block diagram

Using these criteria, the following telemetry assignments were defined:

Channel	*Measurement*
109	PS&L output voltage
203	Main booster regulator output current
204	Maneuver booster regulator output current
205	Total booster regulator input current
206	Battery voltage
207	Communication converter load current
216	Battery charger current
221	Solar panel 4A1 current
222	Solar panel 4A5 current
223	Solar panel 4A3 current
224	Solar panel 4A7 current
225	Battery current drain
226	2.4-kc inverter output current
227	2.4-kc inverter output voltage
407	Power regulator assembly temperature
409	Solar panel 4A1 front temperature
415	Standard cell current
416	Radiation resistant cell current
417	Standard cell voltage
428	Battery temperature
429	Solar panel 4A5 front temperature

In the event of a deck switching failure, one of the following sets of measurements will be available:

Set 1:

(1) PS&L output voltage.
(2) Solar panel 4A1 temperature.
(3) Solar panel 4A5 temperature.
(4) Main booster regulator output current.
(5) Maneuver booster regulator output current.
(6) Total booster regulator input current.
(7) Battery voltage.
(8) Battery charge current.
(9) Communication converter load current.
(10) Battery temperature.
(11) Standard cell current.
(12) Standard cell voltage.
(13) Radiation resistant cell current.
(14) Power regulator assembly temperature.

Set 2:

(1) Inverter output voltage.
(2) Inverter output current.
(3) Battery current drain.
(4) Solar panel 4A1 current.
(5) Solar panel 4A3 current.
(6) Solar panel 4A5 current.
(7) Solar panel 4A7 current.

5. Attitude Control and Midcourse Guidance

The following discussion is a summary of the progress of the research and development activities in the areas of:

(1) System requirements and design (pitch and yaw acquisition, roll acquisition, and attitude control gas requirements).

(2) Celestial sensors (Star tracker–Canopus, and Sun sensors).

(3) Inertial sensors (gyro control assembly).

(4) Actuators (gas system leak test).

a. Pitch and yaw acquisition

Derived rate acquisition. In *SPS 37-20,* the results of an analog computer study of derived rate acquisition were presented. These results were obtained from the analysis of an ideal, single-axis system with requirements determined by *Mariner C* parameters. In that study it was indicated that further analysis would be made, including better simulation of the control system. This has been done, and significant results have been obtained, indicating that derived rate acquisition on more than one axis at a time is, at best, impractical. The first part of the new analysis was devoted to the optimization of the single-axis case, and the second part to an approximation of a two-axis acquisition.

Single-axis optimization. The block diagram in Fig. 30 illustrates the derived rate acquisition system. Negative feedback through a lag around the switching amplifier furnishes the necessary damping for acquisition. The direction (although not the magnitude) of the spacecraft rate is determined by the switching amplifier output, and the lag with a long time constant approximates an integrator. Hence, the derived rate signal is a "pseudo" rate feedback system, to provide damping.

To establish limit cycle operation a "minimum on time" network holds the jets on for 20 msec, irrespective of signals calling for shorter pulses. Therefore, a limit cycle is established with a rate deadband determined by minimum on time, and a position deadband determined by the switching amplifier.

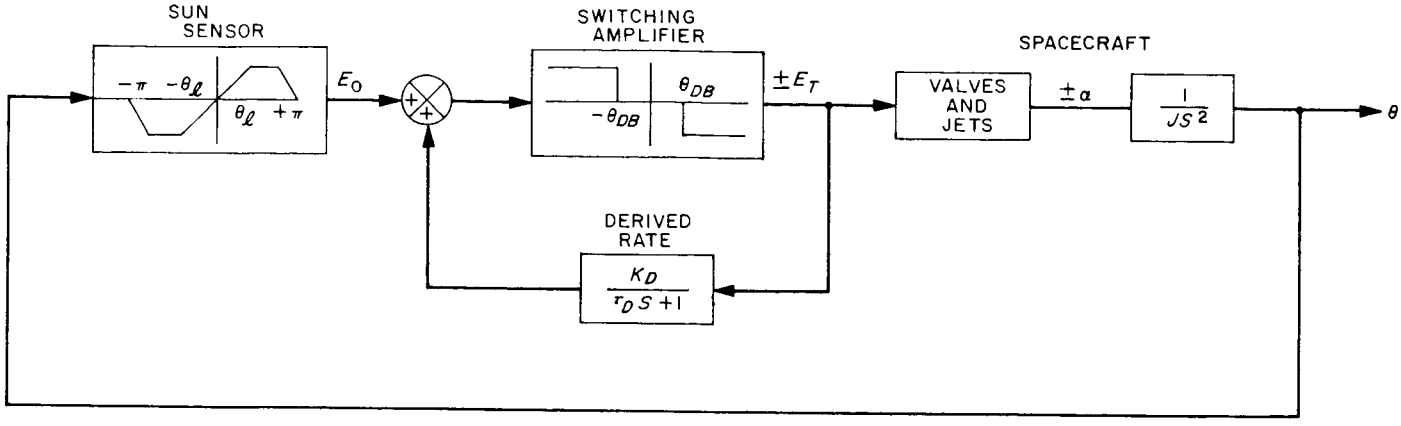

Fig. 30. Idealized derived rate system

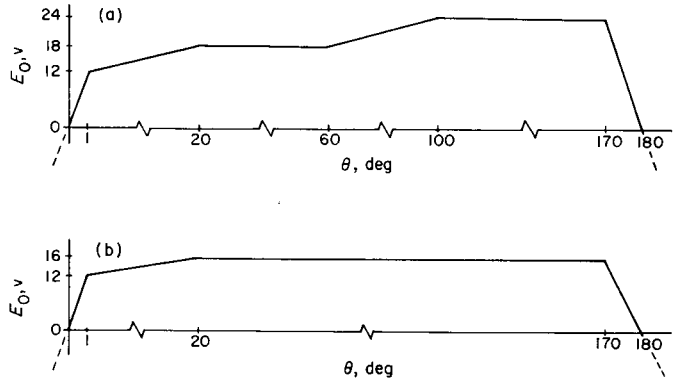

Fig. 31. Sun sensor characteristics

System parameters. The system parameters, determined by *Mariner C* requirements, are as follows:

α = spacecraft controlled rate = 0.2 mrad/sec

θ_{DB} = switching amplifier deadband = $\pm$8.0 mrad

The Sun sensor characteristic that is used is illustrated in Fig. 31a. This sensor is the mechanization which approaches the optimization necessary; that is, a linear region of approximately $\pm$20 to $\pm$40 deg. Fig. 31b represents a possible alternative to determine the effects of a lower saturation level.

A derived rate reset sensor is used to allow the derived rate feedback to more effectively track the position signal through the rear null of the Sun sensors.

Analysis results. The analysis results are summarized in two plots shown in Figs. 32 and 33. Fig. 32 is a plot of acquisition time t_A as a function of derived rate gain $E_T K_D$ for various derived rate time constants τ_D. The

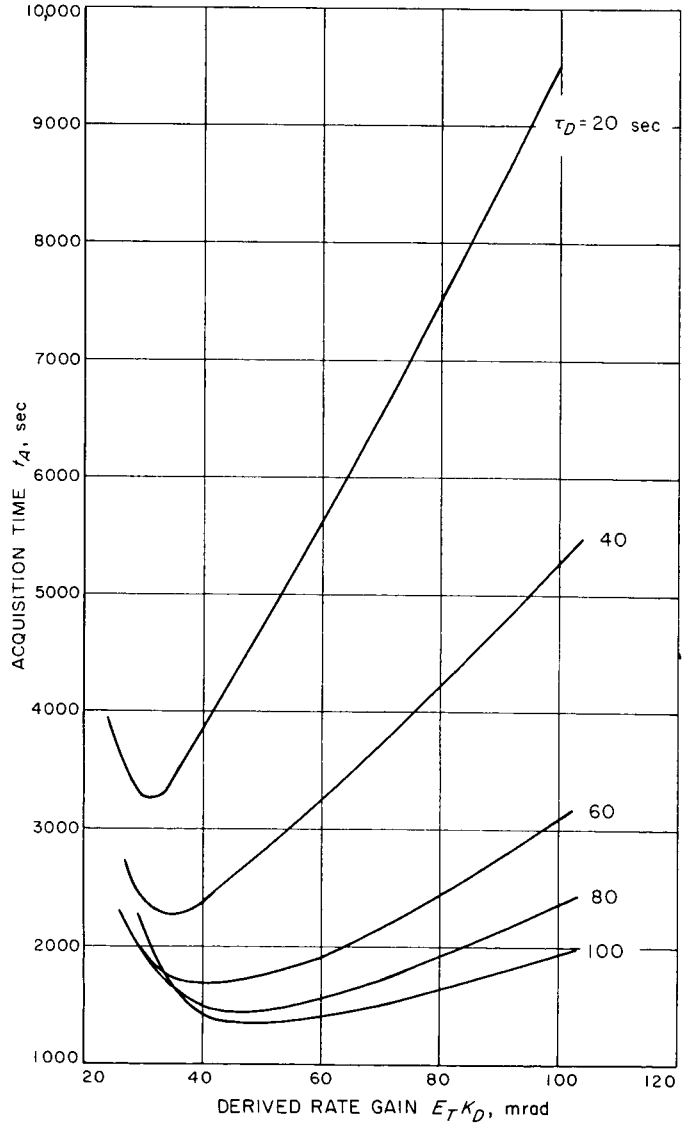

Fig. 32. Acquisition time versus τ_D and E_T K_D derived rate parameters

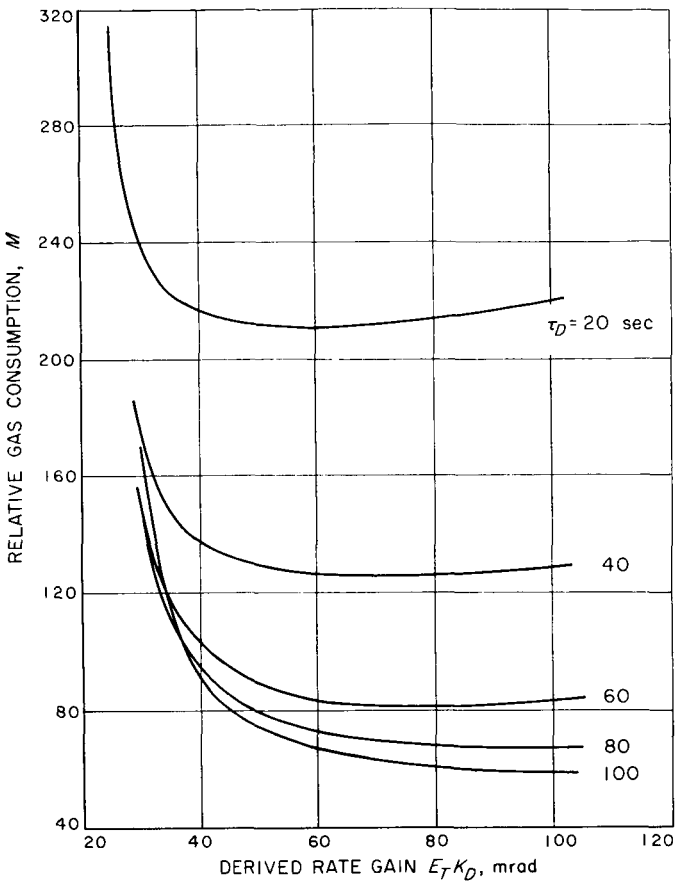

Fig. 33. Gas consumption versus τ_D and $E_T K_D$ derived rate parameters

initial conditions for acquisition are a rate of 3 deg/sec and a position error of π radians. Acquisition is considered complete when the rate is reduced to within ± 0.2 mrad/sec.

The results shown in Fig. 30 may be explained as follows. When the error signal is within the saturation region of the sensor, the derived rate feedback attempts to match the saturated position error signal and turn off the jets. The longer it takes the feedback to catch up with the sensor signal, the longer the jets are on, and the spacecraft accelerates toward or decelerates away from null. The actual net rate reduction takes place in the linear region of the sensor. Therefore, if the spacecraft is allowed to accelerate and decelerate rapidly in the saturated region, it will complete a revolution in a shorter time. This is accomplished by lowering the derived rate gain and increasing the time constant, thereby making it more difficult for the feedback to match the sensor signal. On the other hand, if the derived rate gain is reduced too much, the net rate reduction through the linear region is degraded. Hence, there is an optimum value, which is easily seen on the plots.

It is seen that a large time constant is desirable, but mechanization constraints make it necessary to make the maximum time constant equal to 60 sec. On that basis, it is seen that the optimum derived rate gain is about 40 mrad, and the acquisition time is 1680 sec, or 28 min.

In Fig. 33, relative gas consumption M is plotted as a function of derived rate gain and various time constants. The actual *Mariner C* gas consumption is obtained by multiplying M by 3.1×10^{-4} to give gas weight in pounds. For the optimum acquisition time, the gas weight expended is 0.0032 lb.

The Sun sensor shown in Fig. 31b was used with the optimum parameters of $E_T K_D = 40$ mrad and $\tau_D = 60$ sec, to illustrate the effect of lowering the saturation level. Since this makes it possible for the derived rate feedback to catch up to the sensor signal much faster, as would be expected, the acquisition time was increased to 2140 sec.

Limit cycle operation. Since the derived rate system must also be used for cruise limit operation, it is necessary to investigate the cruise constraints.

There are two conditions to satisfy:

(1) When the jets are fired, the derived rate feedback must be large enough to prevent a noise signal from causing an extra valve pulse. For large derived rate time constants ($\tau_D = 10$ sec) this means that

$$\frac{E_T K_D}{\tau_D} \Delta t > \frac{E_N}{K_S}$$

where

$E_T K_D$ = derived rate gain
τ_D = derived rate time constant
Δt = minimum on time
K_S = Sun sensor scale factor
E_N = zero to peak noise value.

(2) When the jets have fired, the derived rate signal must remain large enough to prevent a noise signal from causing an extra value pulse until the position error signal is reduced enough to prevent it. Therefore,

$$\frac{E_T K_D}{\tau_D{}^2} \Delta t < \dot{\theta}_l$$

where $\dot{\theta}_l$ = limit cycle velocity

For *Mariner C*,

$$E_N = 25 \text{ mv}$$
$$K_S = = 0.687 \text{ v/mrad}$$
$$\dot{\theta}_l = 2 \times 10^{-3} \text{ mrad/sec}$$
$$\Delta t = 20 \text{ msec}$$

It is now seen that the two-limit cycle constraints are

$$E_T K_D > 1.82\, \tau_D \quad (1)$$
$$E_T K_D < 0.2\, \tau_D^2 \quad (2)$$

where $E_T K_D$ is expressed in milliradians and τ_D is expressed in seconds.

It is immediately seen that the optimum acquisition parameters of $E_T K_D = 40$ mrad and $\tau_D = 60$ sec are incompatible with the first requirement. For $\tau_D = 60$ sec, the minimum $E_T K_D$ is 109 mrad. From Fig. 32, the acquisition time is increased to 3400 sec, minimum.

A plot of the allowable gains and time constants, based on the two requirements shown above, is illustrated in Fig. 34.

Multiple axis acquisition. So far the derived rate acquisition studies have all been on a single axis basis. It is necessary to make a three-axis study due to several types of possible crosscoupling between the three axes. These are: (1) inertial crosscoupling, (2) crosscoupling due to gas jet misalignment, and (3) optical crosscoupling through the 4π steradian field of view Sun sensors.

A good analytical solution of the three-axis acquisition involves a major analysis program. The necessity for obtaining preliminary answers in a matter of weeks requires a simplified solution so that there is some possibility of forecasting major problem areas. Along these lines, approximate, simplified studies have been made and some general conclusions drawn.

(1) Inertial crosscoupling and jet misalignment will always degrade the acquisition performance.

(2) Sensor crosscoupling is probably more seriously degrading to acquisition performance than the other two. However, the problem is complicated enough that further study is necessary to understand the effect.

A "quasi" two-axis acquisition (pitch and yaw) simulation was devised to provide more information. In order to describe it, Fig. 35 is used to illustrate the crosscoupling

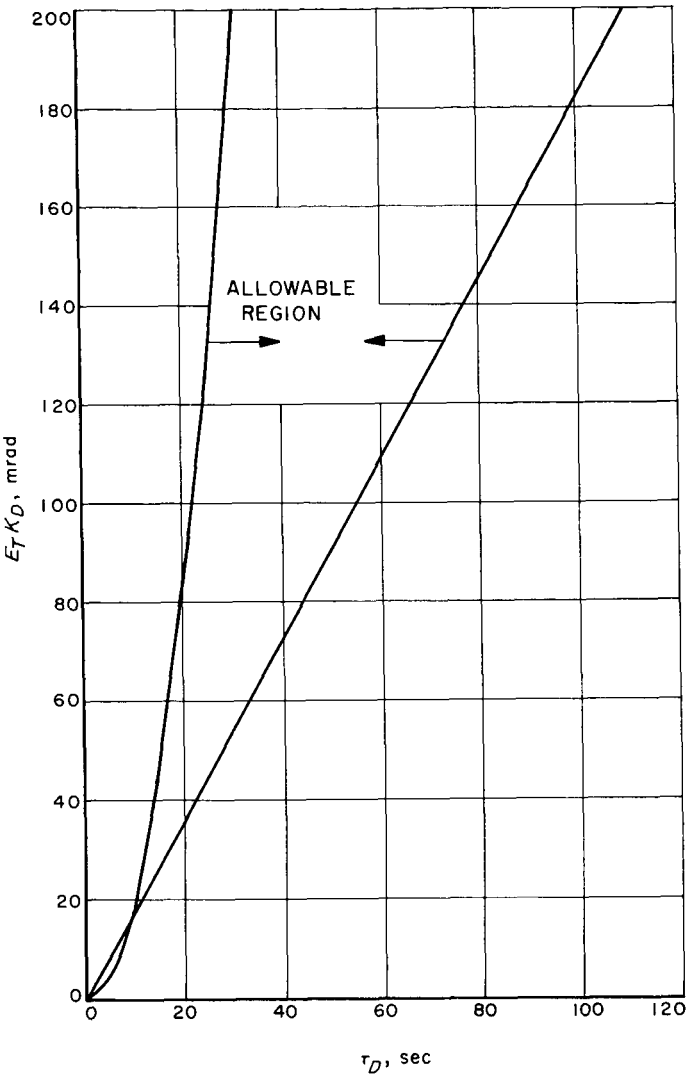

Fig. 34. Derived rate cruise parameter constraints

problem. In this case it is considered that the $+z$ (roll) axis is pointed at the Sun when acquired. Fig. 35 illustrates the case where the roll axis is not pointed at the Sun. The pitch Sun sensor's plane is the y-z plane, and the yaw Sun sensor's plane is the x-z plane. Null for both planes is at z, and there also exists a rear null at $-z$.

It may now be seen that if the roll axis is not pointed at the Sun, any yaw motion of the spacecraft will cause pitch errors to be detected by the pitch Sun sensors. In general, the relationship is

$$\tan \theta_P = \tan \theta_Y \tan \theta_R$$

Moreover, it is seen that if the spacecraft is rolling, the pitch and yaw errors will both change. Obviously, motions about any axis may cause significant inputs to be seen by the other axes.

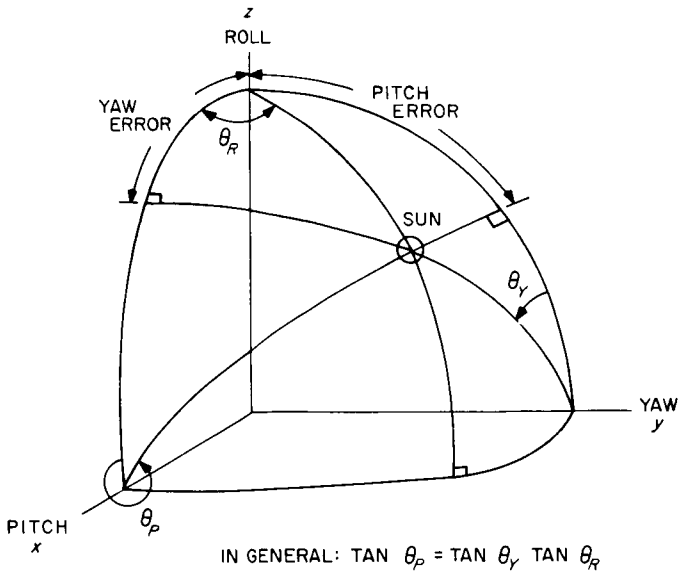

Fig. 35. Off-axis sensor characteristics

A special case is considered. Assume that the pitch and yaw errors are both zero. Then the spacecraft is yawed through 360 deg. For yaw angles between +90 and −90 deg around null, the pitch error is unchanged, that is, it is at null. However, for yaw angles between +90 and −90 deg around the rear (180 deg) yaw null, the pitch plane is turned around so that the rear pitch null sees the Sun and has a 180-deg error. In this case the pitch jets would go on in an attempt to reduce the error to zero. Therefore, even though the pitch axis was acquired, the yaw revolution completely disacquired it.

In addition to the fact that a 180-deg error was put into the pitch axis by yaw motion, the fact that the pitch plane is not parallel to the Sun line causes significant changes in the sensor output. For example, at a yaw error of ±90 deg, the pitch sensor output must be zero since all the pitch sensors are perpendicular to the Sun. Some experimental information has been obtained for off-axis Sun sensor performance. These results are shown in Fig. 36. This plot indicates the attenuation resulting in the sensor output as a function of the off-axis angle of the sensor. The minus values of the attenuation are used to indicate that the rear null is seen by the Sun. The experimental points were for off-axis angles between ±90 deg of the front null, and the minus values of attenuation were assumed to be the same.

In the "quasi" two-axis study, inputs were fed into a single-axis analog simulation to approximate the sensor crosscoupling effect of the other axis. The crosscoupling

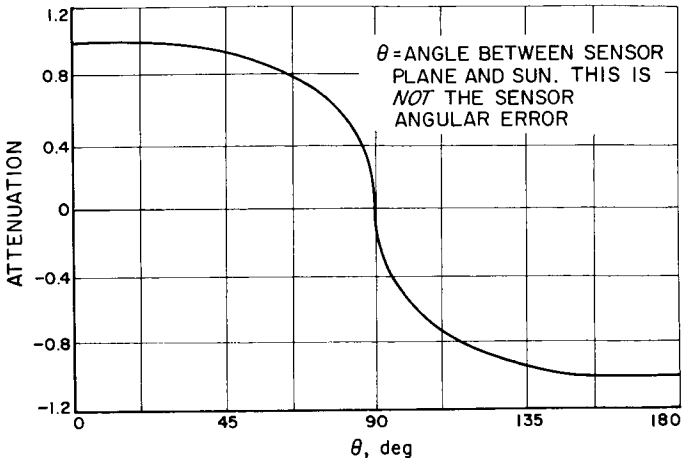

Fig. 36. Sun sensor off-axis attenuation

effect was devised as follows. It was assumed that the yaw angle was the off-axis angle of the pitch plane. A perfect single-axis acquisition, θ_Y as a function of time, was used to represent the yaw angle. This was used to determine the attenuation of the pitch sensor output. Then the pitch sensor output of a single-axis analog study was modified by this off-axis attenuation as a function of time. The result was a pitch acquisition that showed some of the results of sensor crosscoupling.

Results. The derived rate parameters used were

$$E_T K_D = 40 \text{ mrad}$$

$$\tau_D = 60 \text{ sec}$$

The acquisition for a single-axis acquisition was $t_A = 1760$ sec, which was used for the input to the off-axis attenuation program. It was found that the acquisition performance of the crosscoupled axis was a function of the initial conditions. In each case, the initial rate was 3 deg/sec, the maximum allowable separation rate specified. However, initial errors of $-\pi$ rad and 0 rad were used.

For

$$\theta_i = -\pi \text{ rad} \qquad t_A = 1680 \text{ sec}$$

$$\theta_i = 0 \qquad T_A = 2831 \text{ sec}$$

In one case the acquisition was helped; in the other it was hindered. The explanation is as follows. Sometimes the two axes are "in phase," that is, the plus saturation region of the sensor is reducing the rates; then after the error has passed through most of the plus saturation region, the attenuation program multiplies the output with a minus sign. At that point, when the sensor normally passes into the negative saturation region, it looks posi-

tive to the sensor, and the rates are continually reduced. Another effect is that the attenuation of the sensor output as a function of time appears as a proportional output to the switching amplifier and the rates may be reduced or increased depending upon the direction of the change.

In short, it is apparent that the "in phase" or "out of phase" relationships of the two axes can strongly affect acquisition. But in the analysis scheme, since the crosscoupling axis always acquires, it allows the other axis to acquire on a single-axis basis.

Obviously, the crosscoupling axis is also affected by the crosscoupled axis. This effect may be seen by making another iteration. The crosscoupled axis output was used as the input to the attenuation program, and the effect on the output of another single-axis acquisition was recorded. The results showed that during the time the crosscoupling axis was disacquired, it did not allow the crosscoupled axis to acquire. Instead, the rates were even increased up to as much as 4.25 deg/sec. Eventually, the crosscoupled axis acquired, but only when it was allowed to by the acquisition of the crosscoupling axis.

Apparently, the disastrous crosscoupling effect that was observed was due to the fact that the spacecraft must go through several revolutions, even on a single-axis basis, before acquisition takes place. Therefore, another similar simulation was made with an initial rate of only 0.2 deg/sec, and π rad position error. Even in this case enough crosscoupling was observed, such that the affected axis did not begin to acquire until the off-axis angle was reduced to less than 90 deg. In this case, it is more likely that fortuitous initial conditions may allow acquisitions within a 30- to 60-min time period. It would not be recommended to depend upon this.

Conclusions. The type of analysis just discussed was not a worst case study. For example:

(1) The spacecraft is always allowed to acquire since the disturbing input axis is always made to acquire, in spite of the fact that crosscoupling back into the disturbing axis would seriously interfere.

(2) The off-axis angle was considered to be the actual angular error of the disturbing axis. This could be for better or worse.

(3) Disturbing inputs from the roll axis were completely ignored.

(4) Inertial crosscoupling and jet misalignment were ignored, and would further degrade the acquisition.

On this basis, it is concluded that derived rate acquisition on more than one axis at a time is undesirable.

b. Roll acquisition.

The identification and acquisition of Canopus forms the major problem of roll axis attitude control. The acquisition gate provides a logic signal which discriminates against objects that differ markedly from Canopus in brightness. However, false acquisition signals occur over an off-null angular region for a very bright object because the apparent brightness falls within Canopus brightness range. Extremely bright objects may also cause inverted phase error signals. If this is left uncorrected, the resultant roll motion may be a high-velocity limit cycle with very rapid gas consumption.

To avoid the problems presented by very bright objects causing inverted error signals, logic in addition to the acquisition signal is required. The additional logic is based on inhibition of the acquisition signal by a roll error signal polarity detection. The mechanization is relatively simple and reliable if unidirectional roll search is employed. Unidirectional roll search has inherent noise rejection properties, i.e., spurious acquisition signals and very narrow field-of-view objects are automatically rejected. Acquisition of Canopus with unidirectional search requires a $\pm$2-deg minimum field of view for Canopus brightness objects, and this requirement is feasible with the present Canopus tracker.

Roll attitude control system description. A block diagram of the roll attitude control system is shown in Fig. 37. The Canopus tracker provides two signals. The roll error signal e_s is proportional to the roll error angle θ over a range of $|\theta| < |\theta_\ell|$ and is constant for $\theta_\ell \leq |\theta| < \theta_f$. The acquisition signal is a logic signal which indicates when $|\theta| < \theta_f$. When the acquisition signal is true, the relay is in Position 1 and position error information is obtained from the Canopus tracker, i.e., $e_\theta = e_s$. When the acquisition signal is false, the relay selects e_c as the artificial error signal. The voltage e_c causes the vehicle to roll until the next acquisition. A rate-integrating gyro provides a rate measurement signal which sums with e_θ to form the error signal for the switching amplifier and attitude control gas jets.

Phase plane analysis. To facilitate the phase plane analysis, the voltages shown in the block diagram may be related to corresponding position and rate variables. The

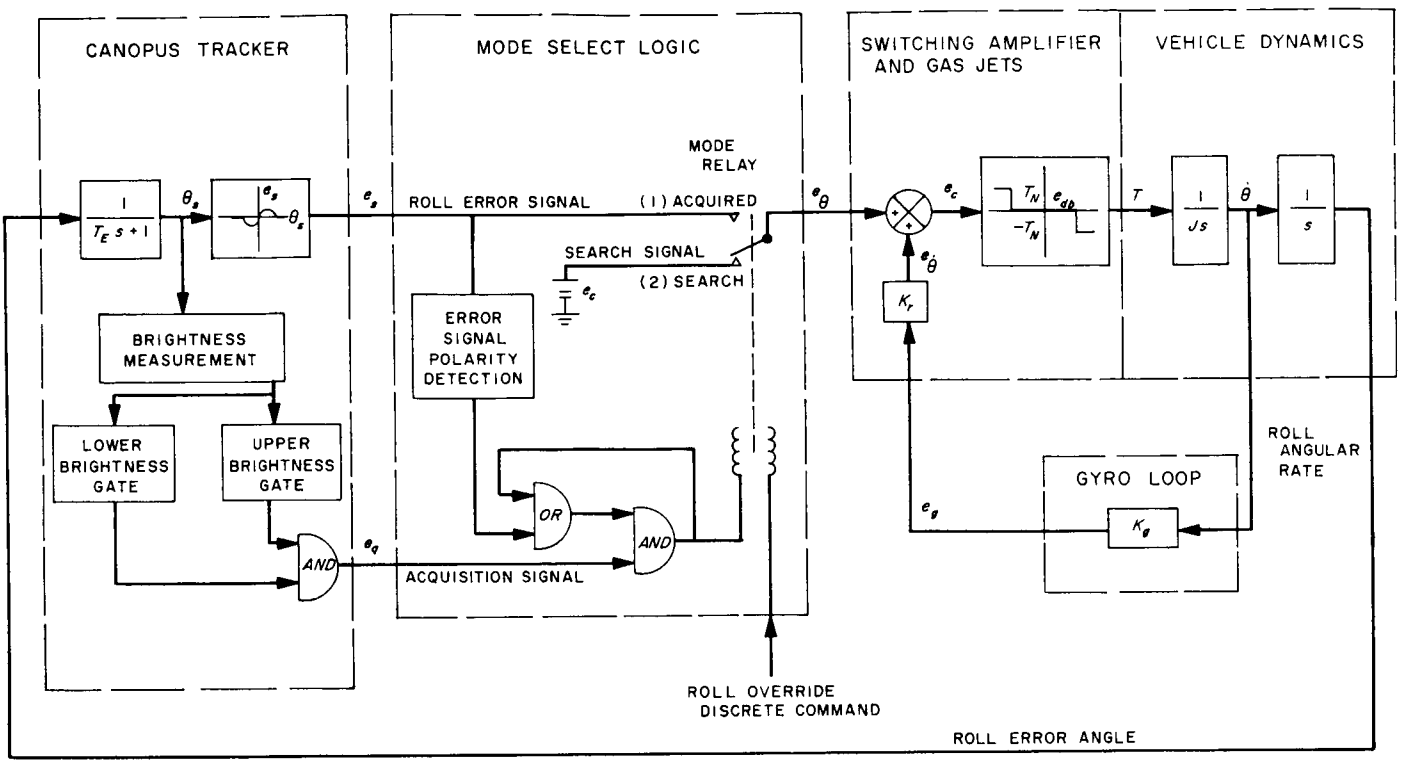

Fig. 37. Roll acquisition block diagram

phase plane switch lines are established by the following relationships:

$$e_s = K_E\theta \text{ for } |\theta| \leq \theta_\ell$$

$$e_s = K_E\theta_\ell \text{ for } |\theta| > \theta_\ell$$

$$e_c = K_E\theta_c$$

$$e_{db} = K_E\,\theta_{db}$$

$$e_g = K_g\,\dot{\theta}$$

Also,

$$\alpha \triangleq \frac{T_N}{J}$$

$$K_{\dot\theta} \triangleq \text{ rate to position gain} = \frac{K_g\,K_r}{K_E}$$

The phase plane switch lines in Fig. 38 illustrate the case when e_c is a constant voltage. This voltage corresponds to a constant position error θ_c. Constant rate switch lines are generated because the position signal sums with a rate signal to actuate the gas jets. Search is unidirectional, always positive, for this case. The nominal search rate $\dot\theta_c$ is $1/K_{\dot\theta}\ \theta_c$. The actual search rate is $\dot\theta_c \pm\theta_{db}\ 1/K_{\dot\theta}$. The acquisition channel time delay T_q causes sloping switch lines at $\pm\theta_f$. The initial conditions for the acquisition phase are $\dot\theta_1 = (\theta_c \pm \theta_{db})/K_{\dot\theta}$ and $\theta_1 = -\theta_f + T_q\,\dot\theta_1$ (switch point S1 in Fig. 38).

The search rate must be scaled so that acquisition is achieved when a worst combination of tracker parameters and half gas system failure occurs. The minimum tracker angles are $\theta_f = 2$ deg and $\theta_\ell = 0.7$ deg. For gas system failure mode $\alpha_f = 0.09$ mrad/sec^2.

The two conditions for acquisition are

$$\frac{1}{K_{\dot\theta}}(\theta_\ell + \theta_{db}) = \dot\theta_\ell < \sqrt{2\alpha_f(\theta_\ell + \theta_f)} \qquad (1)$$

and

$$\frac{1}{K_{\dot\theta}}(\theta_c + \theta_{db}) < \sqrt{4\alpha_f\,\theta_f} \text{ (neglecting } \tau_q) \qquad (2)$$

From (1) the minimum $K_{\dot\theta}$ is determined,

$$K_{\dot\theta} > \frac{\theta_\ell + \theta_{db}}{\sqrt{2\alpha_f(\theta_\ell + \theta_f)}}$$

If $\theta_{db} = 0.25$ deg $\doteq 4$ mrad, $\theta_\ell = 17$ mrad

$$K_{\dot\theta} > 7 \text{ sec}$$

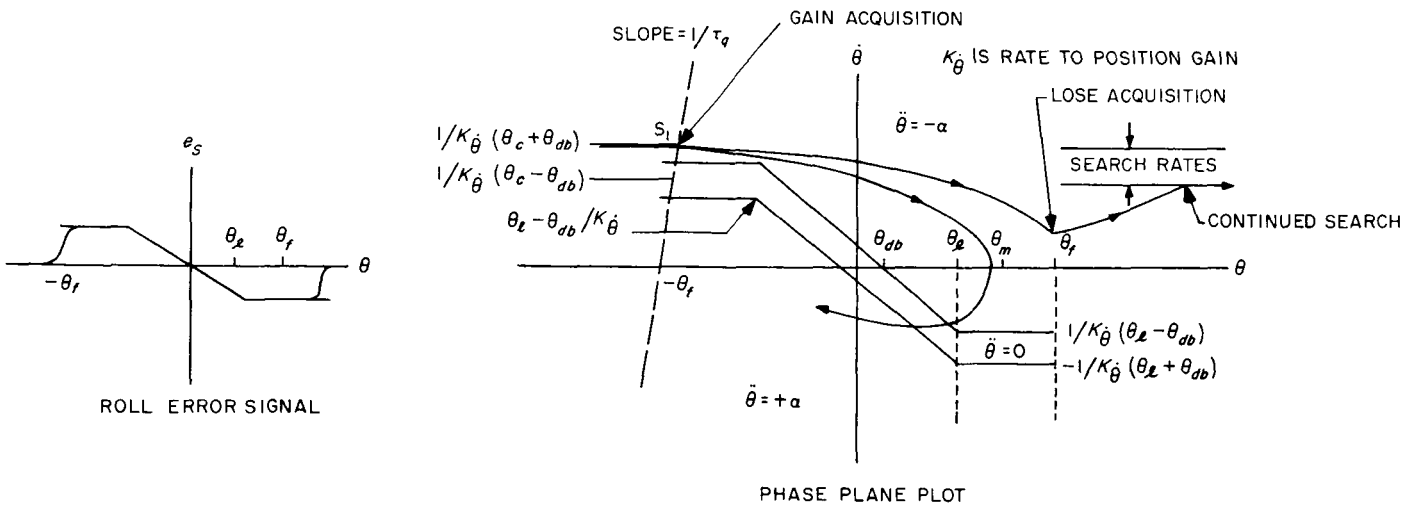

Fig. 38. Canopus acquisition

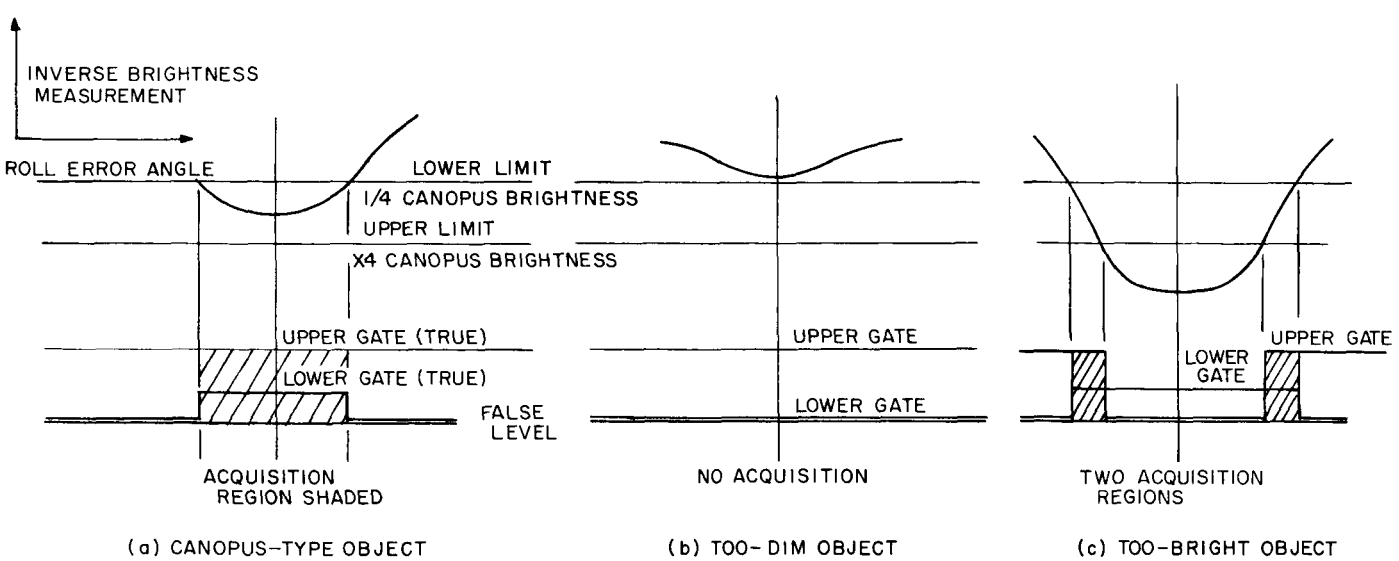

Fig. 39. Acquisition signal

The search rate may be determined from

(2) and $\dot{\theta}_c = \theta_c \frac{1}{K_{\dot{\theta}}}$

$$\dot{\theta}_c < \sqrt{2\alpha_f 2\theta_f} - \theta_{db}/K_{\dot{\theta}}$$

$$\dot{\theta}_c < \sqrt{2 \times 0.09 \times 2 \times 34} - 4/7 = 2.9 \text{ mrad/sec}$$

Now

$$\theta_c = K_{\dot{\theta}}\, \dot{\theta}_c = 20 \text{ mrad}$$

To allow for tolerance buildups, a safety factor of 2 is used so that the nominal search rate is 1.5 mrad/sec or 0.08 deg/sec. After gain of acquisition the roll jets reduce the roll rate to zero at an angle $\theta = \theta_m$ (Fig. 38). The motion continues to spiral inward until limit cycle is achieved.

False objects. The roll control system must have the capability of searching through the entire 2π rad of roll angle, rejecting objects which differ markedly from Canopus brightness. Canopus is identified by comparison of brightness measurements of objects encountered during roll search with Canopus brightness. The acquisition signal consists of the upper and lower brightness gates summed in the tracker and discriminates against objects which are too bright or too dim (Fig. 39). In Fig. 39a

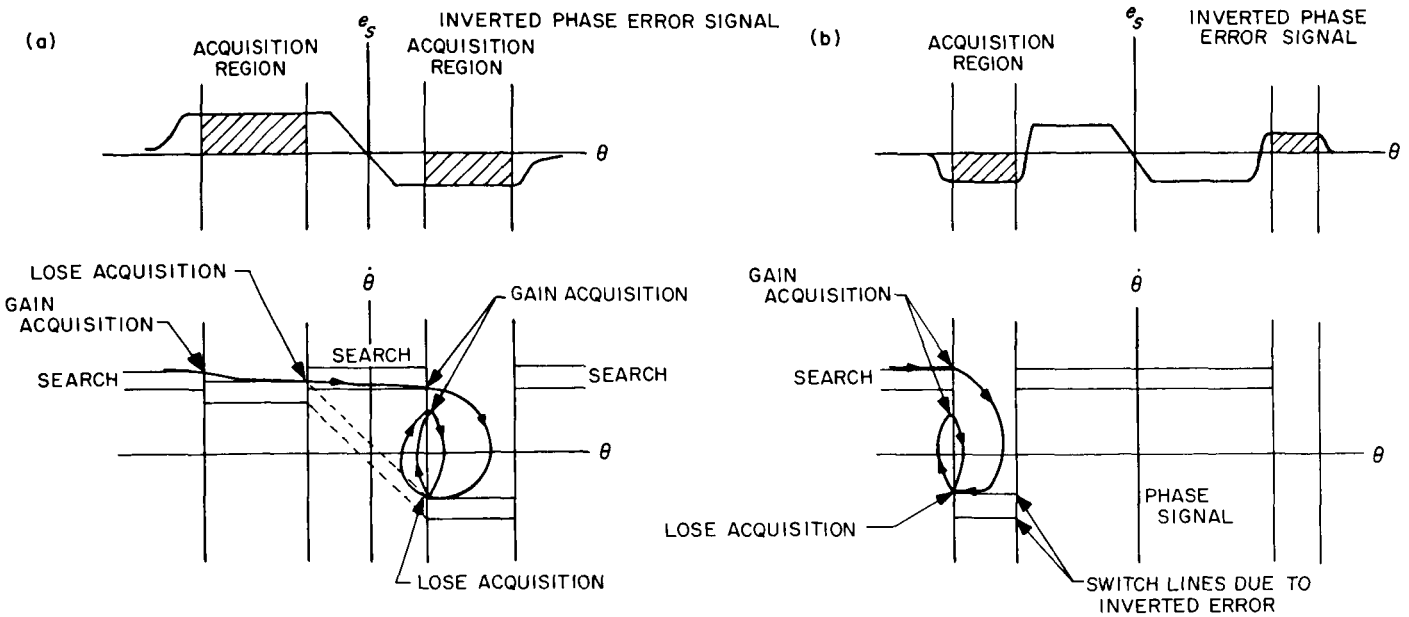

Fig. 40. Behavior without error phase logic for very bright object

both gates and hence the acquisition signal are true in the shaded areas. The false object which is too dim causes no difficulty (Fig. 39b). A false object which is too bright, however, qualifies the lower gate and upper gate in the region in which the apparent brightness is in the Canopus brightness range. Thus a false acquisition signal is present (Fig. 39c). The situation is complicated by the possibility of inverted phase roll error signals in the acquisition region. This phenomenon is due to reflections and arises when extremely bright objects are encountered. The tracker signals for the inverted error signal case are shown in Fig. 40b.

If the inverted error signal region is much smaller than the field of view of Canopus, roll motion will continue until the upper gate goes false. For a wider inverted error signal region the motion will reverse (Fig. 40b) and be driven to the initial acquisition line. Then the system will return to the search mode and the search signal will drive the object back into the field of view causing a limit cycle on the acquisition line. The too-bright, but not inverted, case is illustrated in Fig. 40a.

Similar reasoning predicts a resultant high velocity limit cycle which causes very rapid gas consumption because the jets are on almost continuously.

Mechanization. The mechanization described below and shown in Fig. 37 solves the too-bright object problem, insuring rejection of the too-bright object and continued roll search.

The logic necessary to handle the too-bright object case is rather simple when unidirectional search is used. The mechanization is based on the fact that the roll error signal of Canopus has the same polarity as the search signal at the instant that the acquisition signal changes from false to true. Therefore, a detection of a wrong polarity error signal is used to inhibit the acquisition signal and prevent the change of state from search to acquired mode. Thus the roll control loop will never see the inverted phase error signal and will continue to search. This case is illustrated in Fig. 41b. The case of a too-bright object with proper polarity error signal causes no difficulty because the polarity detection logic will inhibit acquisition in the region where turn around motion might occur. Fig. 41a illustrates this case.

The inhibit circuitry is quite simple, consisting of a transistor, which when saturated by a proper polarity roll error signal, provides the path to be ground through when the mode relay is pulsed from search mode to acquired mode. Once in the acquired mode the transistor is kept saturated by the signal which is present on the other pole of the mode relay. Thus the loss of acquisition will not be inhibited from changing the mode relay state to search.

The unidirectional search mechanization automatically rejects objects whose brightness measurement is close

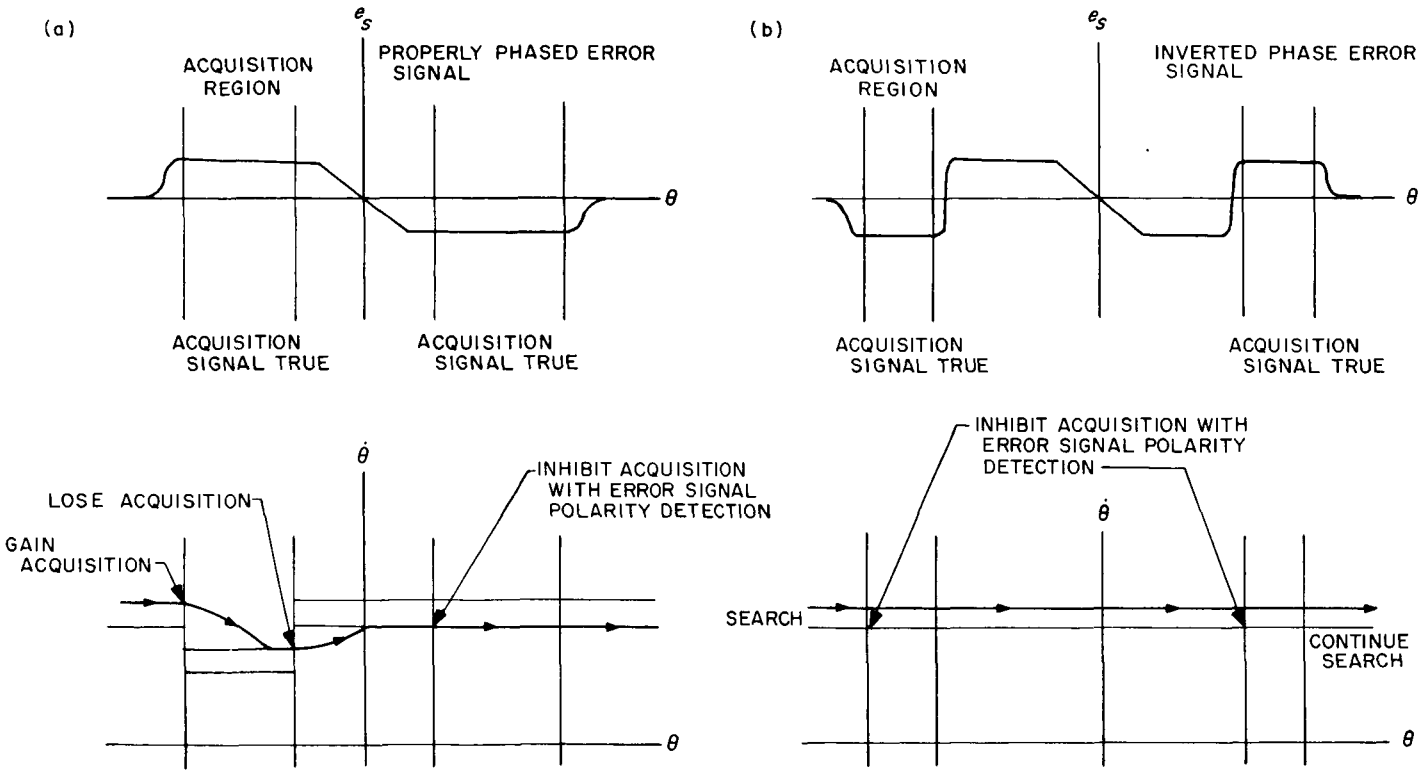

Fig. 41. Behavior with roll error signal polarity detection inhibit logic (very bright object)

enough to Canopus brightness to qualify the lower gate over an angular region much smaller than the Canopus field of view. The deceleration will be insufficient to remove the search rate in the angular region of acquisition and search will resume.

c. Attitude control gas requirements for mission phases.

The amount of attitude control system gas to be stored on the spacecraft is dependent on the gas consumption during initial acquisition, maneuvers, reacquisitions, and cruise. Gas consumption during cruise requires a predication of disturbance torques experienced during cruise. If the solar torque cruise attitude control (solar vane system) functions properly, then unbalanced torque and gas consumption during cruise will be very small. The gas system, however, must be capable of performing the attitude control function without the aid of the solar vanes and despite any failures of the solar vane system which would produce large unbalance torques. The total gas weight stored is sufficient to accommodate solar vane system failures and redundant half gas system failures.

Initial acquisition and reacquisitions. Gas consumption data during initial acquisition is obtained from computer studies of spacecraft dynamic behavior while the large initial tumbling rates are being removed. To date, single axis studies only have been performed. A general three-axis acquisition study, in which crosscoupling between axes is considered, is necessary to determine single-axis performance degradation. Gas consumption during reacquisition after maneuvers and disturbances is much less than during initial acquisition because the spacecraft rates to be removed are much lower than initial spacecraft injection rates.

The computer studies yield gas consumption in the relative units of gas jet on time, which may then be converted to gas weight. The table below shows relative consumption in seconds. Initial tumbling rates are assumed worst case at 3 deg/sec about all axes. Pitch and yaw acquisition is by derived rate while roll acquisition employs gyro rate information.

Mode	*Pitch, sec*	*Yaw, sec*	*Roll, sec*
Initial acquisition	1000	1000	300
Reacquisition	300	300	100

Maneuver mode. The commanded turns require the vehicle to accelerate from near-zero angular velocity to the

commanded turning rate and at the completion of the turn to decelerate to zero velocity. In general, the gain and removal of the turning rates occurs in both the pitch and the roll axes. During the midcourse motor firing, the vehicle attitude is stabilized by the autopilot, but the attitude control gas jets remain on. The approximate relative consumption is computed in Table 4 for turning rate of 3 mrad/sec and engine firing of 30 sec/maneuver.

Table 4. Relative consumption for each maneuver

Mode	Pitch, sec	Yaw, sec	Roll, sec
Commanded turn	24	0	24
Engine firing	30	30	30
Total	54	30	54

Cruise mode. Gas consumption during cruise varies drastically as a function of the type of disturbance present. Various cases will be investigated.

(1) *Undisturbed nominal limit cycle:*

The gas consumption is dependent on the limit cycle dimensions (θ_D, $\dot{\theta}_D$).

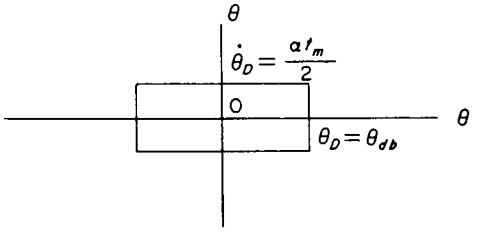

The duty cycle is

$$\frac{t_m}{\frac{2\theta_D}{\dot{\theta}_D}} = \frac{\alpha t_m^2}{4\theta_{db}}$$

The relative gas consumption is

$$t_{ON} = \text{duty cycle} \times \text{mission time}$$

$$t_{ON} = \frac{\alpha t_m^2}{4\theta_{db}} \times t_t$$

For nominal values of $\alpha = \frac{1}{4}$ mrad/sec^2, $t_m = 20$ msec.

$$\theta_{db} = 8 \text{ mrad}, t_t = 200 \text{ days}; \quad t_{on} = 50 \text{ sec}$$

which contrasts with 1000 sec per axis for initial acquisition.

(2) *Steady torque disturbance:*

A steady torque disturbance tends to compress the limit cycle against one side of the dead band.

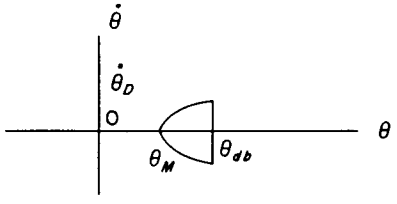

The phase plane plot is shown for T_D = constant > 0

where limit cycle width $\theta_{db} - \theta_M = \frac{\dot{\theta}_D^2}{2T_D/J} = \frac{J\alpha^2 t_m^2}{8T_D}$

The marginal case for this compressed condition occurs when

$$\theta_M = -\theta_{db} \text{ or } T_{DM} = \frac{J\dot{\theta}_D^2}{4\theta_{db}}$$

For *Mariner C* pitch parameters of $J = 60$ slug-ft^2

$$\theta_{db} = 8 \text{ mrad}, \dot{\theta}_D = 2.5 \times 10^{-3} \text{ mrad/sec}$$

$T_{DM} = \frac{1}{6}$ dyne-cm, which is very small.

Gas consumption for constant unbalanced torque is readily computed by considering that over a long time period the average velocity must be nearly zero. Therefore,

$$T_N t_{on} - T_D t_t \doteq 0$$

or

$$t_{on} \doteq \frac{T_D}{T_N} t_t$$

Gas consumption is directly proportional to the magnitude of the unbalance and to mission time, and independent of switching amplifier minimum on time t_M.

(3) *Transient disturbances:*

Transient disturbances with nonzero average value accelerate the spacecraft to angular rates which are higher than nominal limit cycle rates. At the edge of the deadband, these rates will be reduced by multiple pulsing of the gas jets with coasting motion between pulses until turnaround motion is achieved. The average effect of these disturbances will be very small compared to the effect of a steady torque unbalance.

Table 5. Parametric summary

Parameter	Symbol	Units	Pitch	Yaw	Roll
Moment of inertia	J	slug-ft^2	60	60	104
Angular acceleration constant	α	mrad/sec^2	0.225	0.225	0.225
Effective moment arm	ℓ	cm	240	240	225
Gas specific impulse (continuous)	I_S	sec	60	60	60
Gas specific impulse (pulsing)	I_S	sec	35	35	35
Limit cycle deadband	θ_{db}	mrad	8	8	4
Switch amplifier minimum on time	t_m	msec	20	20	20
Total mission time	t_t	days	200	200	200
Gas weight conversion (continuous)	W/t_{on}	lb/sec	3.2×10^{-5}	3.2×10^{-5}	5.5×10^{-5}
Gas weight conversion (pulsing)	W/t_{on}	lb/sec	5.5×10^{-5}	5.5×10^{-5}	9.5×10^{-5}
Unbalance torque conversion	$W/T_{D,avg}$	lb/dyne-cm	4.7×10^{-3}	4.7×10^{-3}	4.7×10^{-3}
Gas weight consumed	W	lb			
Initial acquisition			0.055	0.055	0.017
Maneuvers			0.005	0.004	0.009
Reacquisitions			0.030	0.030	0.011

Noncruise total = 0.215 lb
Leakage per half system = 0.375 lb
Stored weight for zero cruise disturbance = $0.375 + 3 \times 0.215 = 1.0$ lb
The total stored weight is the sum of the zero cruise disturbance number and the stored weight necessary to accommodate the predicted total unbalanced torque. See Fig. 43.

Computation of gas weight. The relative gas consumption is readily converted to gas weight consumed by use of a momentum balance equation.

$$J \alpha t_{on} = W I_S \ell$$

or

$$W = \frac{J\alpha}{I_S \ell} t_{on}$$

The specific impulse of the gas has a different value for continuous jet firing and for pulsed (pulse width less than 0.1 sec) operation. All phases of the mission which employ derived rate increment stabilization fall into the later category.

Table 5 shows the *Mariner C* attitude control system parameters and resultant gas weight conversions.

The important case of unbalanced torque during cruise is discussed here separately. The average rate of gas weight expenditure $\dot{W}$ is obtained from a torque balance.

$$I_s \ell \dot{W} = J\alpha$$

$$\dot{W} = \frac{J\alpha}{I_s \ell} = \frac{T_D}{I_s \ell} \; ; \; \frac{\dot{W}}{T_D} = \frac{1}{I_s \ell}$$

If the average torque unbalance for the entire mission is $T_{D,avg}$, then gas weight consumed is directly proportional to mission time and the unbalanced torque magnitude.

$$\frac{W}{T_{D,avg}} = (\dot{W}/T_D) t_t$$

For $t_t = 200$ days

$$\frac{W}{T_{D,avg}} = 4.7 \times 10^{-3} \text{ lb/dyne-cm}$$

The *Mariner C* gas system is composed of two separate half systems with separate gas-storage bottles so that a valve-open failure will not be catastrophic. The failed open valve will deplete the half system which supplies that valve and in addition will deplete one-third of the gas in the other half system to offset the torque caused by the failed valve. Therefore, three times the estimated gas consumption must be stored in addition to predicted leakage per half system. Fig. 42 illustrates the redundant

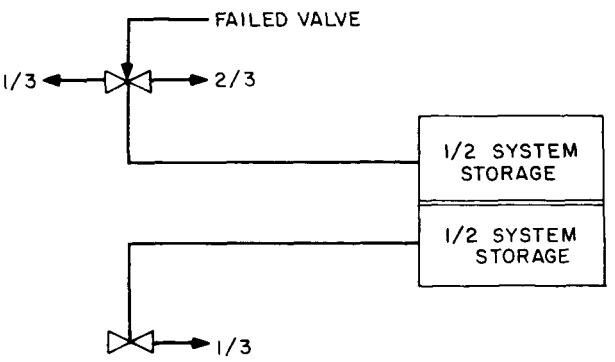

Fig. 42. Redundant mode operation

Table 6. Nomenclature

Symbol	Parameter
J	Moment of inertial about an attitude control axis
α	Angular acceleration constant
ℓ	Effective gas jet moment arm
T_N	Gas system torque about a single axis
T_D	Disturbance torque
I_S	Specific impulse of attitude control gas
θ_{db}	Angular deadband
t_t	Total mission time
t_m	Switching amplifier minimum on time
t_{on}	Relative gas consumption
W	Gas weight consumed
$\dot{W}$	Average gas weight consumption rate
T_{DM}	Marginal limit cycle torque

mode operation. Definition of terms used in this section is given in Table 6.

Unbalanced torques. One of the main sources of unbalanced torques is the failure of a solar vane to erect. The computation of unbalanced torque arising from solar vane failures are shown below:

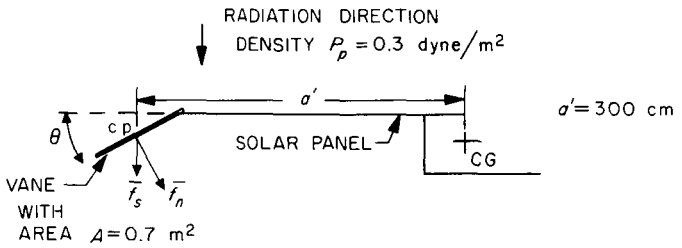

Torque calculations are based on specular reflection with reflectivity $\rho = 0.8$. The force along the Sun line $|\bar{f}_s| = (1 - \rho) P_p A \cos\theta$ and the force normal to vane $|\bar{f}_n| = 2\rho P_p A \cos^2\theta$. The torque of a vane about the spacecraft center of gravity

$$T = |\bar{f}_s| a' + |\bar{f}_n| a' \cos\theta$$

A single vane failure mode occurs when one vane fails to erect, but the opposite vane adapts properly. The unbalanced torque is a single vane torque with

$$\begin{aligned} \theta &= 55 \text{ deg} \\ T_D &= P_p A \left[(1 - \rho) a' \cos\theta + 2\rho a' \cos^3\theta\right] \\ &= 0.3 \times 0.7 \left[0.2 \times 300 \times \cos 35 \text{ deg} + 2 \times 0.8 \times 300 \times \cos^3 55 \text{ deg}\right] \\ &= 26 \text{ dyne-cm} \end{aligned}$$

The worst case occurs when one vane fails to erect and the opposite vane fails to adapt. Unbalanced torque is a single vane torque with

$$\begin{aligned} \theta &= 35 \text{ deg} \\ T_D &= 0.3 \times 0.7 \left[0.2 \times 300 \times \cos 35 \text{ deg} + 2 \times 0.8 \times 300 \times \cos^3 35 \text{ deg}\right] \\ &= 66 \text{ dyne-cm} \end{aligned}$$

Table 7 summarizes the cases likely to be encountered.

d. Canopus tracker.

System design. The *Mariner C* Canopus tracker has two basic functions. The first is to provide roll error signals on Canopus during the cruise mode. Canopus must be acquired for pointing the high-gain antenna back

Table 7. Gas weights for 200-day mission

Mode description	Total average unbalanced torque about all axes, dyne-cm	Cruise mode gas weight expended due to unbalanced torque, lb	Total stored gas weight necessary to accommodate the mode (Includes non-cruise consumption, lb
All unbalanced torque removed	0	0	1.0
Mariner 2 unbalanced torque	73	0.34	$3 \times 0.34 + 1 = 2.1$
Expected unbalanced and single axis failure	$73 + 26 = 99$	0.43	$3 \times 0.43 + 1 = 2.3$
Expected unbalanced and double solar vane failure	$73 + 66 = 139$	0.65	$3 \times 0.65 + 1 = 2.95$

Due to the uncertainties involved in the assumptions used in this analysis, a safety factor of 3 is recommended. Recommended gas weight is $3 \times 2.3 = 6.9$.

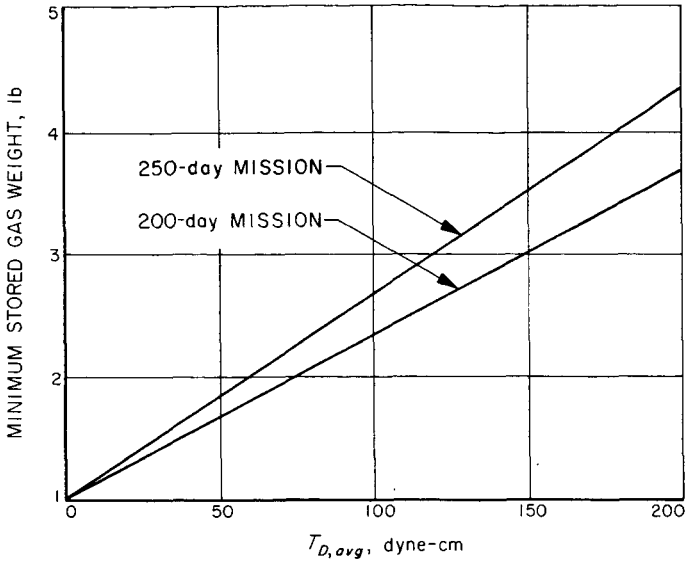

Fig. 43. Minimum stored gas weight as a function of total unbalanced torque

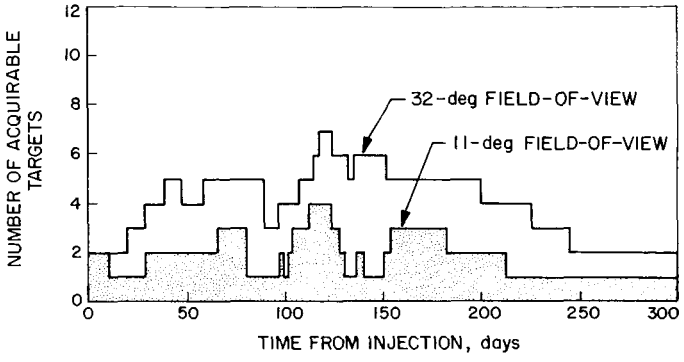

Fig. 44. Star tracker acquirable targets for the Mars mission

to Earth. The second function is to provide a celestial reference upon which to base the midcourse maneuver.

The most difficult problems involved in building the Canopus tracker system are the problems of acquisition and recognition. The problem of acquisition is intimately involved with the whole roll attitude control system. It is appropriate to discuss the characteristics of the Canopus tracker and trajectory geometry which create the problem.

The parameters used for recognition of Canopus are its position and illuminance. Confidence in tracker calibration and in the absolute value of the illuminance of Canopus is not high. Unless we can achieve more confidence in these parameters we will be forced to set our lower gate at 1/4 Canopus. This includes at least 20 stars, the Moon, and the planets Earth, Jupiter, and Mars. The Earth and Moon can be rejected early in the mission with a high gate. Mars can be rejected the same way near encounter.

The position of Canopus is described by its cone angle from the Sun and its clock angle about the probe-Sun line (which is defined as zero with the clock angle of all other objects measured from Canopus). The field of view of the tracker is limited in cone angle to approximately 11 deg. Therefore, as the spacecraft rolls about the Sun line many stars are excluded as possible targets for acquisition. The 11-deg field of view is gimbaled electronically to follow Canopus through a total excursion of 28 deg in cone angle. Decreasing the field of view decreases the length of time a given star has the proper cone angle. Fig. 44 is a bar graph comparing the number of acquirable targets other than Canopus as a function of time for a 32-deg field of view with the 11-deg one used.

The 11-deg field-of-view plot in Fig. 44 serves to illustrate that automatic acquisition and recognition will not be achieved by the Canopus tracker. The star Achernar (illuminance = 0.43 × Canopus, clock angle 40 deg) is the one object preventing automatic initial acquisition. Achernar has been accepted as a target which cannot be discriminated against without compromising reliability and unduly increasing complexity. A clockwise roll search will be used to make the probability of acquiring Achernar before Canopus equal to approximately 0.1. Two telemetry channels will be prime factors in deciding what target has been acquired. First will be the star brightness readout which will be calibrated to our laboratory standard. As the spacecraft searches for an acquirable target, the brightness of objects in the field of view will be recorded on the ground approximately every 1.2 deg. From this a star map can be made which will be extremely useful in deciding what target has been acquired even if the absolute brightness calibration is not perfect. The second is a channel which monitors the output of a photoconductive Earth gate. The field of view is such that the Earth will be detected only if Canopus is the target acquired by the tracker. Once a target has been acquired, recognition will be a ground-based decision.

Roll acquisition is complicated by tracker response to very bright objects (the Earth illuminance $> 10^6 \times$ Canopus) just outside the field of view. Optical ghosts and light diffusely reflected off the baffles cause a Canopus level acquisition signal but also a saturated error signal of the wrong phase to be generated by the tracker. This transition period of operation occurs when the planet is

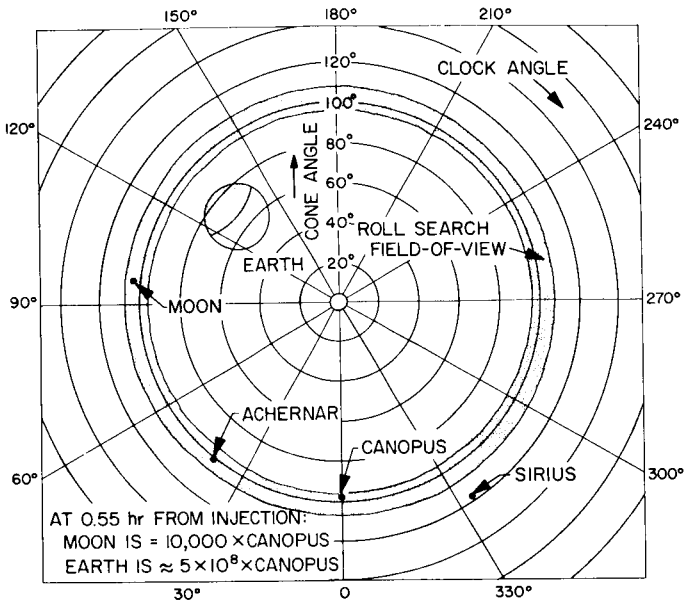

Fig. 45. Type I trajectory mission

between 7 and 15 deg off axis. For all straight-forward acquisition schemes the spacecraft would limit cycle on a bright object.

The Earth and Moon are the bright objects which create this problem. The Moon has 10^5 times the illuminance of Canopus at the time of initial acquisition. For many launch days the Moon will also have the proper cone angle. On a typical trajectory the Earth has a cone angle that will cause trouble for the first week. Fig. 45 shows the trajectory geometry at the time of acquisition. The position of the Earth is rapidly going toward the critical cone angle and has an illuminance which is greater than 10^6 Canopus.

Considerable effort was expended on this problem. It finally was solved rather simply by using a unidirectional search and discriminating against acquisition signals which occur when the error signal has the wrong polarity.

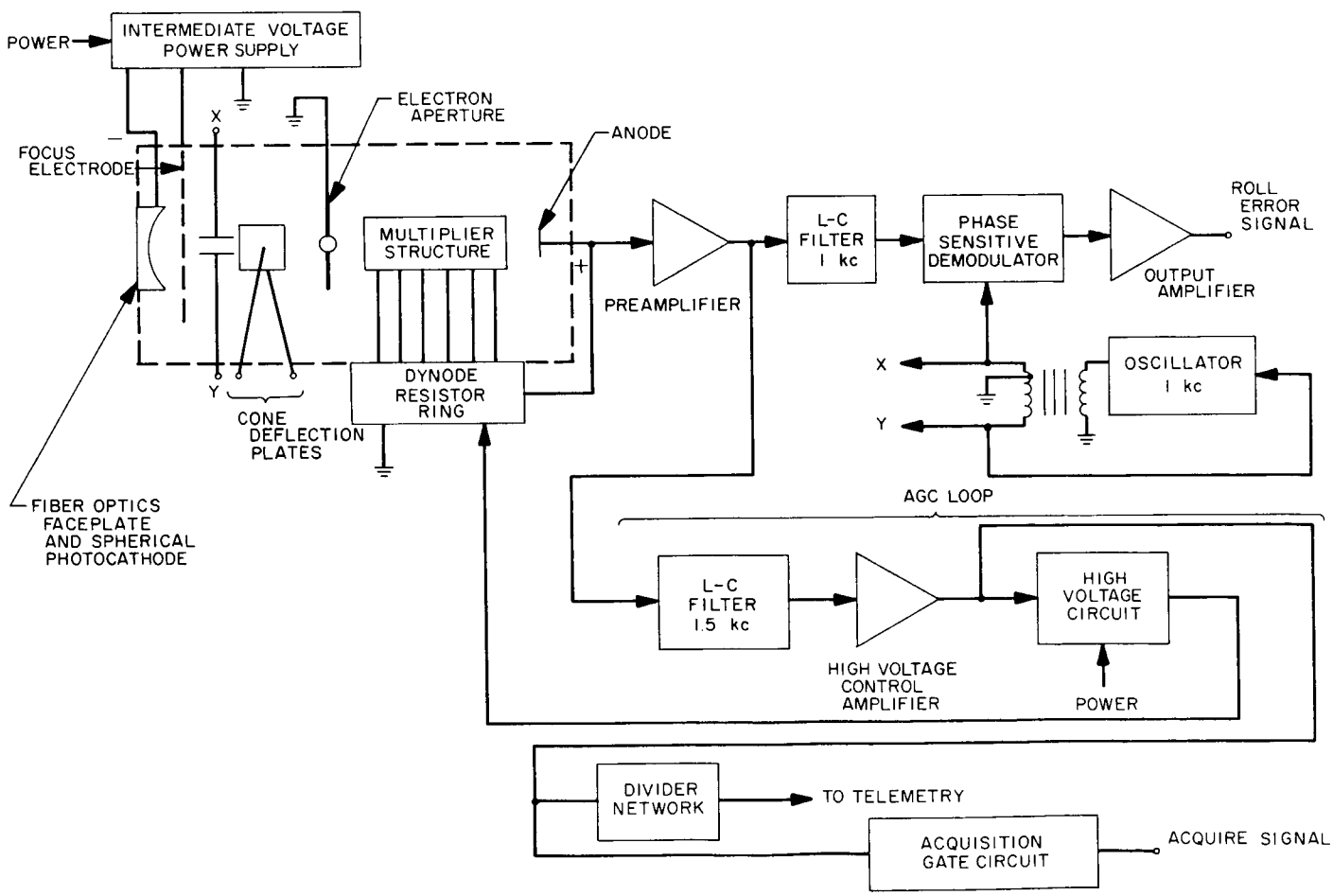

Fig. 46. Image dissector and roll electronics

Electronic mechanization. The Canopus tracker requirements are:

Linear field of view in roll	±0.85 deg ±0.15 deg
Total field of view in roll	±2 deg (minimum)
Scale factor	8 v dc/deg ±20%
Noise peaks	0.2 mrad peak-to-peak
Acquire gate	Canopus + 4 × Canopus − ¼ × Canopus
Roll error time constant	0.5 sec
Acquisition gate time constant	0.5 sec

The electronic circuitry of the Canopus star tracker has been designed to take full advantage of the unique characteristics of the image dissector tube. The image dissector tube (Fig. 46) consists of a spherical S-11 photocathode surface followed by an electrostatic focusing electrode and a set of spherical electron optics orthogonal deflection plates and a precision aperture. The deflection system is in a vacuum envelope with a conventional electron multiplier section. A fiber optics faceplate transfers the image from the optical system's image plane to the curved photocathode surface. The electrons emitted from the photocathode are imaged in the plane of the aperture. The image of electrons is swept sinusoidally at 1 kc across the aperture. The width of the aperture is such that electrons are collected up to approximately 40% of the time. Fig. 47 shows the pulse trains generated for various star positions. (Note the phase of 1-kc component with respect to sweep.) A Fourier analysis of the pulse train shows that the 1-kc component is proportional to the roll error. Fig. 48 shows the behavior of the 1-kc and 2-kc component with star position.

The magnitude of the generated pulses is proportional to the brightness of the object in the field of view. The roll error signal is generated from the phase and magnitude of the 1-kc component, and the AGC loop is controlled by the magnitude of both the 1-kc and 2-kc components.

The output current pulses of the tube are amplified by a transistorized, high-gain, wide bandwidth, three-stage preamplifier. The 1-kc component is filtered by a high Q, narrow bandwidth, temperature stabilized L-C filter. This

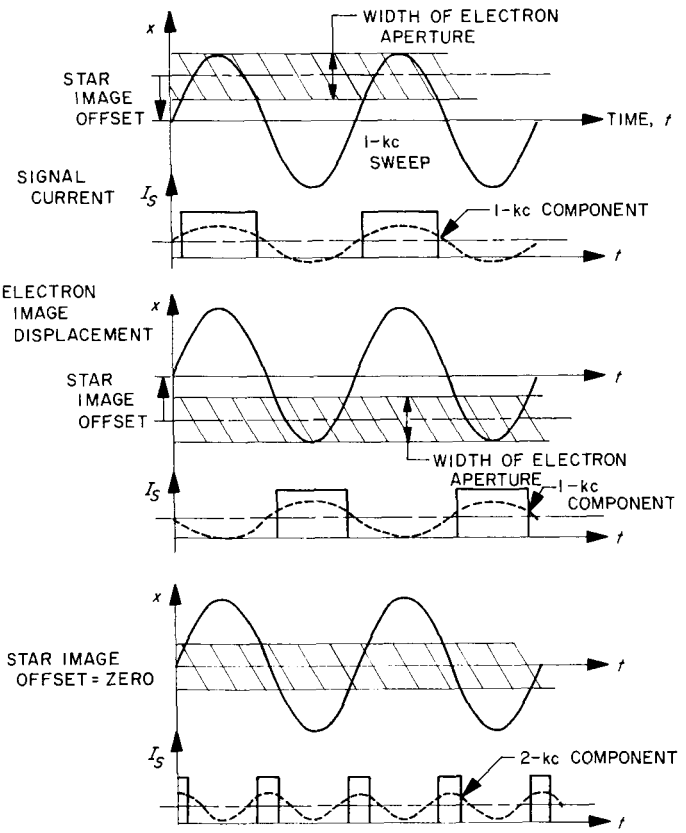

Fig. 47. Pulse trains generated for various star positions

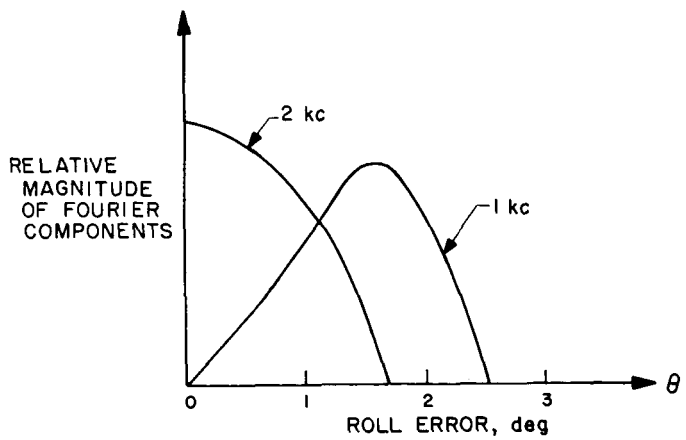

Fig. 48. 1-kc and 2-kc component magnitudes versus roll error of the star

signal is demodulated in a half-wave diode demodulator, and the resultant signal is amplified and filtered by a two transistor DC amplifier.

The AGC loop performs several functions. It varies the gain of the tube's multiplier section, as the gain varies

exponentially with the applied dynode voltage. This lengthens tube life by preventing excessive current flow when a bright object is encountered. This feature also compensates the system against unpredictable long term changes in the multiplier gain. The stability of the magnitude of the preamplifier output pulse permits the use of a very simple and reliable demodulator in the roll loop with no performance degradation. The AGC loop also provides a signal that is proportional to the brightness of the object in the field of view which is telemetered as a check of tracker operation and also to control the "acquire" logic gate.

The AGC loop consists of a controlled bandwidth L-C filter with a center frequency of 1.5 kc. The bandwidth of the filter is approximately ±600 cps in order to pass both the 1-kc and 2-kc signals and to discriminate against tube noise outside this bandwidth. The resultant signal is peak detected and DC amplified in the high voltage control amplifier. The high voltage circuit is a 2400-cps resonant tuned circuit driving a half-wave voltage quadrupler. The magnitude of the output voltage is controlled by changing the Q of the resonant circuit indicator with the DC signal from the control amplifier through an auxiliary bias winding.

The acquisition gate is turned on only when an object in the brightness range of the star Canopus is in the field of view. The gate consists of two modified Schmitt trigger circuits in cascade.

The roll reference frequency oscillator is a conventional stabilized L-C tuned circuit oscillator with an AGC loop for amplitude stability.

The intermediate voltage power supply for the cathode and focus voltages is similar in design to the high voltage circuit except no regulator circuitry is required as these voltage magnitudes are not critical.

The low voltage power supplies are full wave bridges with resistor-capacitor filters, transformer coupled to the 2400-cps power bus. No regulation is required, as all the tracker circuitry will operate properly for wide variations in the supply voltage.

The required field of view in the other axis, the cone axis, is much greater than the roll axis to perform the required mission. The aperture is restricted to an 11-deg field of view in order to reduce background effects, and the required dynamic range of 30 deg is supplied by an electronic gimbaling method. The cone deflection plates

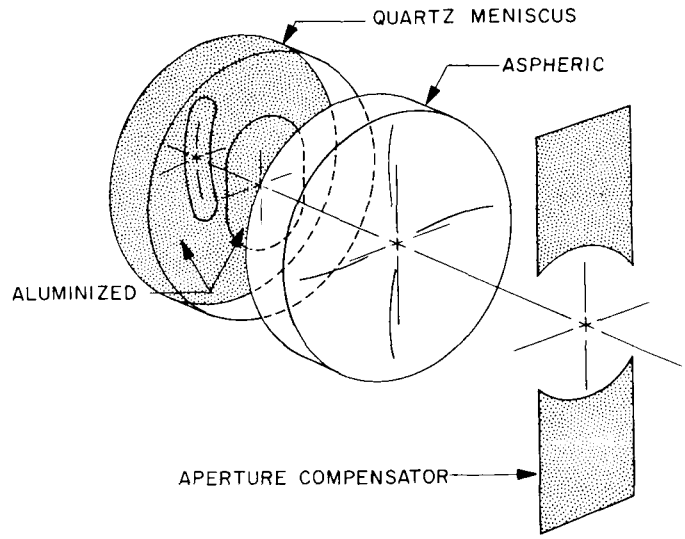

Fig. 49. Canopus tracker optical system

are driven by incremental voltages from an 8-bit magnetic latching relay ring counter. The cone angle generator is switched by either fixed timing signals from the CC&S or by overriding radio commands. Five positions, each a progressive increment of 5 deg, are used during the mission. The three remaining steps are redundant positions corresponding to the planet encounter cone angle.

The tracker is equipped with a mechanical Sun shutter that automatically shields the photocathode from the physically damaging effects of imaging extremely bright objects. The power for the shutter is switched on by a logic network in the attitude control system whenever the spacecraft is not positioned along the Sun line. The actual closing signal is provided by an auxiliary cadmium sulfide detector and an internal drive amplifier.

Optical design. The optical system of the tracker consists of a shade, a catodioptric lens, and an aperture compensator (Fig. 49).

The shade is designed to give the tracker a field of view which is 4×30 deg. It also prevents stray light originating outside a cone which is 70×50 deg from falling on the lens. Baffles in the shade are arranged so that a minimum of first reflection stray light will enter the lens (Fig. 50).

The lens is designed to have a uniform image quality in a field of view which is 4×40 deg. It has a 0.8-in. focal length and a geometric "speed" of $f/0.6$. However,

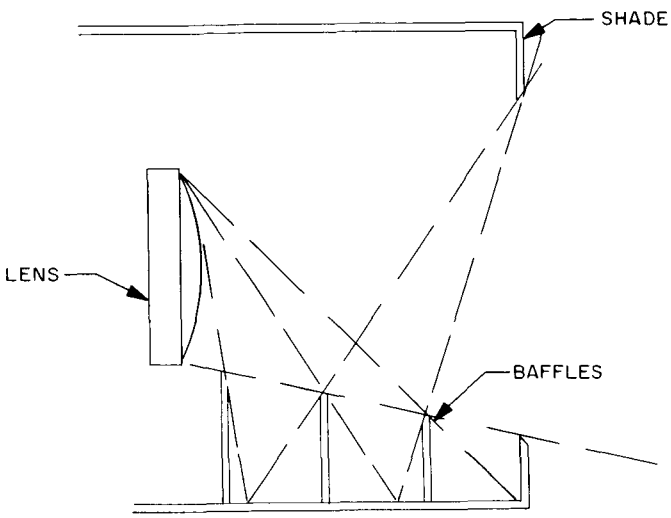

Fig. 50. Internal baffling layout for the Canopus tracker

the effective speed considering the aperture compensator is $f/1.0$.

The aperture compensator is used to make the image intensity constant with cone angle. This is necessary to eliminate variation in the signal as a function of star cone angle. A 34% fall-off in the signal would be expected without the aperture compensator. No detectable signal change is noted that can be attributed to aperture modulation in the ± 15-deg field of view, and no undesirable side effects have been found.

Mechanical design. The mechanical design of the package was complicated by the required mounting geometry. The package is essentially cantilevered from the front ⅓, which is essentially the shade. To cope with this condition it was found desirable to package electronics well toward the front of the shade to help balance the tracker.

The tracker is integrated into a single unit. It houses the shade, the optics, the image dissector, and all the electronics. The image dissector is mounted in O-rings and constrained axially by a clamp at the front. This prevents changes in the optical focus with temperature and prevents stressing the image dissector. The optics are mounted in a barrel which is flange mounted to the chassis of the tracker. Focusing is accomplished by shimming. Alignment of the optical axis with the electrical null of the image dissector is accomplished by having ample tolerance in the clearance holes on the flange. The baffles and aperture compensator drop in as a unit. The baffle assembly is fabricated of 0.020 stock and is very light weight. The tracker is enclosed by 4 cover plates. Three of the covers serve only as dust covers. The fourth is used to seal out light from the optics and image dissector and to give the structure torsional rigidity.

The one area which remains as a problem in the mechanical design is the Sun shutter. Two designs are under evaluation. One is an external Sun shutter which is a flag operated by a rotary solenoid. The other is an internal shutter which acts just in front of the image plane. The design under evaluation has no sliding or rotating parts and the potential of excellent reliability.

The packaging of the electronic circuitry takes advantage of the mechanical configuration of the tracker. The conventional single-sided printed circuit boards are arranged around the three sides of the image dissector tube and are completely accessible and functional if the protective covers are removed. Only one connector is used in the tracker, at the spacecraft interface. All of the 2400-cps primary power is utilized on the connector side of the tracker. All component parts are derated in accordance with *Mariner C* requirements.

Breadboard and prototype trackers have been in operation for several weeks exceeding all the functional requirements and without any operational failures. An environmental prototype is in construction, and the full range of environmental tests will be conducted with this model.

e. Square root Sun sensor.

This Sun sensor was developed to allow Sun acquisition without the use of pitch and yaw gyros. The name "square root sensor" was used because the original requirement specified an output which was proportional to the square root of the angle from the null position for both the pitch and yaw axes. This requirement has since been changed to provide a greater scale factor near null and saturation of the signal near 100 deg. A modified output curve of the Sun sensor system is shown by Fig. 51.

Four nearly identical assemblies, each containing four Clairex 605 photodetectors, are required for the square root Sun sensor system. Two primary assemblies are mounted on the sunlight side of the spacecraft bus and contain four photocells which serve the same function as the primary cells on *Mariner R*. The remaining four cells (two per assembly) and all eight cells of the secondary assemblies serve the same function as the secondary cells on *Mariner R*. The secondary assemblies are mounted on the dark side of the spacecraft bus. Two different excitation voltages are supplied to the primary assemblies,

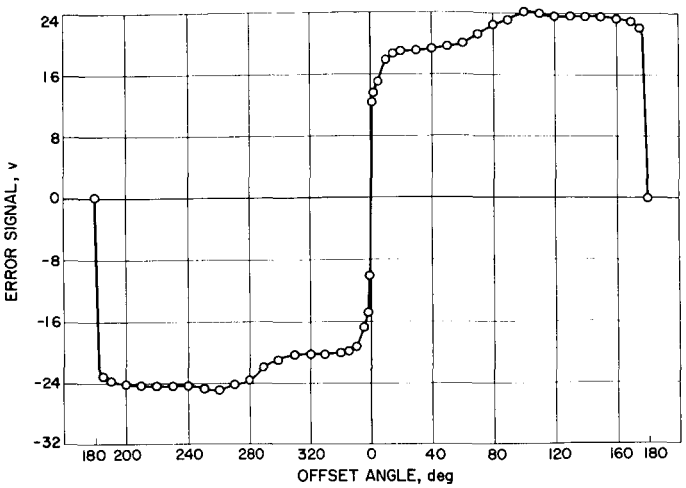

Fig. 51. Square root Sun sensor system characteristics

±16 v to the primary cells and ±26 v to secondary cells. Since the secondary assemblies contain only secondary cells, only the ±26-v excitation is required.

This system does not require any photocells to be mounted on the solar panels. In order to accomplish this, each of the four cells which would normally look out along the plane of the solar panels was replaced with two cells connected in parallel. One of these cells is located in a primary assembly, and its field of view is restricted to 1-π steradian cutting off at the plane of the solar panels. The other cell is located in a secondary assembly and covers 1-π steradian on the other side of the solar panel plane. Together they cover a 2-π steradian field of view but cannot be affected by reflections or shadows from the solar panels.

f. Reset Sun sensor.

The reset Sun sensor is required to indicate when the spacecraft is 180 deg from Sun acquisition about the x and/or y axis. This output is used in the attitude control logic to reduce gas consumption and the time required for acquisition. This is done by controlling the gas jets so that the spacecraft's angular rate is reduced as it approaches the Sun-acquired position from 180 deg out.

The sensor is built around two Clariex 605 photocells connected in parallel. One elongated aperture serves both cells, providing a total field of view of 20 × 180 deg. The assemblies are mounted on the dark side of the spacecraft bus. Two assemblies are oriented to sense the Sun position about the x axis and two more are used for the y axis. In this way, redundant outputs in both axes are provided to the attitude control system logic.

g. Sun gate.

The Sun gate used on *Mariner C* is a modified version of the one used on *Mariner R*. For *Mariner C* each of the two detectors is masked and shadowed so that it has a uniform response curve to cone angle offsets and is insensitive to clock angle changes. One assembly therefore provides two independent outputs instead of one as in *Mariner R*. The redundant output is used to improve the reliability of the attitude control system.

The output signal is used to terminate the Sun acquisition mode whenever the spacecraft roll axis is within a predetermined angle of the Sun line. The excitation voltage to the secondary Sun sensor's cells is removed upon acquisition. This prevents degradation of null characteristics generated by the primary cells.

h. Earth detector.

The Earth detector is used to verify the acquisition of Canopus after the roll search is completed. If Sun and Canopus acquisition are accomplished, the Earth detector will sense reflected sunlight from the Earth. Its field of view is ±25 deg in cone and ±17 deg in clock, which will cover the change in direction from the spacecraft to Earth due to differences in individual trajectories.

The construction of the Earth detector is very simple. It consists of a one-element lens which images the Earth on a cadmium sulphide photocell. The detector strip is in the form of a grid pattern which is large enough to receive the Earth image as the Earth angle changes within the field of view. A DC voltage is applied to one side of the detector so that current will pass through the photocell and a fixed resistor to ground. The voltage across the fixed resistor changes in relation to the light received by the photocell. This voltage is telemetered and indicates the apparent Earth flux when the Earth is within its field of view.

i. Gyro control assembly.

The purpose of the gyro control assembly is to provide inertial rate and position information to the spacecraft attitude control system for use in acquisition damping or for steering the spacecraft during the midcourse maneuver.

The gyro control assembly has three basic modes of operation. The first is a straightforward rate mode wherein the amount of capture current applied to the gyro torquer is directly proportional to the angular rate about the gyro input axis. This mode is used to damp the spacecraft motions during acquisition of the Sun or reference star.

The second mode is the commanded turn mode. During this mode of operation, the spacecraft is caused to turn about the pitch or roll axes by applying torquing currents to the respective gyros upon command from the CC&S or the radio command decoder. The gyro feedback loop is modified so as to insert a large storage capacitor in the torquer loop. This capacitor stores the total angular movement about the gyro input axis, while at the same time, the gyro is still providing rate information. Turning action is provided by applying a precision torquing current to the gyro torquer. The error signal produced by the gyro gimbal motion is applied to the attitude control system switching amplifier causing the spacecraft to follow the gyro gimbal.

The third mode of operation is the rate plus position mode. The gyro rebalance loop is the same as the commanded turn mode with the exception that no precision torquing current is applied. Thus the capacitor and gyro store the signal on the integrating capacitor. This mode is used during the time that one spacecraft axis is turning while the other two are holding an inertial lock. The same mode is held in all three axes during midcourse rocket motor burning. Error signals from this circuit are used as steering commands to the rocket motor jet vane actuators through the autopilot, and serve to keep the spacecraft on course.

The gyroscope selected for use in this assembly is a miniature, floated, rate-integrating type. It is an inertial guidance quality instrument manufactured by Kearfott Incorporation, New Jersey. This gyro is one of a family of similar Kearfott gyros known as the "Alpha Series" and is designated as Model 2565. The original version of this gyro was designed as a platform stabilizing gyro and was intended to operate at a constant 180°F. Due to the fact that no power is available on the spacecraft to heat the gyro to this temperature, a much lighter flotation fluid is used in the *Mariner C* (2565) version. This less viscous fluid permits operation over a range of ±20°F from 115°F which is the temperature the gyro assumes due to heat from the spin motor.

The rebalance amplifier for this gyro is shown in Fig. 52. AC error signals at 2400 cycles from the gyro pickoff are first amplified by the AC section consisting of Q1, Q2, and A3. This AC section is stabilized by large amounts of AC and DC feedback which hold the gain and DC levels constant over a wide range of temperatures, supply voltages, or different transistor gains. The amplified AC

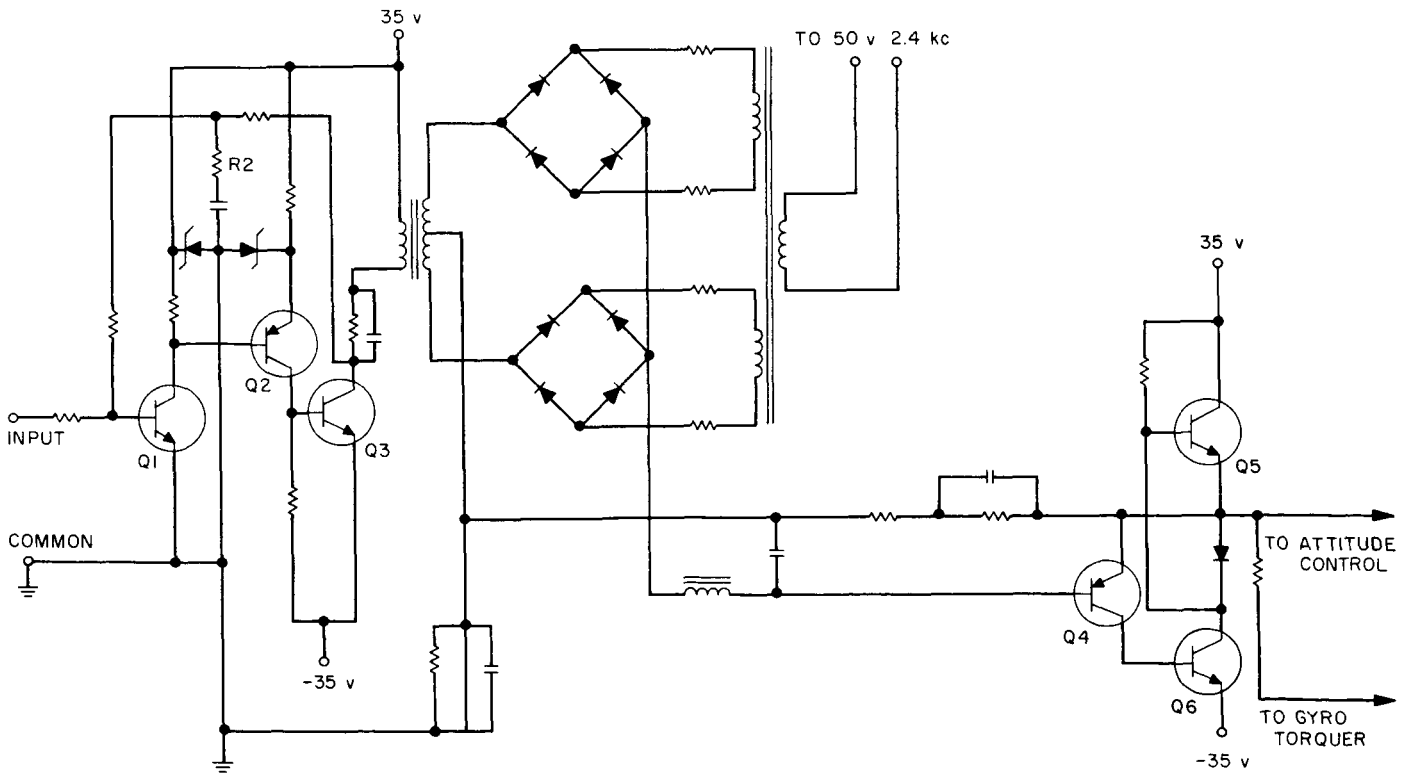

Fig. 52. Gyro loop closing amplifier

error signal is transformer-coupled to a double ring demodulator. DC from the demodulator is fed through a compensation network to a DC power amplifier. The compensation network is required due to the very low viscous damping within the gyro itself. This low damping is due to the low viscosity flotation fluid mentioned before.

The DC power amplifier, which consists of Q4, Q5, and Q6, is a bootstrap-type of circuit with large amounts of DC feedback. Output impedance is very low, being on the order of a few ohms. The DC gain is three. DC current from this amplifier flows through a resistor which is selected to provide the correct scaling of 34.8 v/deg/sec for the attitude control system switching amplifier. The gyro torquer is connected after the scaling resistor so that rebalance current flows through it to the power supply common point. Over-all gain of the AC amplifier, demodulator, and DC amplifier is adjusted to 1000 v/v by means of R1.

j. Gas system leak test.

Scope. Leak-testing of a completed gas system involves pressurizing the system to proof pressures and then following this with a search for both major and minor leaks with a leak detectant solution. Such techniques are generally adequate but have several shortcomings, including the following:

(1) They have difficulty in detecting leaks in inaccessible places.

(2) They cannot detect gross leaks which can blow away solution before bubbles can form.

(3) Possible contamination of certain critical elements by leak detectant may result.

(4) Minute leaks may escape detection.

In order to avoid such shortcomings, the helium mass spectrometer survey has been used and has resulted in considerable savings in time and effort in producing systems with extremely low leak rates.

Operations. After the gas system has been completed through proof-testing, a general "snoop solution" test is made. The leaks which are detected are then removed. System pressure should be dropped to approximately 50 to 100 psi, and helium is introduced into the system. At this point no purge is necessary. The helium pressure is then raised to 3000 psi, and the needle valve on the inlet is closed. It is important to note that no valve actuation be permitted, as the helium flow over the valve seats can have deleterious effects. The mass spectrometer (Veeco or equivalent) sniffer head is then brought up to the item undergoing investigation. Sensitivity and threshold adjustments will require constant monitoring due to the extreme sensitivity of the instrument in the low ranges. An orderly progression from one item to another is made in order to ensure a complete search. Upon detection of a leak, the sniffer head is held stationary until the count indicator stabilizes. Every such indication is to be noted. After completion of the search, the total of all leak counts is determined and an appropriate leak rate (cc/hr) should be computed. It should be realized that helium is approximately three times as permeable as nitrogen and will therefore go through a hole one third as small as one for nitrogen.

Helium pressure is finally dropped until the check valve in the fill manifold no longer will flow. The helium inlet lines are finally exchanged for nitrogen and the system should be filled to approximately 500 psi. This fill should be followed by two purges at the same pressure level to evacuate as much of the helium as possible. The system can then be filled to the desired working pressure. The computed leak-rate data should be compared to the quantitative leak-rate measurements to be made at a later date in the buildup of the system. Such comparisons have not as yet been made to date because of inaccuracies in the readout of the mass spectrometer. It is expected that further use of this technique will permit actual meaningful comparisons. These procedures will be documented and become part of the total gas actuator system specifications.

D. Space Sciences

1. Planetary Scan Subsystem

a. Introduction. A continuing effort in the development of the planetary scan subsystem is described. A number of modifications have been made to accommodate new and revised requirements; otherwise, the subsystem is similar to that described in previous *SPS*. A block diagram of the subsystem is shown in Fig. 53.

When the subsystem is energized, a signal from a one-shot multivibrator circuit presets all logic circuits and the subsystem enters the planet searching mode of operation.

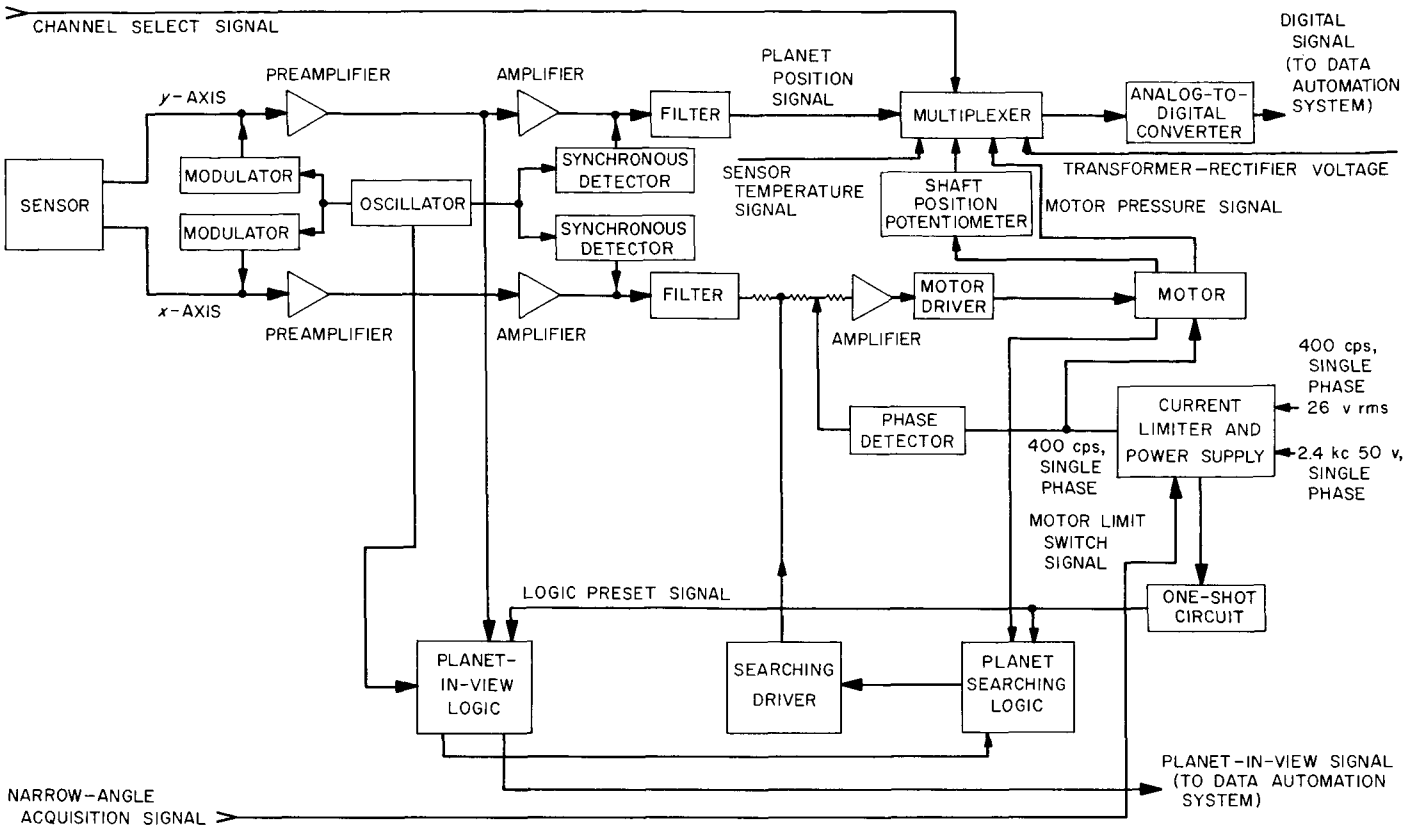

Fig. 53. *Mariner* C scan subsystem block diagram

The subsystem scans 180 deg in the process of searching for the planet. The scanning device provides the motion in one direction while the moving spacecraft provides motion approximately perpendicular to the scanning plane. A 400-cps motor is used for the scanning. Limit switch action is provided to reverse the direction of scan when the scanning of 180 deg is completed.

A planet sensor is utilized to detect the presence of the planet. The sensor, having a 50-deg circular field view, is sensitive to an image having a frequency range of 0.4 to 1.1 μ. When the planet comes into view, a signal from the planet-in-view logic switches the subsystem from planet searching to planet acquisition mode. The subsystem tracks the planet at its first bisector through the use of the servo system.

Upon receiving a narrow angle acquisition signal indicating the planetary science instruments are in position, the scan and tracking motions of the subsystem will cease.

b. Fiber optic system. A fiber optic system is being developed as an integral part of the planet sensor assembly. The system consists of conventional optical elements coupled by a conical fiber element to form a compounded system capable of fast response over the wide angular field. The purpose of the fiber element is to reduce the size of the image, thus allowing the use of a conventional optic system with a larger aperture at a specified field of view. The characteristics of the compounded system are as follows:

(1) Focal length: 10 mm.

(2) Effective f-ratio: $f/0.7$.

(3) Optical resolution: 20 line-pair per mm.

(4) Frequency response: 0.5 to 1.1 μ.

(5) Field of view: 50 deg.

(6) Weight: 1 lb.

(7) Dimensions: 2 in. in diameter, 6 in. in length.

c. Sensor. The radiation tracking sensor is a semiconductor junction device which converts the x-y coordinates of a light spot projected on its surface into a pair of voltages, V_x *and* V_y. A diagram of the sensor is shown in

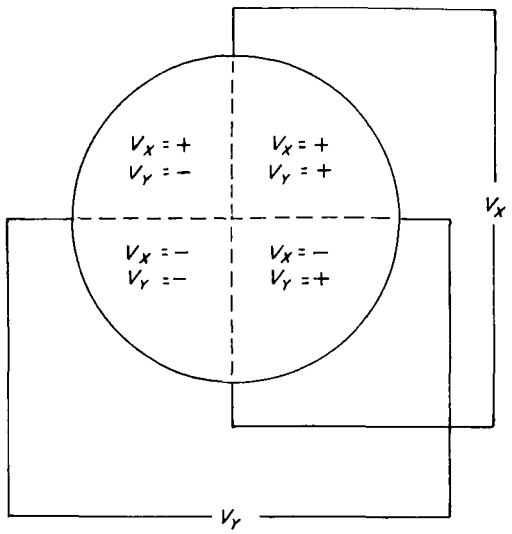

Fig. 54. Radiation tracking sensor

Fig. 54 with the polarities of the output voltages V_x and V_y as shown when the light spot is located in the indicated quadrant. When the light spot is located at the center, V_x and V_y are zero. Voltages from the sensor are self-generating and no bias voltage is required.

d. Electronics. A photomodulator device is used to modulate the DC x-axis output signal from the sensor. The photomodulator consists of a pair of small neon lamps and a matched pair of cadmium sulfide cells. An oscillator is used to drive the lamps at a frequency of 25 cps. The method of modulation by photomodulator was chosen for its simplicity and reliable operation. It also produces extremely low offset voltages when operating over the required temperature range.

The modulated signal is amplified by a 4-stage AC preamplifier having a gain of 8000 and an input impedance of 3 megohms. The signal is again amplified by a 3-stage, zener-coupled, AC amplifier having a gain of 1000 and an output impedance of 300 ohms. The signal is then demodulated and filtered by a synchronous detector and a 3-stage R-C filter network. The DC signal from the filter network is phase detected using the 400-cps signal to the driving winding of motor as reference. The phase detected 400-cps signal is amplified and utilized to drive and control the direction of drive of the motor.

The y-axis output signal of the sensor is similarly processed and amplified. This signal, indicating the planet

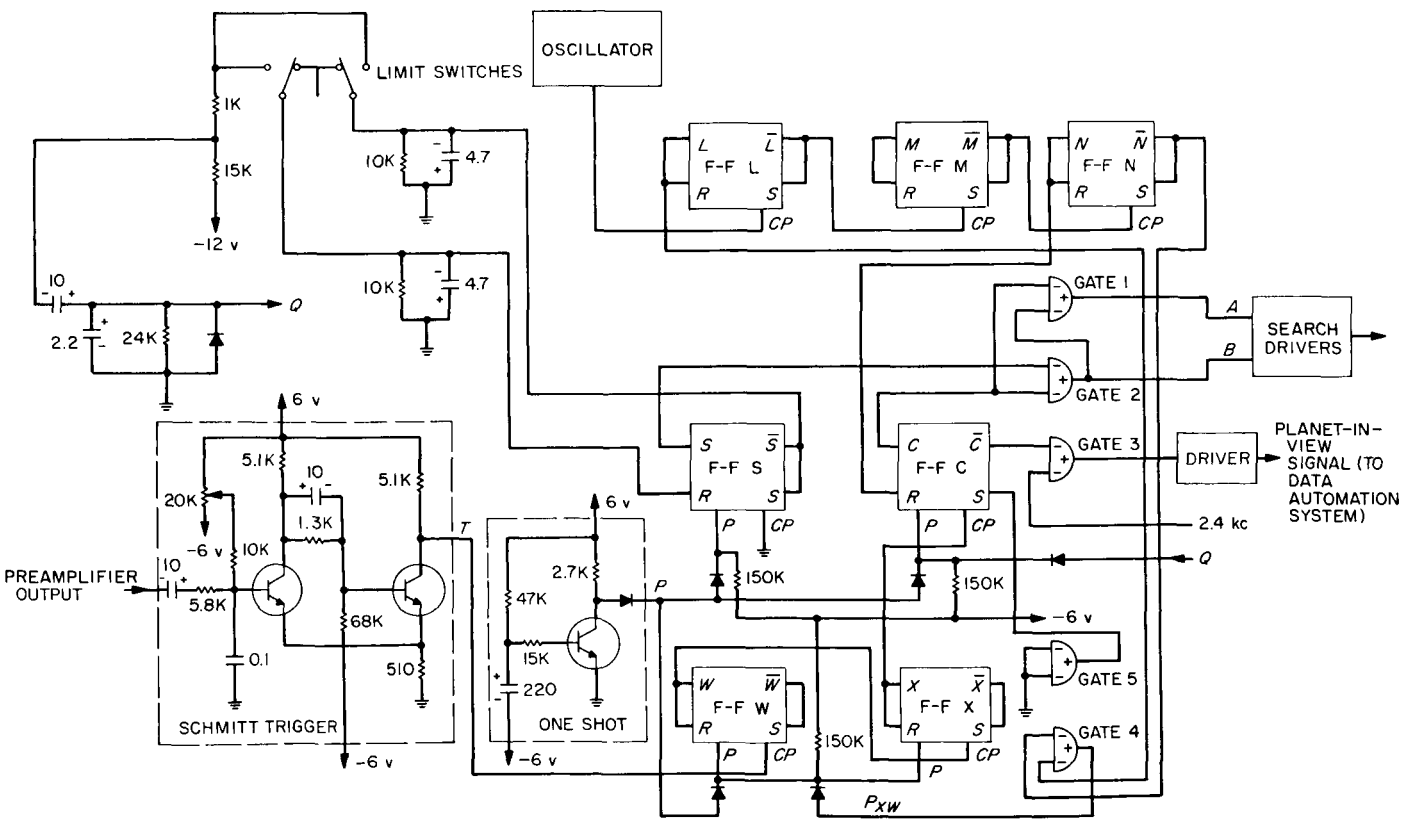

Fig. 55. Logic and control circuit

position, is then sent to the A-to-D converter via a multiplexer.

e. Logic and control circuitry. The logic and control circuits are as shown in Fig. 55. Searching and acquisition modes of operation are controlled by the flip-flop C (F-F C). When power to the subsystem is applied, a signal from the one-shot circuit presets all the F-Fs and the subsystem is in the planet searching mode. The clockwise and counterclockwise motor drive signals are controlled by F-F S. The F-F S in turn is being set and reset by the limit switches through the wave-shaping circuits.

Logic equations for the searching mode operation are as follows:

$$\bar{B} = CS$$

$$B = \bar{S} + \bar{C}$$

$$A = CB = C(\bar{S} + \bar{C})$$

$$= C\bar{S}$$

$$\bar{A} = S + \bar{C}$$

$$\text{CW drive} = AB$$

$$= C\bar{S}(\bar{S} + \bar{C})$$

$$= C\bar{S}$$

$$\text{CCW drive} = \bar{A}\,\bar{B}$$

$$= (S + \bar{C})(CS)$$

$$= CS$$

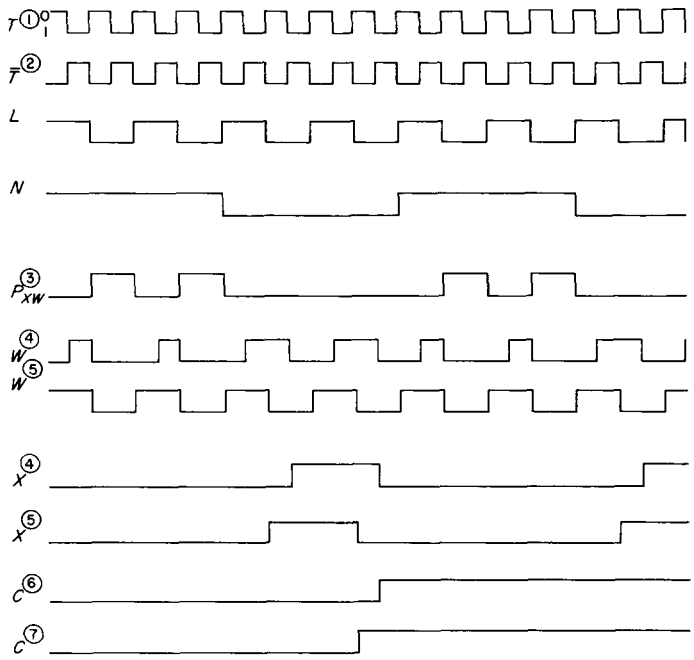

① SIGNAL T FROM SCHMITT TRIGGER WHEN SENSOR SIGNAL IS POSITIVE
② SIGNAL $\bar{T}$ FROM SCHMITT TRIGGER WHEN SENSOR SIGNAL IS NEGATIVE
③ SIGNAL P_{XW} FROM GATE 4 USED TO RESET F-F X AND W
$P_{XW} = N + \bar{L}$; $\bar{P}_{XW} = L\bar{N}$
④ CORRESPOND TO T, CHANGE STATE WHEN P_{XW} IS 1 AND CP CHANGE FROM 0 TO 1
⑤ CORRESPOND TO $\bar{T}$, CHANGE STATE WHEN P_{XW} IS 1 AND CP CHANGE FROM 0 TO 1
⑥ CORRESPOND TO T
⑦ CORRESPOND TO $\bar{T}$

Fig. 56. Planet-in-view logic

The planet-in-view logic consists of a Schmitt trigger, F-Fs W and X, and Gates 1, 2, 3, and 4. The Schmitt trigger is utilized to detect the voltage level of the modulated sensor signal from the preamplifier. Firing level of the Schmitt trigger is adjusted above the noise level. It is also so adjusted that the trigger will not fire when the spacecraft is at a distance from the planet beyond the acquisition capability of the subsystem.

A signal from the oscillator having the same frequency as the modulated sensor signal is frequency divided by eight through the use of F-Fs L, M, and N. This frequency-divided signal is utilized to control the sampling period. F-Fs W and X are used to count the number sensor signal pulses through the trigger during the sampling period. If eight or more pulses are gated during the sampling period, F-F C changes its state and the subsystem is now in the acquisition mode. If less than eight pulses are gated, F-Fs X and W are reset by the signal from Gate 4 during each sampling period. The counting operation resumes during next sampling period. Fig. 56 shows the wave form at the outputs of the various flip-flops and gates.

$$\text{Acquisition mode} = \bar{A}B$$

$$= (S + \bar{C})(\bar{S} + \bar{C})$$

$$= S\bar{C} + \bar{C}\bar{S} + \bar{C}$$

$$= \bar{C}(S + \bar{S} + 1)$$

$$= \bar{C}$$

f. Power supply and power consumption. Preamplifiers and amplifiers are designed to operate on plus and minus 12 v, and logic and control circuits on plus and minus 6 v. The subsystem requires 3.0 w of 2.4 kc, single-phase and 3.0 w of 400 cps, single-phase of primary spacecraft power to operate.

E. Propulsion

1. Introduction

The primary function of the *Mariner C* post injection propulsion system is to remove or reduce boost vehicle injection dispersion errors so that a Mars flyby with a sufficiently small miss distance can be reasonably assured. This function is performed during the two possible spacecraft maneuvers when the spacecraft is directed to turn to a prescribed position in space and impart a corrective impulse via the post injection propulsion system. A description of the *Mariner C* propulsion system was presented in *SPS, 37-19,* Vol. II.

2. Development Program

The development program to date has been covered in *SPS 37-19* and *37-20,* Vol. II.

Since the last reporting period, design work has continued and fabrication of some type-approval and proof test model equipment has commenced.

It has been decided not to use a spontaneous catalyst (*SPS 37-20,* Vol. II, p. 59) as the ignition system for the *Mariner C* post injection propulsion system. The decision to continue with the present design, which utilizes a bipropellant ignition system, was based on the fact that, although preliminary results are encouraging, the spontaneous catalyst is still too unproven to incorporate in a flight system at this time. Advanced development work will continue relative to the spontaneous catalyst.

In order to accommodate the maximum burning time capability of the propulsion system (approximately 100 sec), the CC&S clock which controls the duration of the motor burn has been changed from a 25- to a 12.5-pps system. This change will allow the CC&S to handle burning time of up to approximately 160 sec, but it does result in larger burning time errors. These timing inaccuracies (resolution errors) are reflected in velocity increment errors and they represent a major contributing factor to the errors in small maneuvers (less than 0.5 m/sec). By virtue of this fact, the total impulse or velocity increment predicted accuracies presented in *SPS 37-19,* Vol. II have been revised, the new prediction curve (includes spacecraft timer errors) being depicted in Fig. 57.

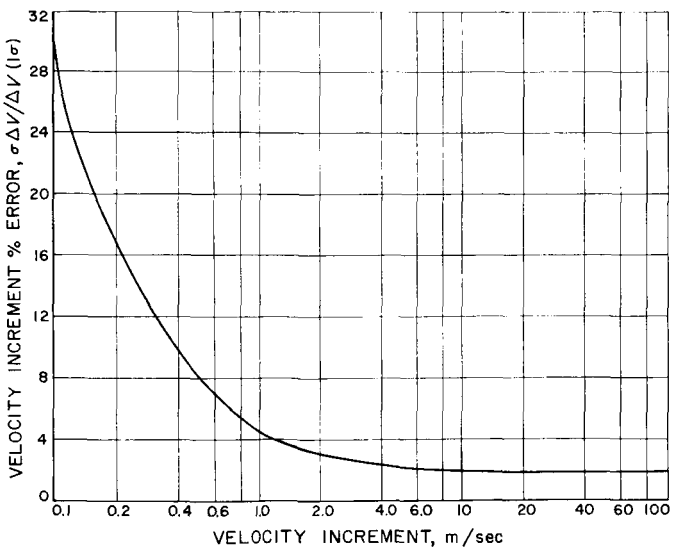

Fig. 57. 1-σ velocity increment percent errors versus velocity increment

F. Telecommunications

1. High-Gain Antenna

The high-gain antenna is attached to the spacecraft in a fixed position such that its maximum gain is in the direction of Earth at planet encounter. The antenna will be a 46- by 21.2-in. paraboloid, elliptical in planform. The parabolic sector was chosen in preference to a circular parabola of the same gain because of improved performance both at the low-gain antenna–high-gain antenna switch over portion of the spacecraft flight and at the post-encounter region. This is due to the broader antenna pattern in the plane containing the Earth tracks.

A dual cap turnstile feed (Fig. 58) is used to illuminate the sector. The dual cup ground plane establishes very low ellipticity over the illuminating region, which consequently produces low ellipticity over the sector's main beam. The illumination taper, including space loss correction around the edge of the sector, is a nearly constant 11 db.

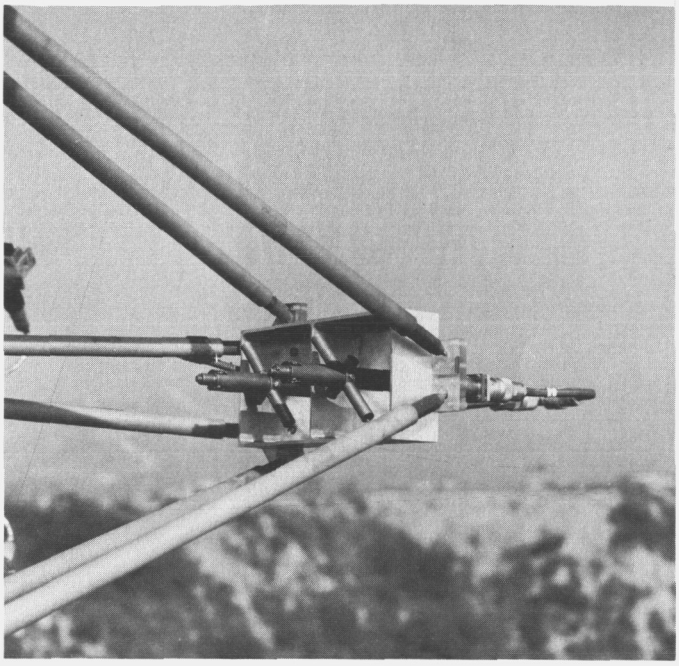

Fig. 58. Dual cup turnstile feed

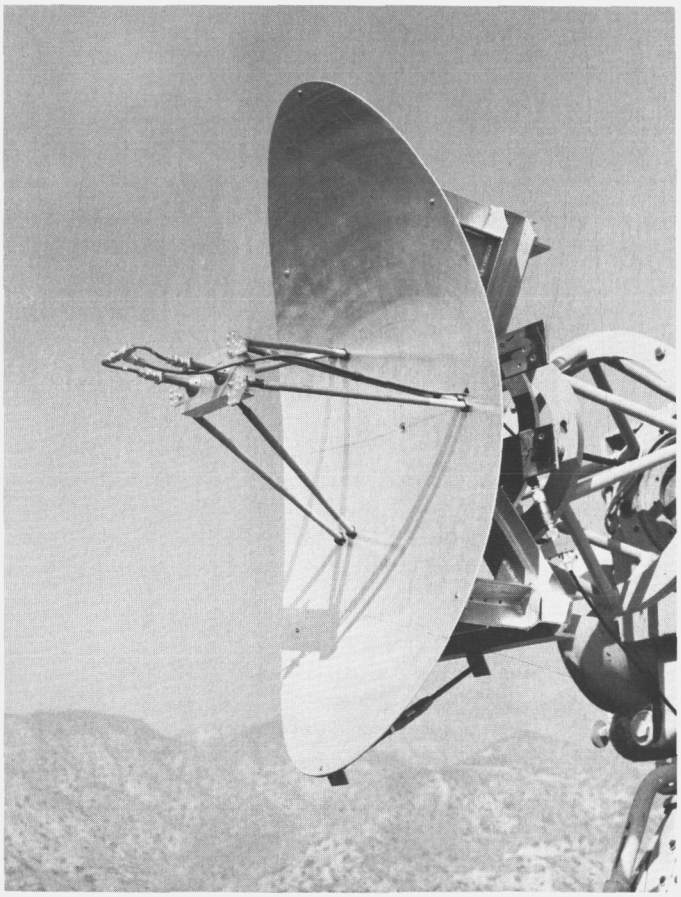

Fig. 59. Prototype high-gain sector

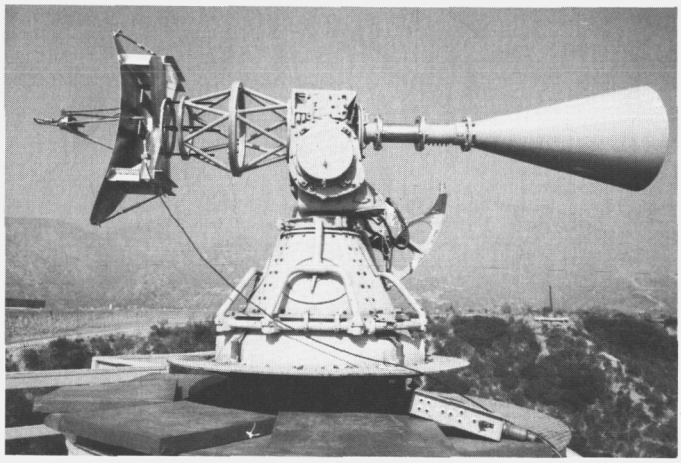

Fig. 60. Sector and standard gain horn in test position

Gain optimization of the feed reflector combination (Fig. 59) was accomplished by pattern and gain comparison methods in conjunction with feed focal position adjustments. Fig. 60 shows the prototype sector and standard gain horn mounted in test position. Optimum feed, sector, and focal position parameters chosen were:

Feed element separation = 2.92 in.

Sector f/d in the major axis = 0.33

Feed position = 15.21 in. from sector vertex to front face of feed cup aperture

Gain measurements of the prototype sector indicate a gain relative to circular isotropic of 23.5 $\pm$0.5 db. This is an area efficiency of ȯ1.5%. Radiation patterns measured in the minor and major axes of the sector are shown in Figs. 61 and 62 respectively.

The coaxial tee and cabling behind the feed, best seen in Fig. 59, will be replaced with a stripline hybrid ¼ in. thick attached to the back of the feed. The RG 142 cable used on the prototype will be replaced with ⅜-in. semi-rigid coax in the flight version.

Two identical prototype sectors are presently under construction using flight configuration feed support structure and dual cup ground plane. A confirmation of the measure gain will be made by an identical antenna gain measurement setup. Delivery of a type approval feed for assembly in the sector is scheduled for July 26, 1963.

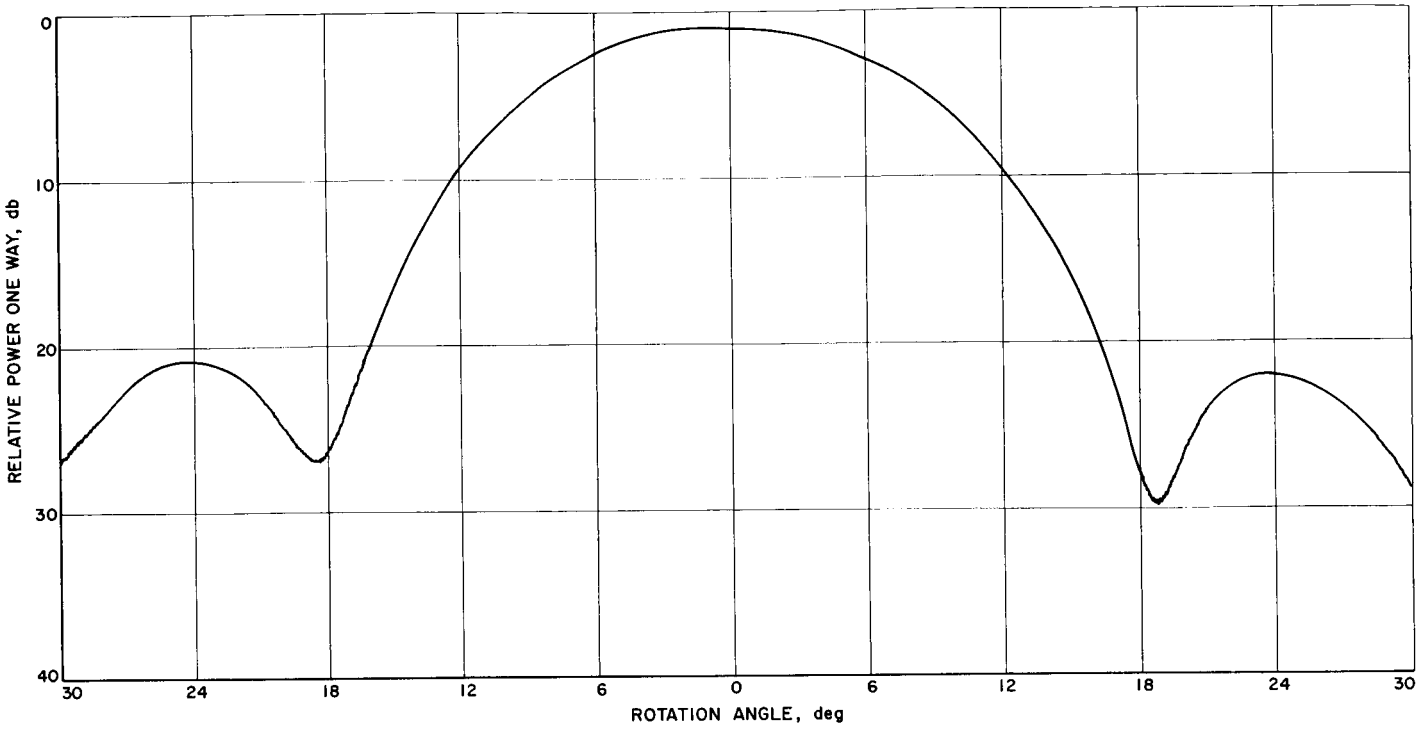

Fig. 61. Radiation pattern through sector minor axis

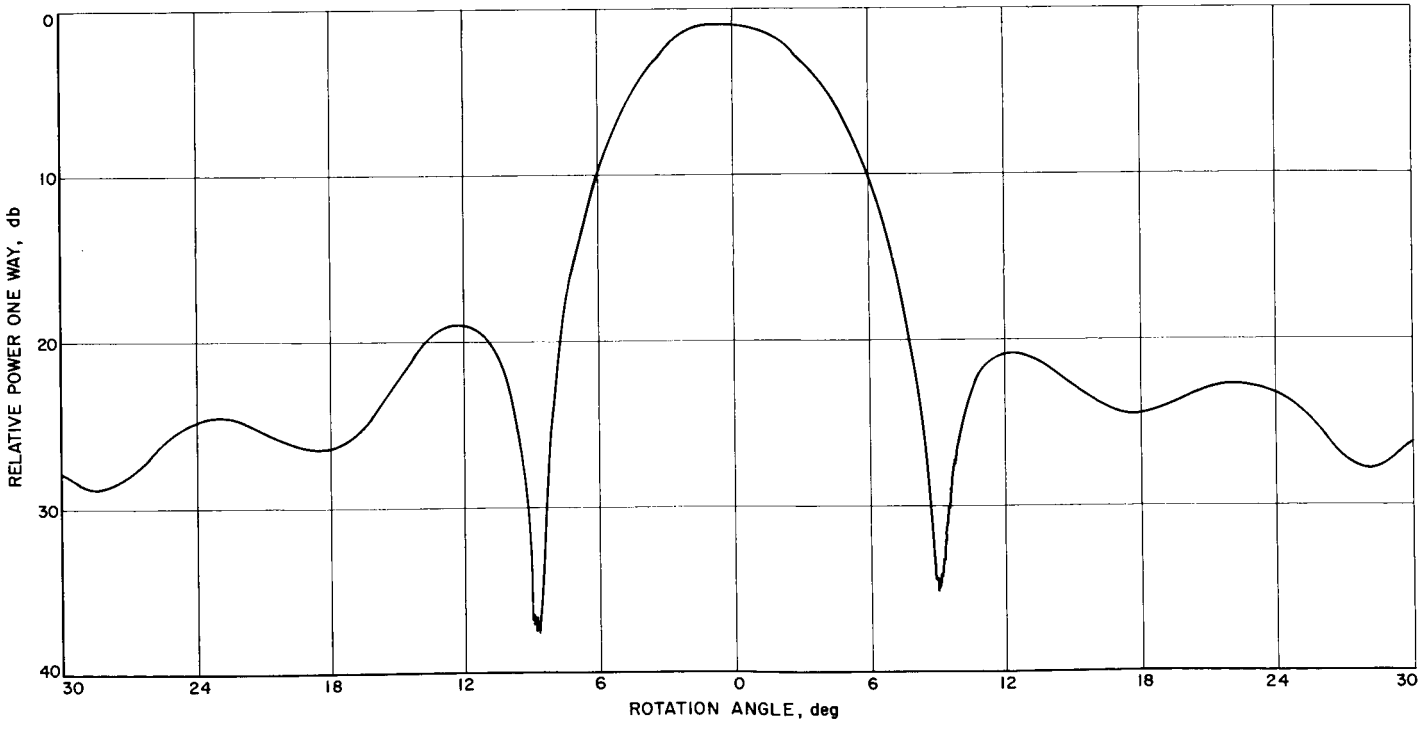

Fig. 62. Radiation pattern through sector major axis

G. Supporting Activities

1. Summary of Mariner C Environmental Test Program

During March and April, a total of 76 development and 20 type-approval tests associated with the *Mariner C* program were performed by the JPL Environmental Test Laboratory. These tests are listed as follows:

Facility	*Number of tests*
Vibration	59
Low frequency vibration	15
Acoustic	1
Shock	1
Temperature	7
Vacuum	4
Vacuum temperature	10
Total	97

2. Acoustic Testing

During March, a 10- × 12-in. section of an experimental *Mariner C* solar panel was tested in the 7-ft^3 pentagonal reverberation chamber (Fig. 63) to determine the effect of sound pressure on the solar cells. The panel, containing 105 solar cells, was suspended with rubber bands and exposed to bandlimited (300-1000 cps) noise for 90 sec. An Altec BR-150 microphone monitored the sound field. Noise level measurements were made over one-third octave bands, centered at selected points in the 200-2000 cps range. The maximum level recorded was 134 db (re: 0.0002 μbar) at center frequencies of 630 and 800 cps. The over-all noise level was 139 db.

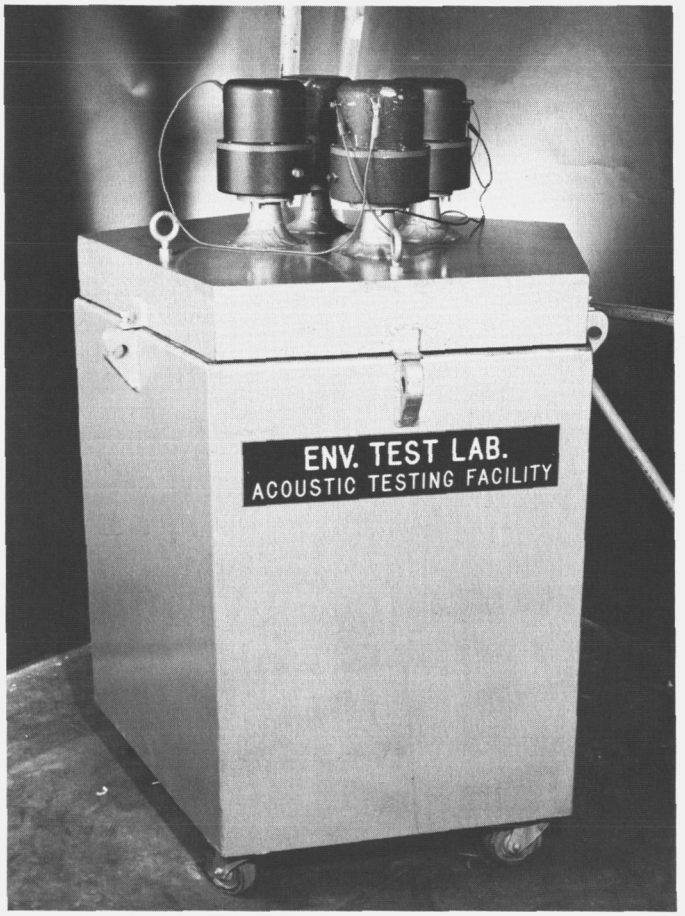

Fig. 63. Section of *Mariner C* solar panel suspended in reverberation chamber

Additional acoustic tests will be conducted on a full size *Mariner C* solar panel during May 1963.

IV. *Mariner B* Project

The primary purpose of the *Mariner B* Project is to permit scientific investigations of the planet Venus during the periods of availability in 1965 through 1970 and the planet Mars during the periods of availability in 1966 through 1971. Secondary purposes in order of priority are: (1) to make interplanetary scientific investigations in the regions between Earth and Mars, (2) to develop experience in the design of a spacecraft that has considerable flexibility with regard to the specific missions it is basically capable of covering, and (3) to provide experience and knowledge which will permit a quality and efficient design of the later *Voyager* spacecraft. To these ends, the spacecraft will be designed for a precision flyby mission and will incorporate the capability of either carrying or not carrying a small landing capsule. The *Mariner B* spacecraft will be injected by the *Centaur* launch vehicle. It is expected to launch two identical probes at each of the planet launching opportunities. Deep space probes to be launched in between periods of Mars and Venus availability are included in the *Mariner B* Project.

The preliminary design phase of *Mariner B* has been completed. Mission objectives, design characteristics and restraints, and functional specifications have been finalized and published. Further system efforts are being held pending review of the *Mariner B* Project by NASA.

A. Supporting Activities

1. Summary of Mariner B Environmental Test Program

During March and April, 11 development tests associated with the *Mariner B* program were performed by the JPL Environmental Test Laboratory. These tests are listed as follows:

Facility	*Number of tests*
Vibration	5
Vacuum	3
Vacuum temperature	1
Gas sterilization	2
Total	11

V. *Voyager* Project

The primary objective of the *Voyager* Project is the scientific exploration of Mars and Venus by means of spacecraft designed for use with *Saturn* boost vehicles. Secondary objectives are the scientific exploration of interplanetary space in the Mars-Venus region, and the determination of the feasibility of, the development of technology for, and the collection of scientific data necessary to successful manned flights to these planets.

Voyager flights are envisioned beginning in the 1967-69 period and continuing into the mid-1970's.

The *Voyager* Project is currently in the planning phase. The schedule is to submit to NASA management on September 1 of this year a *Voyager* Project Development Plan indicating the potential missions, the launch vehicle to be used, several development and flight schedules, estimated costs of the entire project, and a management plan. To generate the data required for this Project Development Plan, study efforts are now in process at the Marshall Space Flight Center (MSFC), at JPL, and in industry.

In the case of MSFC, a tentative decision was reached during this reporting period to use the MSFC-defined upper Stage S-VI on a *Saturn I-B* vehicle. Detailed conceptual studies for Stage S-VI are currently being conducted at MSFC. The tentative payload capability of such a launch vehicle is currently estimated to be in the range of 6,000 to 7,000 lb.

At JPL the Advanced Planetary Spacecraft Study Committee has been performing mission analyses since May 1962. Results to date indicate that the optimum mission for the *Voyager* class of spacecraft is probably a combination orbiter/lander. It is, therefore, this concept on which mission studies are being concentrated.

To supplement the JPL studies, early in April NASA headquarters selected General Electric's Missile and Space Division, Valley Forge, Pennsylvania, and the Avco Research and Advanced Development Division, Wilmington, Massachusetts, to also perform mission studies for the *Voyager* spacecraft. These two companies were selected from an open competition to which a total of 13 companies responded with proposals. Most of the unsuccessful bidders have indicated a desire to continue at their own expense the same type of effort that General Electric and Avco are conducting. The results of these industry studies will be incorporated, as appropriate, into JPL's results in the preparation of the Project Development Plan.